Modelling and experimental observation of ferroelectric domains



Dan Sui
Oriel College
Department of Engineering Science
University of Oxford

Supervised by: John E. Huber
Hilary Term 2015

Modelling and experimental observation of ferroelectric domains

Dan Sui, Oriel College, University of Oxford
For the degree of D.Phil. in Engineering Science, Hilary Term 2015

Abstract

This thesis focuses on studying the interaction and evolution of the needle domains in barium titanate single crystal through the simulation and experimental methods. The results are expected to assist in the interpretation of the arrangement and evolution of the needle domains and improve the design of future material.

The existence of a needle domain gives rise to an internal stress field and electric field around the needle tip, which influences the polarization switching process and crack propagation in a single crystal. A model is established to study the interaction and evolution of the needle domains in barium titanate single crystals using the theory of dislocations. Considering the electrical and mechanical incompatibility at the needle tip, the fields produced by a needle domain are represented using the fields due to the equivalent edge dislocations and line charges distributed over the needle tip. Accordingly, the dislocation fields derived by Barnett and Lothe for anisotropic piezoelectric media are used to analyse the stress and electric fields around the needle domains. The calculation of the modified Peach-Koehler force and the total energy due to the needle domains is used to study the interaction among the needle domains and the stability of the needle pattern. Through experimental observation, we further know about the microstructure and common pattern of needle domains. X-ray diffraction is used to map the shape of needle tip and detect the strain field around the needle tip.

The interaction of pairs of needle domains in an infinite piezoelectric body is studied. It is found that the needle tip interactions tend to be dominated by the electrostatic terms. Additionally, the stability of groups of needle domains is investigated. Stable configurations of needle domains in a herringbone pattern are identified, consistent with experimental evidence. However, comb-like arrays of needles are found to be unstable. This is contrary to experimental observations, where needle domains are observed in aligned arrays. This contradictory result leads to an analysis of the effect of charge produced by the polarization jump at a needle tip on domain interaction. The existence and position of stable equilibrium states are found to be sensitive to a change in the quantity of polarization charge. When the polarization charge is

reduced to about 48% of its theoretical value, the modified model works well to interpret the stability of comb-like needle pattern and herringbone needle pattern.

A viscous model is proposed to further analyse the evolution of the needle domains under the external perturbation. Based on the superposition theory proposed by Van der Giessen, boundary value problems are discussed. Single needles and pairs of needle domains are selected to analyse the effect of boundary condition on the distribution and arrangement of the needle domains. After that, the evolution of the comb-like needle domains under the applied external loads is studied. During the process of analysis, a lattice friction model, and the viscous model are compared.

Acknowledgements

I would like to take this opportunity to appreciate my supervisor Dr. John Huber for his guidance, support, and encouragement. He gave me advice and direction while allowing me the freedom to develop the project. Especially, when I faced the double difficulties from my study and the coming of my baby, he gave me lots of free time and space to balance my life. Without his advice and encouragement, I could never overcome this tough period.

I would like to especially thank Prof. C. Chen in Tsinghua University for many useful discussions through the course of this work. His constructive suggestion enlighten me in research study. I am also grateful for the kind help from Prof. Jay Shieh in National Taiwan University. His rich experience in experiment unblocked my blockage.

I acknowledge Engineering and Physical Sciences Research Council (EPSRC) for providing financial support. It is an honour to be a member of Oriel College, and I am profoundly grateful to Oriel College for its kind and warm support.

I also thank all the members in the Material Engineering group for making my life enjoyable. Especially, I want to thank Nien-Ti Tou, Prashant Potnis, and Kwanlae Kim for their advice and help. Many thanks to Mathew Arthington who provided all kind of help. Additionally, I would like thank Dave, Ano, and Doris for their accompany.

None of this would have been possible without the constant care, the immense patience and unconditional support I received from my husband and my family, to whom I am more than grateful. Also many appreciate and treasure the coming of my sweet baby Jason. His coming promoted me grow fast, and his laugh and kiss could charge my exhausted body. I am lucky to have my family, thanks.

Contents

Abstract **i**

Acknowledgements **iii**

Contents **iv**

List of Figures **vii**

1 Introduction **1**
1.1 Motivation of research 1
1.2 Background of ferroelectric crystals 3
1.3 Single crystal ferroelectrics 6
1.3.1 High performance of single crystal 6
1.3.2 Challenge of single crystal 7
1.4 $BaTiO_3$ single crystals 8
1.5 Needle domains 13
1.5.1 Structure and arrangement of needle domains 13
1.5.2 Review of needle domain research 15
1.6 Layout of this thesis 19

2 Chapter 2 Model of needle domains **21**
2.1 Dislocations in crystals 21
2.1.1 Definition of edge dislocation 22
2.1.2 Peach-Koehler forces 23
2.2 Domain compatibility 26
2.2.1 Minimum energy 26
2.2.2 Electrical and mechanical compatibility 28
2.3 Modelling of needle domains 30
2.4 Fields due to a dislocation with a line charge 35
2.5 Modified Peach-Koehler force 40
2.6 Relationship between plane strain and plane stress 42

3 Chapter 3 Observation of needle domains **45**
3.1 Optical microscopy . . . 45
3.1.1 Optical techniques . . . 46
3.1.2 Generation and configuration of needle domains . . . 47
3.2 X-ray observation methods . . . 51
3.2.1 Distinguishing domain types using X-ray diffraction . . . 56
3.2.2 Strain measurement using X-ray diffraction . . . 57
3.3 Synchrotron X-ray experiment to identify domain needles . . . 59
3.4 Measurement of domain needle shape . . . 64
3.5 Measurement of strain field around a needle tip . . . 67
3.6 Conclusions . . . 71

4 Chapter 4 Simulation of needle fields **72**
4.1 Nondimensionalization . . . 72
4.2 Isotropic reference case . . . 73
4.3 Fields due to a single needle domain . . . 76
4.4 Interaction of the needle domains . . . 80
4.4.1 Identical tips in parallel domains . . . 80
4.4.2 Perpendicular needle domains . . . 83
4.4.3 Opposite parallel domains . . . 85
4.5 Groups of needle domains . . . 86
4.5.1 Herringbone pattern of needle domains . . . 86
4.5.2 Comb-like needle domains with identical tips . . . 88
4.6 The effect of polarization charge on stability . . . 90
4.7 A needle domain detached from the comb . . . 95
4.8 Influence of external perturbation on groups of needle domains . . . 98
4.8.1 Viscous model for the motion of needle domains . . . 98
4.8.2 Comb of needles with a small perturbation . . . 99
4.8.3 Comb of needles with a large perturbation . . . 102
4.9 Domain bundle boundaries in a $BaTiO_3$ single crystal . . . 103
4.10 Estimation of friction F_{cr} . . . 107
4.11 Conclusions . . . 112

5 Chapter 5 Boundary effect **114**
5.1 Superposition theory for boundary condition 114
5.2 The boundary influence on the fields and arrangement of the needle domains . . 118
5.2.1 Single needle domain under the effect of BC 120
5.2.2 A pair of needle domains in a finite crystal 123
5.2.3 The effect of polarization charge on interaction of needle domains . . . 128
5.3 Evolution of a pair of needle domains under applied compressive force 130
5.4 Evolution of comb needles under mechanical loads 138
5.5 Conclusions 141

6 Conclusions and further work **143**
6.1 Conclusions and discussions 143
6.2 Future work 147
6.2.1 Improvement of current model of needle domains 147
6.2.2 Free charge and free traction 149

A List of publications and conference proceedings **155**

References **156**

List of Figures

1.1 Typical polarization-electric field hysteresis loop. 4
1.2 Representative strain-electric field hysteresis loop in ferroelectrics. 5
1.3 Piezoelectric coefficient d_{33} as a function of transition temperature T_c [22] . . . 5
1.4 Various crystalline phases of $BaTiO_3$ with cooling temperature modified from [12]. 8
1.5 $BaTiO_3$ crystal structures of unit cell in cubic and tetragonal phases [14] 9
1.6 Six equivalent variants of polarization in tetragonal phase 10
1.7 Schematic diagram of a^1, a^2, and c domains 10
1.8 (a) Lattice configuration (b) Macro structure for $180°$ and $90°$ domain walls in a crystal plate 12
1.9 Herringbone pattern with watermarks formed by $180°$ domain in $BaTiO_3$ cermics [45] 12
1.10 (a) Needle-shaped domains with round or sharp tip (b) Wedge-shaped domains 13
1.11 (a) Needle-shaped domain observed by optical microscope (b) TEM micrographs showing needle-shaped domains in the $BaTiO_3$ single crystals [50] . . . 14
1.12 (a) Needle domain observed in $LaAlO_3$ single crystal [48], the subscript 'pc' is used to denote pseudocubic indices; (b) Herringbone pattern needle domains in $BaTiO_3$ single crystal observed by TEM [51]; (c) Comb pattern of needle domain in $BaTiO_3$ [52]. 15
1.13 3-D laminar structure composing of needle domains 15
1.14 Optical micrograph showing the boundary between incompatible chevron orientations in $LaAlO_3$ single crystal [56]. 17
1.15 Comb needle observed by Little in $BaTiO_3$ single crystal [44]. 17
1.16 Needle domains existing ahead of the crack tip during crack propagation [16]. . 18

2.1 Schematic diagram of edge dislocation (a) atom structure, (b) from a continuum standpoint [66]. 22
2.2 Burgers circle (a) in a crystal with edge dislocation (b) in a perfect crystal [67]. 22
2.3 Peach-Koehler force of two parallel dislocations along x axis (modified from [70]). 25
2.4 Peach-Koehler force on dislocation (a) slip force F_x contour map (b) Interaction between two dislocations in x direction 25
2.5 A ferroelectric system applied by a dead load $\mathbf{t}_0$ and external electrical field $\mathbf{e}_0$ (modified from [72]) 27
2.6 Compatibility of polarization and strain in a domain pair 29

2.7 (a) 180° ferroelectric domain wall (b) 90° ferroelectric domain wall [49] 29
2.8 Schematic representation of the needle domain, (a) Needle tip as an assembly of equivalent dislocations modified from Bornarel [54], (b) An equivalent dislocation in the $BaTiO_3$ crystal structure, (c) Geometry of unit cells used for calculating Burgers vector $\mathbf{b}_0$ 31
2.9 Equivalent charge spreading over the needle tip due to the electrical incompatibility 33
2.10 Needle domains with different orientations in four quadrant location. 34
2.11 The plane coordination system 36

3.1 Optical observation and sketch of a 90° domain wall between an a domain and two c domains in $BaTiO_3$ single crystal [43]. 47
3.2 Observation of wedge-shaped laminar domains and square-net domain pattern in $BaTiO_3$ single crystal [12]. 47
3.3 Observation of needle domain in $BaTiO_3$ single crystal under optical microscopy. 48
3.4 Variation of needle pattern with the changing temperature from 90°C to 25°C. . 49
3.5 Patterns of needle domain (a) Comb-like needle domain (b) Herringbone type array of needle domains 50
3.6 Comparison of microstructure for antiparallel 180° domains in $LiTaO_3$ crystals imaged by X-ray and Optical microscopy (a) X-ray Bragg-diffraction image, (b) the same area imaged by optical microscopy [84]. 52
3.7 Diffraction of X-rays by a crystal lattice. 53
3.8 (a) Scattering of X-ray by a specimen (b) The diffraction angles used in X-ray analysis (edited from [90]). 54
3.9 Rocking curve of the [4 0 4] and [0 12 0] Bragg reflections of $CaFeO_{2.5}$ single crystal [91]. 55
3.10 Asymmetric reflections of $BaTiO_3$ single crystal with tetragonal phase: (a) a^1-reflection [402], (b) a^2-reflection [240], (c) c-reflection [204]. 57
3.11 Shift in the Bragg peak produced by change in spacing between diffracting atom layers. 58
3.12 X-ray observation (a) Experimental set up of X-ray observation showing X-ray source, specimen and detector (b) Specimen illuminated by the X-ray beam (c) Optical micrograph of $BaTiO_3$ single crystal specimen with needle domains observed by Potnis [92]. 61
3.13 Different types of domains showing at scan 1 rocking curve of sample located at $x = -1$ mm and $y = 0.41$ mm, when the specimen is rocked in the range of ω between 21.02° and 23.02° with step of 0.005°. 62
3.14 Integrated images of the different domain types detected by X-ray in $BaTiO_3$ single crystals 63
3.15 Combined image with colourful domains [92]. 64
3.16 Integrated image of a needle domain. 65
3.17 Wedge shape of needle domain. 66
3.18 Variation of normalized total intensity in spot area along x-axis direction. Solid line is intensity data line; Dash line is linear fitted line. 66
3.19 The scanning range ($200\ \mu$m $\times$ $200\ \mu$m) around needle tip. The lattice point located at the bottom-left corner was defined as unstrained lattice. 67

3.20 Spot scan ($10\ \mu$m $\times$ $10\ \mu$m) over the range of $200\ \mu$m $\times$ $200\ \mu$m. The lattice located at bottom-left corner is defined as unstrained lattice. 69
3.21 Microstrain field around the needle tip in [240] direction measured by X-ray diffraction. 70
3.22 Microstrain field around the needle tip in [240] direction calculated using the simulation model. 70

4.1 An edge dislocation in isotropic material 74
4.2 Contour maps for various fields due to an edge dislocation in isotropic medium under plane strain, (a, c, e) the strain distributions, normalized by ε_0; (b, d, f) the stress distributions, normalized by σ_0. 75
4.3 Computing range of a single needle domain modelled as one edge dislocation with a positive line charge 76
4.4 Contour maps of strain and stress components under plane strain which are normalized by ε_0 and σ_0, representatively. 78
4.5 (a) Electric field component E_1^* (b) Electric field component E_2^* surrounding a needle domain in $BaTiO_3$ with Burgers vector [1 1 0] and positive line charge . 79
4.6 Energy density field surrounding a single needle domain, normalized by $\varepsilon_0\sigma_0$. . 79
4.7 Schematic diagram of two parallel needle domains with identical tips. 81
4.8 Contour map of extension force on N_2 domain for two parallel domains with identical tips. 81
4.9 Normalized energy for two parallel domains with identical tips. 82
4.10 Schematic diagram of two perpendicular domains. 83
4.11 Contour map of extension force on N_2 domain for perpendicular needle domains. 84
4.12 Energy variation with the changed length of N_2 domain 84
4.13 Schematic diagram of parallel needle domains with opposite tips. 85
4.14 Contour map of extension force on N_2 domain for parallel needle domain with opposite tips. 85
4.15 (a) A Herringbone type array of needle domains observed by optical microscopy in $BaTiO_3$ specimen with thickness of 1 mm; (b) Herringbone needle domains observed by TEM in thin film of $BaTiO_3$ with 300 nm [51]. 87
4.16 Schematic of a herringbone pattern of needle domains. 87
4.17 Energy variation due to change in length of needle domains in a herringbone-type pattern. 88
4.18 Schematic diagram of comb of needle domains with identical tips. 89
4.19 Energy variation due to change in length of needle domains in a comb-like pattern. 89
4.20 Variation of the stable equilibrium position with changing the polarization charge. 91
4.21 Contour map of extensions force on N_2 domains for two parallel domains with identical tips as varying the change of polarization charge. 91
4.22 Variation of the total internal energy with changing the polarization charge. . . 92
4.23 The comb-like needle domains observed by optical method. 92
4.24 Contour map of extension force on N_2 which is perpendicular to the needle N_1 for the reduced polarization charge $Q = 0.48q$. 93

4.25 Interaction between of two perpendicular needle domains (a) Schematic of two perpendicular needle domains with the spacing $s = 10w$; (b) the extension force acting on each needle domain. 94
4.26 (a) Outline of equilibrium position and its reflected line in order to explain the interaction of detached needle with the whole comb, (b)Interaction of parallel needle domains on the detached needle domain 97
4.27 The detached needle acted by longer and shorter comb. 97
4.28 The relation of velocity to the acting force on needle domain (a) Friction $= F_{cr}$, (b) No friction 99
4.29 The evolution of the detached needle tips under small perturbation 101
4.30 The evolution of the detached needle tips under strong perturbation 103
4.31 The comb needles with two detached tip fronts [52]. 104
4.32 A pair of parallel needle domains with opposite tip 105
4.33 (a) Contour map of extension force on needle N_2; (b) extension force acting on needle N_2 moving along the line $x_2 = x_1 - 20w$. 105
4.34 (a) Staggered arrangement of needle domains with opposite tips; (b) equilibrium pattern of needle domains obtained using dislocation method. 106
4.35 STEM images showing two parallel sets of 90° domain bundle and a bundle boundary [95] 107
4.36 The blunt needle tip modelled as the coupling fields of an effective dislocation **b** and line charge q. 108
4.37 Needle domain tip with a distribution of dislocation coupled to line charges (a) Triangle tip distributing the equal dislocation coupling charge. (b) Due to the small opening angle of needle tip, all the equivalent dislocations coupling charge are distributed along one straight line. (c) The relationship of each dislocation coupling charge along the x-axis. 109
4.38 The relationship between friction stress τ_0 and the number n of distributing dislocations coupling charge 111
4.39 The relationship between friction stress (τ) and the number n of distributing dislocations coupling charge 112

5.1 Decomposition of the boundary value problem into the sum of the singular ($\sim$) fields associated with the individual needles and the image ($\wedge$) fields that enforce the prescribed boundary conditions. 116
5.2 Decomposition of the boundary value problem with free traction and zero potential 118
5.3 The element unit with the local coordinate (ξ, η). 119
5.4 Contour map of stress σ_{11} for one single needle domain with $0.48q$ charge at its tip for the infinite case. 121
5.5 Stress σ_{11} fields produced by a single needle domain located at different position, (0, 0), ($60w$, $60w$), ($160w$, $160w$), and ($220w$, $220w$). 121
5.6 Change in energy as the needle domain approaches to an edge. 122
5.7 Two interactive needle domains approaching to edge 123
5.8 Extension forces acted on two needle domains with spacing $10w$ when needle N_1 is fixed at (0, 0) ($50w$, $50w$) and ($200w$, $200w$), respectively. 125
5.9 Extension forces acted on two needle domains with spacing $30w$ when needle N_1 is fixed at (0, 0) ($50w$, $50w$) and ($200w$, $200w$), respectively. 126

5.10 Change of angle θ with respect to the distance of tip position from edge and the quantity of polarization charge at the needle tip. 129
5.11 Change of energy with respect to the tip position x_1 of needle N_1 and the quantity of polarization charge at the needle tip. 130
5.12 A pair of needle domains under the effect of compressive loads. 131
5.13 A pair of needle domains under the application of compressive step loads with increment 0.01 MPa (Solid line: needle N_1; Dash line: needle N_2). 133
5.14 A pair of needle domains under the effect of compressive loads with large increment 0.1 MPa (Solid line: needle N_1; Dash line: needle N_2). 134
5.15 A pair of needle domains under the effect of compressive loads with increment 0.01 MPa (Blue line: needle N_1; black line: needle N_2). 135
5.16 The arrangement of needle domains for the different loading steps with the increment 0.01 MPa. 135
5.17 A pair of needle domains under the effect of compressive loads 0.1 MPa (Blue line: needle N_1; black line: needle N_2). 137
5.18 The arrangement of needle domains for the different loading steps with the increment 0.1 MPa. 137
5.19 An array of comb-like needle domains under the action of the compressive stress. 138
5.20 Evolution of comb-like needle domains applied by varying compressive loads. 139
5.21 Evolution of comb-like needle domains with the pinned needle applied by varying compressive loads levels (a) The needle N_1 is pinned, (b) the needles N_1 and N_2 are pinned. 141

6.1 Needle domains with two ends: (a) Schematic graph of needle domains with two ends, (b) needle domains with two ends observed in the experiment. 149
6.2 Decomposition of the boundary value problem 150

1

Introduction

1.1 Motivation of research

Ferroelectric materials have been extensively used in many areas of technology and science due to their electromechanical properties [1–4]. Ferroelectric materials are a special class of piezoelectric, which in general exhibit a large piezoelectric response. Sensors based on the direct piezoelectric effect transform mechanical signals into electrical signals, and are used as ultrasonic transducers for civil and military applications. Piezoelectric actuators based on the converse piezoelectric effect transform electrical signals into mechanical signals, and are applied in displacement actuators and force generators. Combining piezoelectric effect with converse piezoelectric effect, sonar which is one of the most successful inventions, is widely used for undersea communications and detection [5, 6]. In addition, ferroelectrics have recently emerged as potential materials for information technology and data storage applications due to their inherent high dielectric properties and high polarization [7–9]. They offer many benefits such as high reading and writing speed, low power consumption, high endurance, and better scalability than non-volatile memories. Ferroelectric memory makes use of polarization switching to encode binary data. Besides, electrical, optical, and thermal properties of ferroelectrics are exploited for a wide range of technological applications including high dielectric constant capacitors, shutter devices and temperature sensors [4–6, 10]. Their macroscopic mechanical and

electrical properties are strongly related to the microstructural domain patterns. Therefore, the studies of domain configuration and its evolution are of fundamental interests, and are expected to improve the working performance in applications. Improved understanding of the engineering of domain microstructures has led both to models of macroscopic material response, and also to the improved design of ferroelectric materials.

Barium titanate ($BaTiO_3$) single crystals, as lead-free ferroelectric materials, have been widely used to investigate ferroelectric behaviour [11–14]. The most direct reason is that they can offer great promise for understanding of microstructure evolution in theoretical work, due to simple crystal structure and good chemical and mechanical stability. Besides, an important value is that they have advantages of providing ultrahigh polarization and ferroelectric strain and possessing excellent electromechanical properties.

Perfect single crystals with an ideal single domain structure are hard to manufacture and instead needle-shaped domains are commonly found in the crystals [12,15]. In fact, these needle domains usually appear in a comb-like pattern. The existence of a needle-shaped domain gives rise to an internal stress field and electric field around the needle tip. The needle-shaped domains as crystal defects influence the polarization switching process. Additionally, it is found that the growth of needle-shaped domains generally accompanies crack propagation in single crystal $BaTiO_3$ [16]. Better understanding of the growth behaviour of needle domains during fracture is important for assessing the lifetime of ferroelectrics and improving their reliability [17,18]. One way in which needle domains can affect polarization switching is for a series of parallel needle domains to grow and produce a laminated texture. The laminated region can then propagate through a crystal changing its average polarization and strain state.

However, the formation and interaction of needle domains in $BaTiO_3$ single crystals are not fully understood. Questions such as how to build a theoretical model for investigating the interaction of needle domains, why the family of needle domains usually exist in certain forms,

how a needle domain responds to applied electrical or mechanical loads, and how to control this kind of microstructure so as to design material performance remain open.

My objective is to obtain a fundamental and detailed understanding about the evolution of needle domain structures to support the design of materials, based on both theoretical analysis and experimental observations.

1.2 Background of ferroelectric crystals

In this section, we review the basic concepts and properties of ferroelectric crystals. In addition, opportunities and challenges presented by single crystals are highlighted.

Ferroelectricity was first discovered in the Rochelle salt crystal in 1921 [1–3], and ferroelectric materials have since been intensively investigated because of their importance as electronic components. Ferroelectric crystals are generally defined as a class of materials possessing a spontaneous electric polarization that can be reversed by the application of an external electric field [10]. The spontaneous polarization is induced by a non-centrosymmetric crystal structure.

Ferroelectricity is characterized by non-linearity and hysteresis which result from polarization switching. The non-linearity and hysteresis characteristics have been studied extensively [19–21]. When an external field is applied, the polarization can be reoriented in the direction of the electric field. This process is reversible and is called polarization switching. The polarization switching can be observed by measuring the electric displacement while the electric field is applied. The polarization-electric field hysteresis loop is the most important characteristic of ferroelectric materials, as shown in figure 1.1. It shows that the influence of an external electric field causes the rearrangement of domains. The different rates at which the domains and electric field change lead to a phase difference between the electric field intensity and polarization, hence non-linear variations. In figure 1.1, as the applied electric field increases from A to B, domains in which the direction of spontaneous polarization is different from the

electric field direction begin to switch. The switching process continues until most of the domains are aligned in the electric field direction. If the electric field increases beyond point C, the relationship of polarization (P) to the applied electric field (E) becomes saturated for the ferroelectric material. Spontaneous polarization, P_s, is defined from this curve by the extrapolation of the almost linear region B-C at saturation back to the polarization axis. When the field returns to zero, the polarization does not return back to the initial value, which is displayed by the nonlinear change from point B to D in figure 1.1. The remaining polarization is known as the "remnant polarization", P_r. As the electric field is cycled, the strength of the electric field needed to switch to the opposite polarization is called the coercive electric field, E_c. The process can be repeated, giving a stable hysteresis loop.

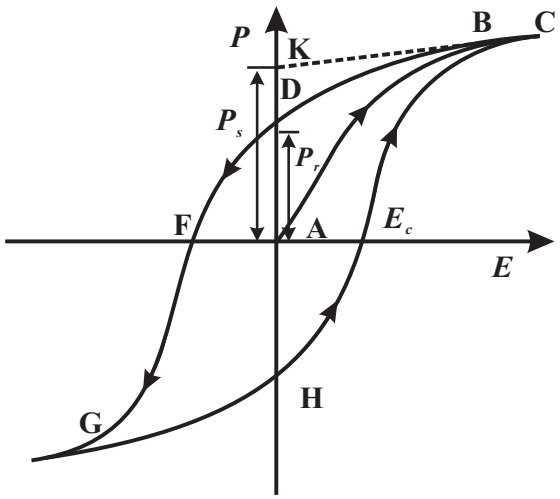


Figure 1.1: Typical polarization-electric field hysteresis loop.

In addition to the polarization-electric field hysteresis loop, another significant hysteresis loop is the strain-electric field loop, which is shaped as a butterfly, shown in figure 1.2. The strain-electric field hysteresis loop arises from combined effects: the piezoelectric effect of the crystal lattice, and ferroelectric switching. To illustrate how the strain of the crystal changes during the electric field cycling, the following description is given. After several load cycles, at point A, a positive remnant polarization and remnant strain exist in material. When a negative electric field is applied, the strain induced by the electric field decreases due to the piezoelectric

effect and depolarization of the ferroelectric. The re-polarization starts at point B where the coercive field is reached. From B to C, the polarization switches to the direction of the applied electric field. When the electric field returns to zero, the remnant strain at point D coincides with that at point A but the remnant polarization is opposite. When a positive electric field is applied, the ferroelectric experiences the same process but the switching direction is opposite.

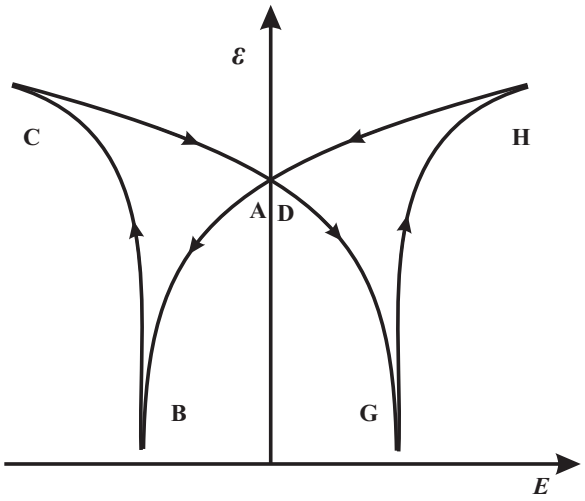


Figure 1.2: Representative strain-electric field hysteresis loop in ferroelectrics.

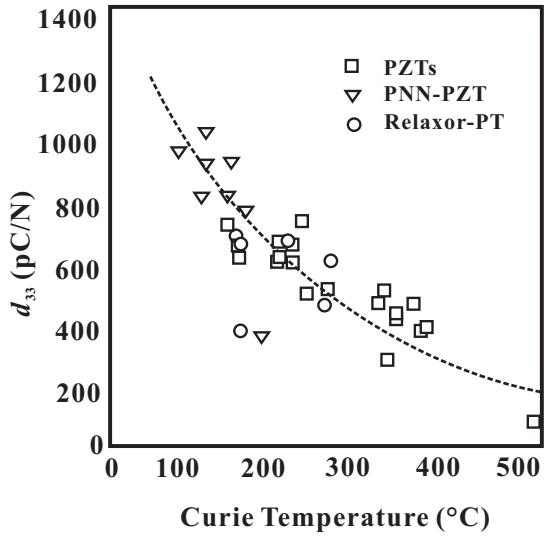


Figure 1.3: Piezoelectric coefficient d_{33} as a function of transition temperature T_c [22]

The Curie temperature, T_c, is also an important characteristic for ferroelectric crystals. The ferroelectric materials undergo a structural phase transition from a high-temperature phase

to a low-temperature ferroelectric phase. The temperature of the phase transition is called the Curie point, T_c. In addition, the dependence of piezoelectric properties on Curie temperature for a variety of materials is shown in figure 1.3. From this result, the piezoelectric activity of ferroelectrics is enhanced through adjusting T_c downward. Generally, small amounts of substitutional alloying elements are doped into the ferroelectric crystals to change the Curie point.

1.3 Single crystal ferroelectrics

1.3.1 High performance of single crystal

Conventional polycrystalline ceramics, such as PZT, a solid solution of lead titanate and lead zirconate, are widely used for their superior piezoelectric behaviour and their linear relation between strain and electric field. Yet the level of strains that can be achieved in PZT is limited. Lots of attempts have been made at achieving large strain actuation [14, 22]. Most notable amongst these is the introduction of single crystal 'relaxor' materials following the work of Park and Shrout, who demonstrated up to 1.7% electrostrictive strain in PZN-PT (a solid solution of lead zirconate niobate and lead titanate) with very little hysteresis [22]. Alternatively, exploiting domain switching in single crystals is proposed to obtain large strain behaviour [14].

Compared to polycrystalline ceramics, single crystals possess high performance in supplying large electrostrictive strain. The remarkable properties of single crystals have inspired a few applications. Ultrasonic and sonar transducers with improved bandwidth and sensitivity could be obtained due to high electromechanical coupling factors ($\sim$0.9) and a wide range of dielectric constants ($\sim$1000 to 5000) of relaxor single crystals [23]. Ritter $et\ al.$ built ultrasonic transducers using a single crystal PZN-PT composite and an increase in bandwidth (by 141%) and sensitivity were observed [24]. Other applications such as transducers for medical imaging [25], single element ultrasonic probe [26], accelerometer with enhanced signal-to-noise

ratio [27], stack actuators for vibration damping and sonar highlighted the usefulness of relaxor single crystals [28]. The potential of lead-free single crystals has also been realized for sensor and actuators applications [29]. Conventional polycrystalline ceramics such as PZT and single crystals of PMN-PT, PZN-PT contain the toxic element lead (Pb) which has detrimental environmental and health effects [30, 31]. There is a need to develop lead-free ferroelectric materials, and hence materials such as barium titanate have been a focus of recent research, especially for medical imaging application due to low acoustic impedance.

1.3.2 Challenge of single crystal

Single crystals are difficult to grow, especially obtaining large single crystals ($\sim$100 mm diameter) with uniformity at low costs is very challenging. Methods for growing single crystals include flux technique [32], Bridgman or modified Bridgman method [33], top seeded solution growth (TSSG) method [34], Czochralski method [35], solid-state single crystal growth methods, templated growth method [36] etc. Manufacturing single crystals has been an active area of research for over 50 years. Though there has been good progress in resolving the process related issues, high costs are associated with single crystal manufacturing, removal of needle domains, and cracking of crystals during manufacturing.

Most ferroelectric materials exhibit a fracture toughness similar to that of glass (0.7-0.8 $MPam^{1/2}$), and single crystal ferroelectrics whose fracture toughness is about 0.2-0.6 $MPam^{1/2}$ are also no exception. Their inherent brittleness makes them susceptible to fracture, especially for applications involving strong mechanical and electrical cyclic loading conditions. The existence of cracks influences the domain switching and the working performance in applications. The reason is that domain switching in ferroelectric materials with cracks can be easily activated near the crack tip by the intensive fields, even when the applied field is not large enough to induce overall domain switching. Since it is rather difficult to characterize domain switching near the crack tip in ferroelectrics, several researchers recently focused on domain switching in

situ-experiments and crack propagation in ferroelectric single crystals [37, 38]. Notably, stripe domain structures (needles) are observed near the crack tips of single crystal ferroeletrics under an electric loading opposite to the original poling direction [38].

1.4 $BaTiO_3$ single crystals

Barium titanate ($BaTiO_3$) is a ferroelectric material of the perovskite class. $BaTiO_3$ single crystals undergo a structural phase transition from a paraelectric phase to a ferroelectric phase upon cooling through the Curie temperature T_c, about $120°C$. During this transition process, $BaTiO_3$ single crystals transform from a cubic (point group $m3m$) state to a tetragonal state (point group $4mm$) with a spontaneous polarization along the $< 0\ 0\ 1 >$ direction, as shown in figure 1.4. With further cooling, $BaTiO_3$ single crystals experience other phase transitions passing through tetragonal, orthorhombic, and rhombohedral phases [12, 39], which are presented in figure 1.4. At high temperature, it has the cubic phase, which is depicted in figure 1.5a, containing a Ba^{2+} ion at each corner of the unit cell, a Ti^{4+} ion at the centre of the unit cell, and an O^{2-} ion at the centre of each face. In figure 1.5b, the tetragonal unit cell results from the following distortion of the original cubic cell: one of the cube edges is elongated to become the tetragonal c axis, the two other cube edges are compressed to become the tetragonal a axis [40, 41].

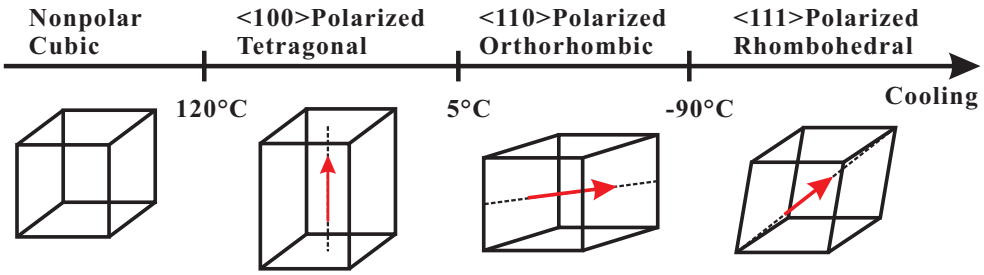


Figure 1.4: Various crystalline phases of $BaTiO_3$ with cooling temperature modified from [12].

This distortion is depicted schematically in figure 1.5b. During the process of phase transition through Curie point, the tetragonal unit cell develops a dipole moment due to displacement

of the central Ti^{4+} ion relative to the surrounding O^{2-} ions. This polar structure results from the coupling consequence between structural distortion and ion motion.

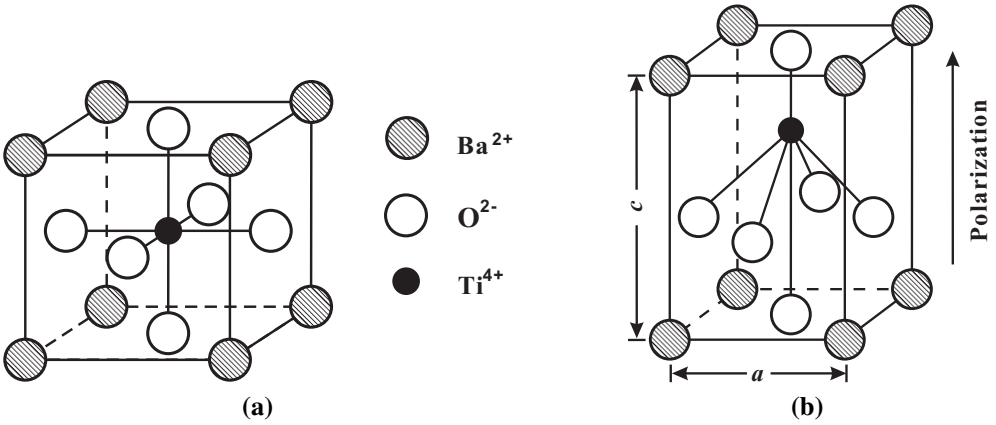


Figure 1.5: $BaTiO_3$ crystal structures of unit cell in cubic and tetragonal phases [14]

Table 1.1: Material constants of $BaTiO_3$ in tetragonal phase with polarization direction of [0 1 0] [14, 39, 42]

	$BaTiO_3$ single crystal
Structure	Tetragonal ($4mm$)
Density, ρ (kg/m^3)	6.02×10^3 (20°C)
Lattice parameter, a (Å)	3.992 (20°C)
Lattice parameter ratio, c/a	1.011 (20°C)
Curie temperature, T_c (°C)	120 (25°C)
Spontaneous polarization, p_0 (C/m^2)	0.26 (25°C)
Spontaneous strain, $\varepsilon_0 = 2(c-a)/3a$	0.0073 (20°C)
Elastic stiffness, C (GPa)	211(C_{11}), 114(C_{12}), 107(C_{13}),160(C_{22}), 56.2(C_{44}), 127(C_{55}) (25°C)
Piezoelectric coefficients, e (C/m^2)	32.6(e_{16}), -3.88(e_{21}),5.48(e_{22}) (25°C)
Dielectric constants, κ	1980(κ_{11}/ κ_0),48(κ_{22}/ κ_0), $\kappa_0 = 8.854 \times 10^{-12}$ (F/m) (25°C)

At room temperature, $BaTiO_3$ single crystal exhibits tetragonal symmetry. The tetragonal phase of barium titanate has been the object of much investigation, since this phase is structurally simple and also stable at room temperature. The configuration parameters of tetragonal $BaTiO_3$ single crystal are given in table 1.1, and the anisotropic material constants with the direction of polarization along $< 0\ 1\ 0 >$ are also provided. The contracted notation assigning

11 to 1, 22 to 2, 33 to 3, 23 or 32 to 4, 13 or 31 to 5, 12 or 21 to 6 is employed. Considering lattice structure ($4mm$) and the direction of polarization, the matrix form of material constant is presented in Eq. 1.1. The 6×6 matrix of the elastic constants C has 6 independent variables. The 6×3 matrix of the piezoelectric constants e has 3 independent variables. The 3×3 matrix of the dielectric constants κ has 2 independent relative dielectric constants.

$$C = \begin{bmatrix} C_{11} & C_{12} & C_{13} & 0 & 0 & 0 \\ C_{12} & C_{22} & C_{12} & 0 & 0 & 0 \\ C_{13} & C_{12} & C_{11} & 0 & 0 & 0 \\ 0 & 0 & 0 & C_{44} & 0 & 0 \\ 0 & 0 & 0 & 0 & C_{55} & 0 \\ 0 & 0 & 0 & 0 & 0 & C_{44} \end{bmatrix} \quad e = \begin{bmatrix} 0 & e_{21} & 0 \\ 0 & e_{22} & 0 \\ 0 & e_{21} & 0 \\ 0 & 0 & e_{16} \\ 0 & 0 & 0 \\ e_{16} & 0 & 0 \end{bmatrix} \quad \kappa = \begin{bmatrix} \kappa_{11} & 0 & 0 \\ 0 & \kappa_{22} & 0 \\ 0 & 0 & \kappa_{11} \end{bmatrix} \tag{1.1}$$

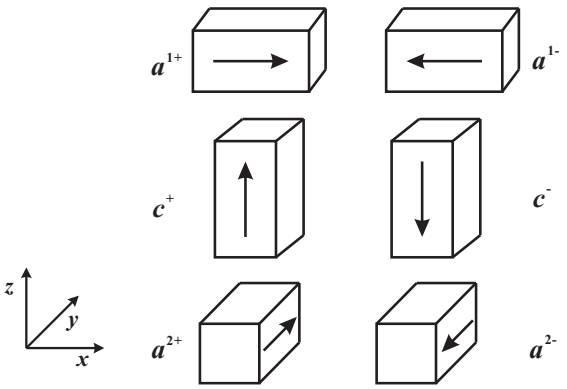


Figure 1.6: Six equivalent variants of polarization in tetragonal phase

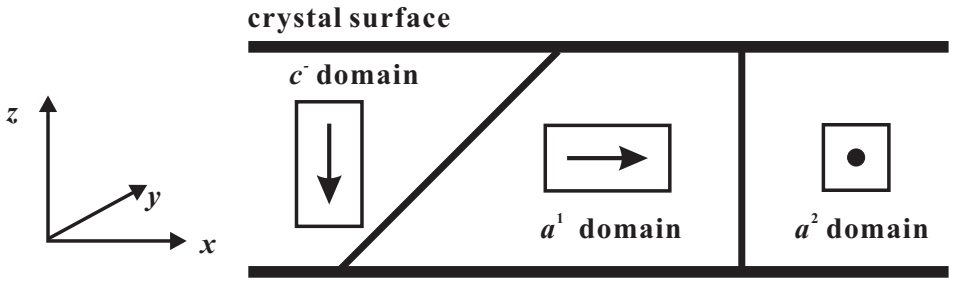


Figure 1.7: Schematic diagram of a^1, a^2, and c domains

A ferroelectric domain is a region within a ferroelectric in which the spontaneous po-

larization is uniformly oriented. $BaTiO_3$ in the tetragonal phase has six possible direction of polarization, shown in figure 1.6. In a crystal plate of barium titanate, a domain with the polarization direction perpendicular to the crystal surface is defined as "c domain", while a domain with the polarization direction parallel to the crystal surface is classified as "a domain". The definitions of a domain and c domain are given by Merz [43]. The a-type domain can be subdivided into a^1 domains with polarization along the x axis and a^2 domains with polarization along y axis. The domains with polarization direction along positive axis are a^{1+}, a^{2+}, and c^+; in contrast, the polarization direction of a^{1-}, a^{2-}, and c^- domains points to the negative axis. (figure 1.7)

The interface between two domains is called a domain wall. In ferroelectrics, the width of domain walls is typically small on the scale of a few nm or less. For Barium Titanate in a tetragonal ferroelectric phase, there are two types of domain wall, 90° domain wall and 180° domain wall. Figure 1.8a and 1.8b show the lattice configuration and macro structure for 90° and 180° domain walls. The 180° domain wall is a boundary between domains with antiparallel polarization, as indicated by the A-A' line in figure 1.8. Alternatively, a 90° domain wall is defined as a boundary which separates two adjacent domains polarized at 90° to each other, as shown in figure 1.8a. There are two types of arrangements for 90° domain wall, c-a and a-a. The 90° c-a domain wall which is indicated by the line b-b' in figure 1.8b goes through the crystal at an angle of 45° to the major surface. An alternative 90° a-a domain wall goes straight through the crystal at 90° to the major surfaces, as shown in figure 1.8b, the line c-c'. Little [44] found experimentally that a 90° wall is actually an $88^\circ 30'$ rotation of crystal lattice. As the lattice parameter ratio of $BaTiO_3$ single crystal with tetragonal phase is $c/a = 1.011$, the skew angle between the domain wall and polarizing axis is $44^\circ 15'$. However, the most studies treat 90° domain wall as the wall separating two domains with perpendicular polarization direction for convenience, which do not influence the domain compatibility. In contrast to the straight 90° domain wall through the crystal, the 180° domain wall structures are often observed as wavy 'watermarks' in ferroelectric crystals, as can be seen in figure 1.9 [45]. The above three

types of domain wall are compatible: there is no net charge and no dislocation built up on the wall. For compatibility, the normal component of electrical polarization and lattice strain are continuous for two adjacent domains; compatibility will be further discussed later. The $180°$ domains can be reversed with minimal structural strains. However, switching of $90°$ domains requires a significant structural deformation.

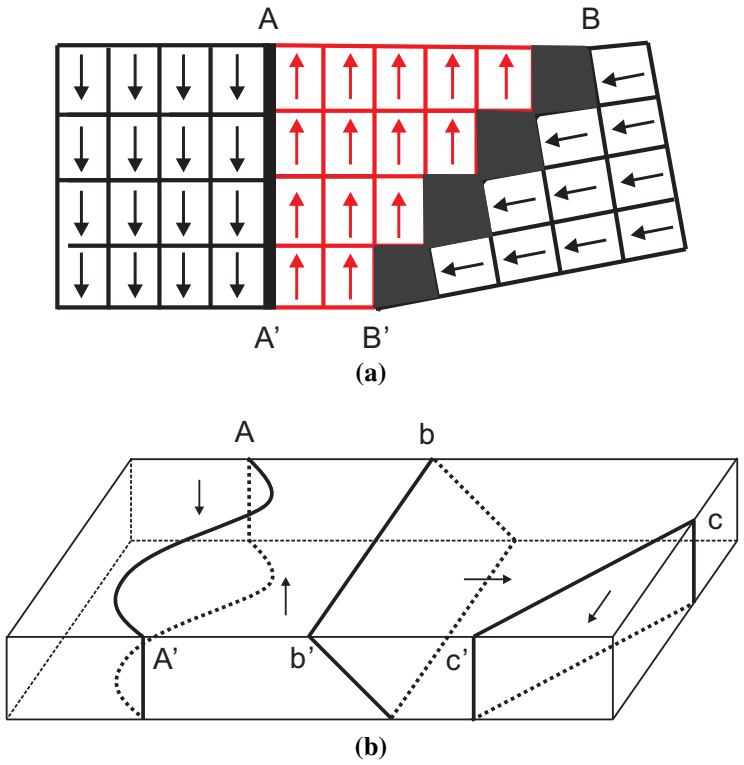


Figure 1.8: (a) Lattice configuration (b) Macro structure for $180°$ and $90°$ domain walls in a crystal plate



Figure 1.9: Herringbone pattern with watermarks formed by $180°$ domain in $BaTiO_3$ cermics [45]

1.5 Needle domains

1.5.1 Structure and arrangement of needle domains

Needle-shaped or wedge-shaped domains are investigated very frequently in ferroelectric single crystals [46–49]. The terms “needle-shaped domain” or “wedge-shaped domain” stem from the description of the domain structure and motion. Figure 1.10 shows the schematic structure of 2-D needle domains. Generally, a needle-shaped domain refers to a long slender domain with a round or sharp tip, as shown in figure 1.10a. This kind of domains normally appears during manufacture of single crystals. Typically, motion of needle domains responding to external loads is by extension or retraction along the longitude direction, without sideways motion. The term “wedge-shaped” domain refers to a triangular domain, as shown in figure 1.10b. Motion of wedge domains is characterised by a combination of lengthening and broadening in response to external loads. Wedge domains are commonly produced during polarization switching of antiparallel domains. Merz [43] found that the nucleation of new wedge shaped domains happened during polarization reversal in ferroelectrics. In practice, needle shaped domains can have long, shallow wedge shapes at their tips and so the distinction between wedge and needle domains is arbitrary. As shown in figure 1.11, microstructures of the needle domains in the $BaTiO_3$ single crystals are observed experimentally. The terms “needle” and “wedge” are used almost interchangeably in the literature.

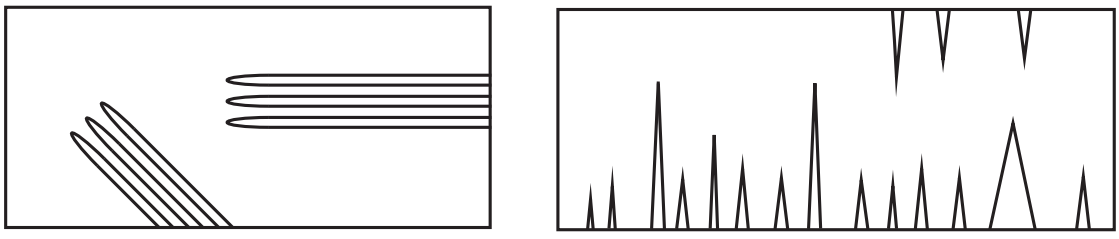


Figure 1.10: (a) Needle-shaped domains with round or sharp tip (b) Wedge-shaped domains

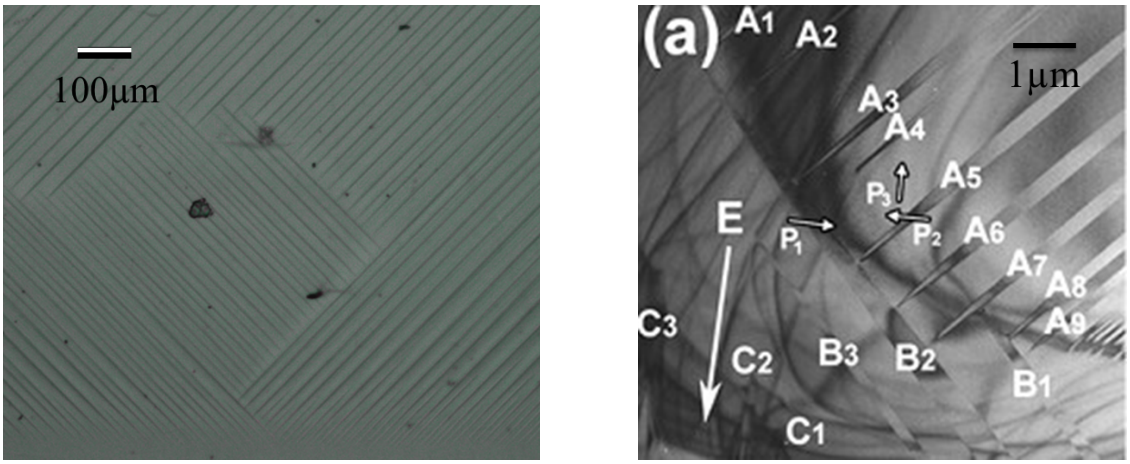


Figure 1.11: (a) Needle-shaped domain observed by optical microscope (b) TEM micrographs showing needle-shaped domains in the $BaTiO_3$ single crystals [50]

The needle domains are a common microstructure in ferroelectrics. They are usually generated when the temperature is cooling through the Curie temperature for the single crystal. The reason is that the formation of a needle domain allows strain at the boundary during annealing. Therefore, perfect single crystals, which possess high performance, are hard to manufacture. In addition, the arrangement of needle domains adopts certain patterns, as shown in figure 1.12. Two typical patterns are herringbone (or 'chevron') and comb patterns. They are observed in experiments, as shown in figure 1.12b and 1.12c, respectively. The needle domains are actually laminae in 3-dimensions, with the needle tip corresponding to the edge, as shown in figure 1.13. The tip of needle domain terminates within the crystal, as seen in the needle domains (group A) shown in figure 1.13. Laminar structure (group B) is obtained when the needle tip is promoted to grow through the whole specimen. The propagation of needle domains is usually influenced by the external loads. When the external force is small, the shape of the needle does not change during the movement, only the needle shaft becomes longer or shorter without sideways movement. The needle domain is also sensitive to temperature.

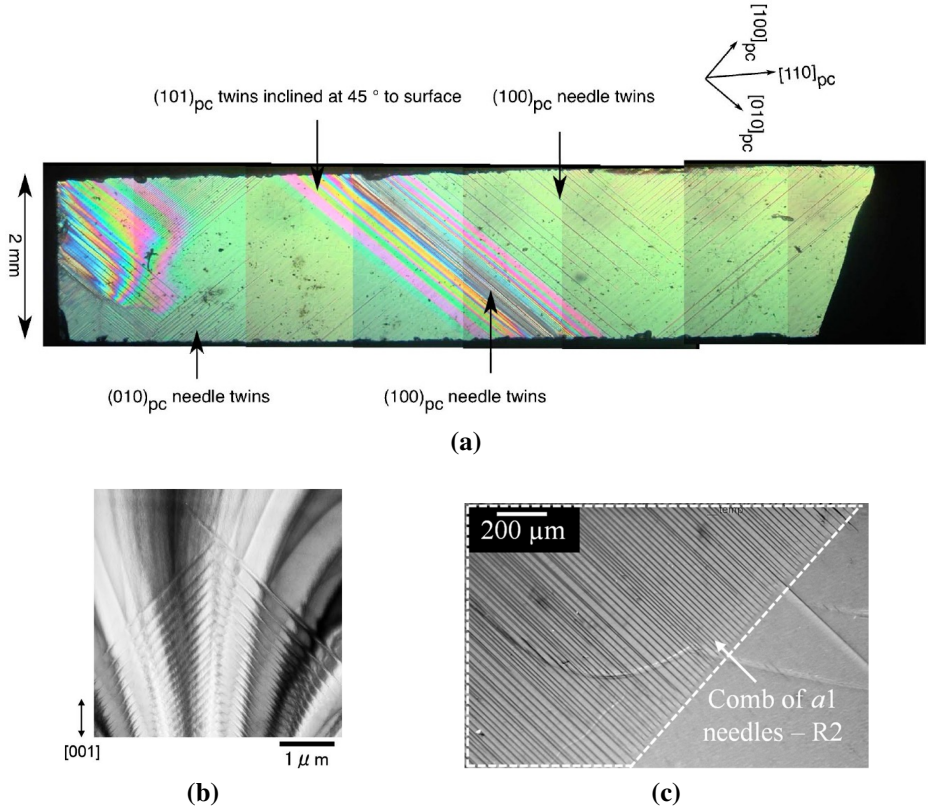


Figure 1.12: (a) Needle domain observed in $LaAlO_3$ single crystal [48], the subscript 'pc' is used to denote pseudocubic indices; (b) Herringbone pattern needle domains in $BaTiO_3$ single crystal observed by TEM [51]; (c) Comb pattern of needle domain in $BaTiO_3$ [52].

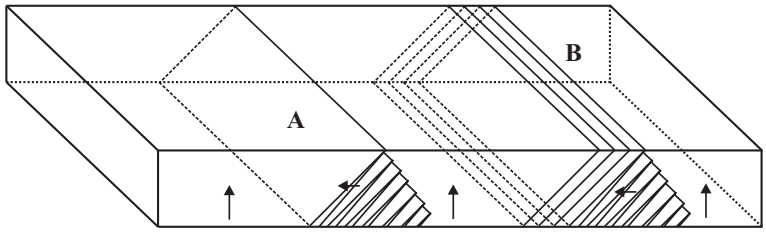


Figure 1.13: 3-D laminar structure composing of needle domains

1.5.2 Review of needle domain research

With the development of thin-film technology for the fabrication of ferroelectric memories, the investigations of the physical properties of domains and domain walls in ferroelectrics have increased in importance. The reason is that the propagation of needle domains does not only affect the manufacture of single crystals, but is also the most common switching mechanism. In additional, a better understanding of needle domains improves the study of cracking in fer-

roelectrics, which is a limiting factor on their working reliability.

Several researchers have investigated the behaviour of needle-shaped domains through theoretical and experimental methods [12, 48, 53–55]. In early work, Forsbergh [12] observed twinning domains growing in Barium titanate single crystals and summarized the predominant twinning forms in the different ferroelectric phases. At room temperature, it was found that the existence of needle domains was in two forms: 90° a-c and 90° a-a for $BaTiO_3$ single crystals with tetragonal phase. In addition, the surface charge existing at the needle tip was considered. Bornarel el al. [53–55] have also investigated the interaction and evolution of needle domains in ferroelectric KH_2PO_4 through theoretical and experimental methods. The needle domains in KH_2PO_4 were observed, their motion and interaction was investigated under an applied electric field [53]. Evidence was found for the existence of long-range interaction, up to $200\mu m$ between the domains. Based on the observed experimental results, Bornarel $et\ al.$ [54, 55] devised a model of a needle domain tip as assemblies of edge dislocations. Accordingly, the fields due to a needle domain and interaction of needle domains can be analysed by using the classical theory of the edge dislocation, for the purpose of further understanding the experimental results and studying the interactive behaviours.

Salje and Bueble $et\ al.$ [46–48, 56, 57] researched needle domains in $LaAlO_3$ and $SrTiO_3$, which are analogs of the (Me, Fe)SiO_3 perovskite thought to be a major component of the Earth's lower mantle. The authors [46, 47] discussed theoretically the formation of needle shaped domains at the mesoscopic scale. They argued that nearby domain wall corners, if sufficiently close are strongly attracted to each other via the elastic distortion of the crystal, and finally merge to form a needle domain with a sharp tip. Harrison $et\ al.$ [56] further experimentally studied the needle domains growing in $LaAlO_3$ single crystals using three-point bending. The sample undergoes a cubic to rhombohedral phase transition at 550°C, leading to the generation of characteristic 'chevron' twins, as shown in figure 1.14. The dynamical response of needle domains in $LaAlO_3$ single crystals under weak elastic stress are investigated

through optical observation and themodynamic analysis [48, 57]. They mainly concentrate on the propagation of needle domains rather than the sideways movements of domain walls, which will happen at large loading. It is found that the propagation of a single ferroelastic needle domain under weak elastic stress consists of two parts: a continuous front propagation and jerky avalanches.

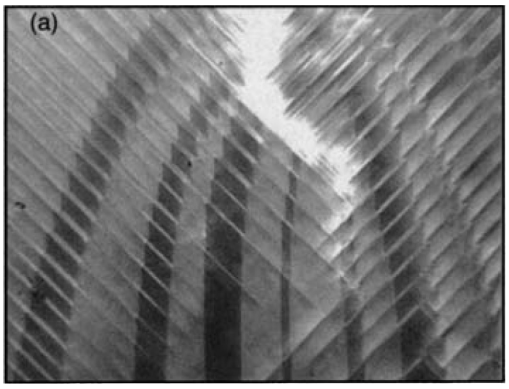


Figure 1.14: Optical micrograph showing the boundary between incompatible chevron orientations in $LaAlO_3$ single crystal [56].

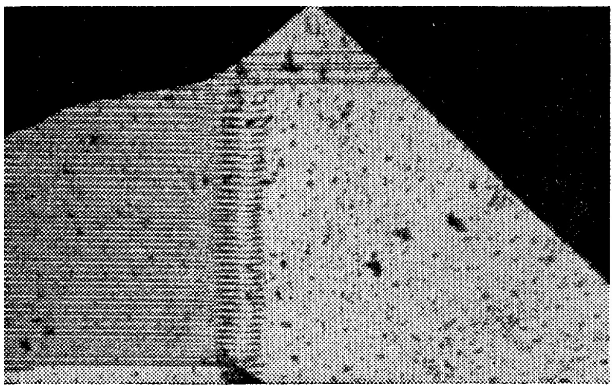


Figure 1.15: Comb needle observed by Little in $BaTiO_3$ single crystal [44].

The propagation of needle domains in ferroelastic materials is related to their switching mechanism. Little [44] made an early study of needle domains in $BaTiO_3$ single crystals. In the tetragonal phase of this material, the typical width of needle-shaped domains is 10-30μm. He found that 90° needles are nucleated at the crystal boundaries when the electric field perpendicular to initial polarization direction increases to a critical field (E_c). After that, the needle domain will extend along longitude direction and also become wide across the crystal. When

the field is removed, the stresses caused in the crystal by the presence of 90° domain force the needle out of the crystal. They shrink slowly at first, then disappear suddenly. Additionally, the comb needle pattern which composes many needle domains terminating along the same line are observed in experiments, as shown in figure 1.15. Bornarel $et\ al.$ [58] report that the switching process in the ferroelectric crystals is related to the twinning dislocations which are created at the tip of needle domain.

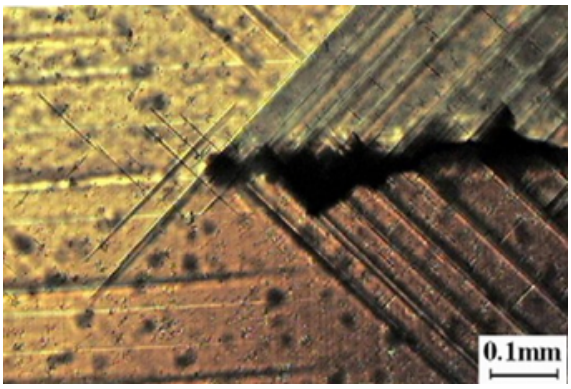


Figure 1.16: Needle domains existing ahead of the crack tip during crack propagation [16].

In addition, many researchers found that needle shaped domains appeared during the development of other microstructural features [16,50,51,59,60]. Fang $et\ al.$ [16] found that needle domains accompany the development of crack propagation. Needle domains appeared ahead of the crack tip during crack propagation, as shown in figure 1.16. Li $et\ al.$ [61, 62] adopted the phase-field model to investigate the nucleation and growth of needle domains near a stationary crack tip in a single crystal of ferroelectric material. Carka [63] further consider a phase-field model with periodic boundary conditions to simulate the fields due to needle-shaped domains. In fact, the existence of needle-shaped domains gives rise to high stress field and electrical field around needle tips in ferroelectrics. When the tips of comb-like needle domains are terminated at the same line, the high stress state at the tip front also induces the growth of cracks. Zhang $et\ al.$ and Duan $et\ al.$ observed 90° a-a needle domains using transmission electron microscopy (TEM) when they investigated the switching mechanism of multi-domains in $BaTiO_3$ single crystal [50, 59, 60]. Matsumoto $et\ al.$ [51] investigated the effect of the thickness of a $BaTiO_3$

single crystal thin film on the microstructure morphology; a herringbone pattern of needle domains was observed by TEM.

1.6 Layout of this thesis

The motivation for the current work, an introduction to ferroelectric materials and prior theoretical and experimental investigations have been reviewed in this chapter.

Chapter 2 builds a model of needle domains in ferroelectric crystals, based on mechanical and electrical compatibility, as well as considering their characteristic structure. The solutions derived by Barnett and Lothe for anisotropic piezoelectric media are utilized to analyse the coupling of stress and electric fields around needle domains. Additionally, modified Peach-Koehler forces on needle domains are proposed to assess the interaction of needle domains. The solution for the plane stress problem is obtained from the transformation of the existing plane strain solution.

Chapter 3 adopts optical microscopy to observe the microstructure and patterns of needle domains in $BaTiO_3$ single crystal. In the experimental observation, we find two commonly stable arrangements of needle domains. Additionally, we use X-ray diffraction to distinguish the domain type in $BaTiO_3$ single crystal and detect the shape of the needle domain. The strain field due to the needle domain is also measured. The needle model built in Chapter 2 is used to calculate the strain field to compare with the result obtained from the experiment.

Chapter 4 discusses the simulation results of internal stress and electric fields produced by needle domains in $BaTiO_3$, which are modelled as an effective edge dislocation coupled with a line charge. First, the interaction of the pairs of needle domains in an infinite piezoelectric body is studied by computing the interactive force and the total energy. After that, groups of needle domains in comb-like and herringbone patterns are investigated. Considering the dominant effect of the electrostatic terms in the needle tip interactions, the influence of the varying

polarization charge existing at the needle tip on the interaction of needle domains is analysed. The evolution of groups of needle domains under the influence of external perturbation of the needle domains is also analysed. During the process of analysing the evolution of needle domains, a viscous model is proposed to simulate the motion of needle domains due to external perturbation. In addition, the study of domain bundle boundaries in barium titanate is used to further verify the model of needle domains.

Chapter 5 studies the boundary value problem based on the superposition theory proposed by Van der Giessen [64]. The influence of boundary conditions on the fields and arrangement of the needle domains is analysed in detail. Considering a typical situation which is that a thin $BaTiO_3$ single crystal has loads over the thickness of the plate, the plane stress assumption is adopted. The evolution of a pair of needle domains and comb-like needle domains are further studied under the action of the compressive step loads. In the analysis process, the lattice friction and plane stress condition and the viscous model are adopted.

Chapter 6 presents a discussion of the contents of this thesis and suggests improvements to the modelling. It also outlines directions for future research.

2

Chapter 2 Model of needle domains

In chapter1, we have introduced the microstructure of needle domains in ferroelectric crystals and reviewed researches about needle domains. However, the most current investigations about needle domains mainly focused on the experimental observation. There was few studies on modelling to explain the interaction and evolution of needle domains. But these modelling works didn't consider the anisotropic and electromechanical coupling properties which are two typical and important properties of ferroelectric crystal. In this chapter, considering the anisotropic and electromechanical properties, we will try to establish a new model of needle domains according to mechanical and electrical compatibility. The fields of dislocations and line charges are used to represent the effect of a needle domain on the surrounding material. An introduction to the Barnett and Lothe theory of a dislocation with a line charge is presented in this chapter. Modified Peach-Koehler forces on needle domains are proposed to describe their interaction.

2.1 Dislocations in crystals

Before discussing how to model the mechanical and electrical fields produced by needle domains, a brief introduction to edge dislocations in crystals is given in this section, for later use.

The fields around an edge dislocation in an isotropic medium are later used as a reference case.

2.1.1 Definition of edge dislocation

The concept of dislocations was originally introduced by Taylor, Orowan [65] and Polanyi to resolve the difference between the theoretical shear strength of metals and experimental measurements. An edge dislocation is a defect where an extra half-plane of atoms (EFGH in figure 2.1a) is introduced midway through the crystal, distorting nearby planes of atoms. The plane ABC is the dislocation slip plane. Dislocation line FG shown in figure 2.1a and 2.1b is defined as the boundary between the slip zone and non-slip zone over the dislocation slip plane, and is perpendicular to the slip direction. A positive edge dislocation is represented symbolically by $\perp$. In contrast, the symbol $\top$ is used to represent the negative edge dislocation, where the half-plane of atoms is inserted below the slip plane ABC.

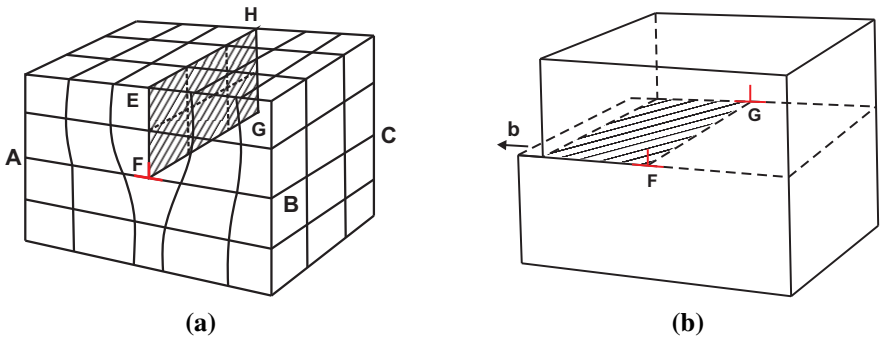


Figure 2.1: Schematic diagram of edge dislocation (a) atom structure, (b) from a continuum standpoint [66].

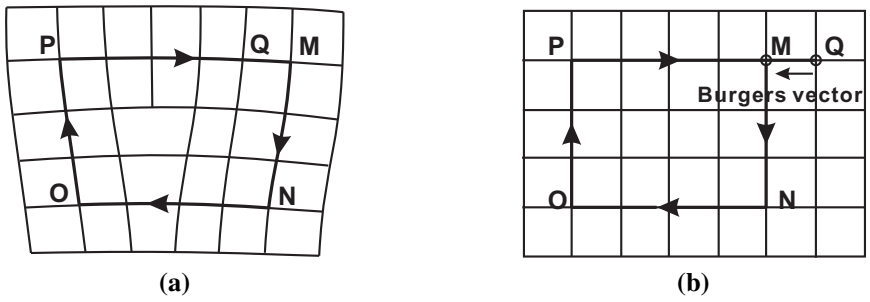


Figure 2.2: Burgers circle (a) in a crystal with edge dislocation (b) in a perfect crystal [67].

To describe the dislocation conveniently, the Burgers vector **b** was introduced by J.M. Burgers (1939) as a unique characteristic of a dislocation [68]. Burgers vector **b**, which is the slip displacement vector associated with the dislocation, is calculated by a closure failure of a Burgers circuit. A Burgers circuit is any atom-to-atom path taken in a crystal containing dislocations which forms a closed loop. Such a path (MNOPQ) is illustrated in figure 2.2a. However, the circle linked by the same atom-to-atom sequence in a perfect crystal, which is displayed in figure 2.2b, does not close. The vector required to make the circuit close, QM, is called the Burgers vector **b**. Thus in an edge dislocation, the Burgers vector is in the slip plane normal to the dislocation line, and a single lattice spacing in magnitude.

2.1.2 Peach-Koehler forces

The existence of a dislocation in a crystal causes lattice distortion. Correspondingly, stress fields around the dislocation are produced. When the distance between two dislocations is small, their interaction may need to be considered. Peach-Koehler force [69] is proposed to describe the mechanical force exerted by a stress field on a dislocation, i.e. that stress field can come from other dislocations, boundary conditions, or any other source.

Considering two interacting dislocations (d_1 & d_2), with dislocation lines along the z-direction, the Peach-Koehler force **F** on d_2 in the x-y plane can be calculated as follows [70],

$$\mathbf{F} = \begin{bmatrix} b_x & b_y & b_z \end{bmatrix} \begin{bmatrix} \sigma^1_{xx} & \sigma^1_{xy} & \sigma^1_{xz} \\ \sigma^1_{yx} & \sigma^1_{yy} & \sigma^1_{yz} \\ \sigma^1_{zx} & \sigma^1_{zy} & \sigma^1_{zz} \end{bmatrix} \begin{bmatrix} \mathbf{i} \\ \mathbf{j} \\ \mathbf{k} \end{bmatrix} \times \mathbf{k} \tag{2.1}$$

Hence:

$$F_x = (b_x\sigma^1_{xy} + b_y\sigma^1_{yy}) \tag{2.2a}$$

$$F_y = -(b_x\sigma^1_{xx} + b_y\sigma^1_{yx}) \tag{2.2b}$$

where, b_x, b_y and b_z are the components of Burgers vector of dislocation d_2 along x, y and z axis. The stress field produced by the dislocation d_1 is denoted by σ^1_{ij}. The unit vectors **i**, **j**, and **k** are along the direction of coordinate x, y and z, respectively. F_x and F_y represent the components of Peach-Koehler force **F** along the x and y directions. In practice, the stress field (σ^1_{ij}) in Eq. 2.1 which acts on the edge dislocation d_2 with Burgers vector $\mathbf{b} = [b_x\ b_y\ b_z]$ can be generated by external loading or other dislocations.

The interaction of two dislocations has been investigated by many researchers [69–71]. The Peach-Koehler force of two parallel dislocations is commonly considered. The interaction force which is parallel to the slip plane can cause slip movement along the slip plane. Alternatively, the interaction force which is perpendicular to the slip plane can result in climbing. Taking an example of slipping force , the classical results are shown in figure 2.3. The spacing of two parallel dislocation is y. The solid line represents the force F_x along x-axis of two identical dislocations. While the dotted line describes the slip force for two opposition dislocations. Without considering any other effects clamping the dislocations, the equilibrium state corresponds to the slipping force $F_x = 0$. From figure 2.3, we find that the equilibrium state occurs at the horizontal positions 0, y and -y. However, the stability of these equilibrium positions should also be considered.

To discuss the equilibrium stability of the interactive dislocations, we take an example of two identical parallel dislocations in an isotropic material with the elastic constants are $c_{11} = 240$GPa, $c_{12} = 120$GPa, and $c_{66} = 60$GPa, the Burgers vectors of dislocation d_1 and d_2 are selected as $[1\ 0\ 0]$. The contour map of the interaction force F_x was computed using Matlab and is shown in figure 2.4a. For later comparison with needle domains, the horizontal and

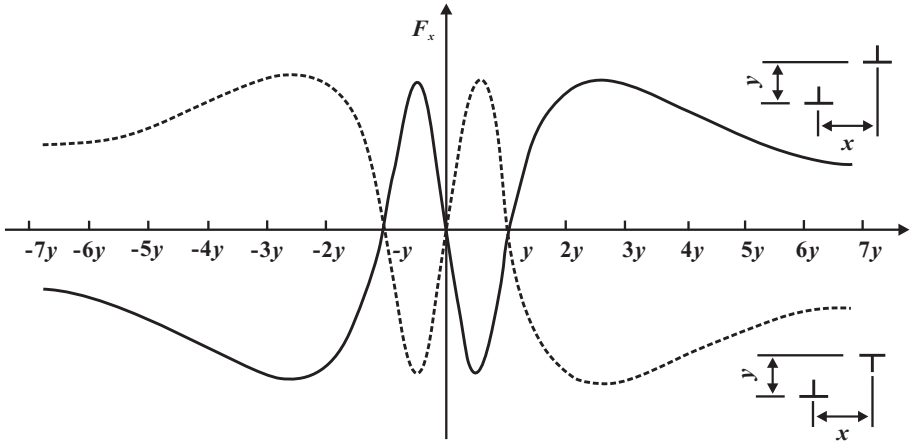
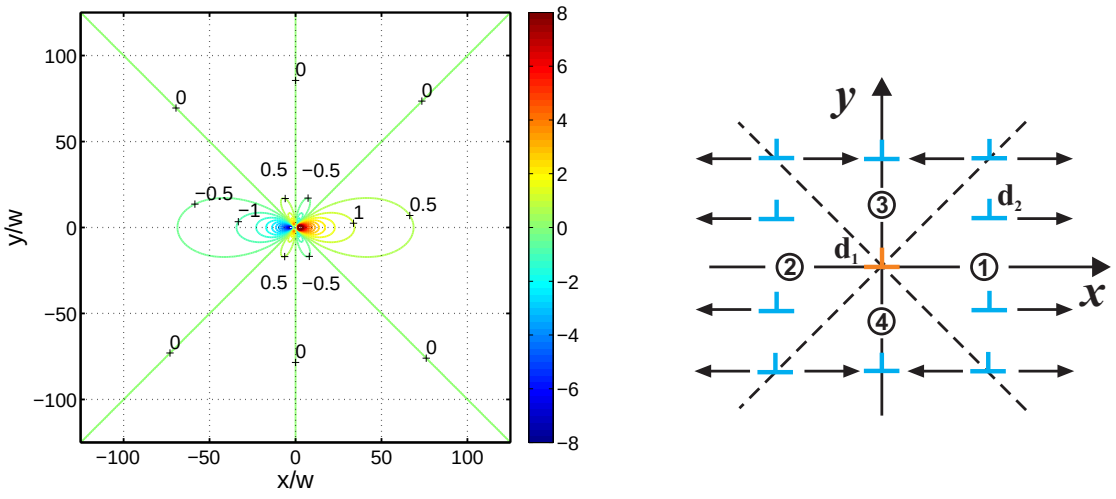


Figure 2.3: Peach-Koehler force of two parallel dislocations along x axis (modified from [70]).



(a) **(b)**

Figure 2.4: Peach-Koehler force on dislocation (a) slip force F_x contour map (b) Interaction between two dislocations in x direction

longitudinal ordinates (x and y) are normalized by $w = 10\mu m$, and the force F_x is normalized by $\sigma_0\varepsilon_0 w$, where $\sigma_0 = 2.6$MPa, and $\varepsilon_0 = 0.01$. The detailed information about nondimensionalization will be stated in section 4.1. Note that there is no slip force when dislocation d_2 is situated at the lines of $y = \pm x$ and $x = 0$, which are in agreement with the well-known results shown in figure 2.3 (solid line). The location at $x = 0$ is the stable equilibrium position. This means that if a dislocation deviates from this stable equilibrium position, the interaction force

serves as a restoring force to draw it back. This can be seen from the signs of the forces F_x in figure 2.4a. However, the location at $y = \pm x$ is the unstable equilibrium position where any pertubation will result in movement further away from this position under the effect of interaction force. Based on these results, the relationship between two identical dislocations for the isotropic medium is presented schematically in figure 2.4b.

2.2 Domain compatibility

In this section, we discuss the compatibility of a pair of ferroelectric domains. Which factors determine the orientation of a domain wall? Which laws determine the arrangement of ferroelectric domains? This will turn out to be important because it will define the directions in which domain needles form and grow.

2.2.1 Minimum energy

The principle of minimum energy is a fundamental concept used in structural analysis and modelling. It asserts that an equilibrium state is a state with minimum energy. Accordingly, the domain pattern is expected to adopt an energy minimum configuration at equilibrium.

Consider a ferroelectric single crystal that occupies the space region $\Omega \in R^3$ with the boundary $\partial\Omega$, with the dead load $\mathbf{t}_0$ and electric field $\mathbf{e}_0$, as shown in figure 2.5. The total energy $\mathbf{U}$ is a function of displacement field $\mathbf{u}$ and electric polarization field $\mathbf{p}$. Shu and Bhattacharya [72] argued that the total energy could be written as:

$$\mathbf{U}(\mathbf{u},\mathbf{p}) = \int_\Omega \left(\frac{1}{2}\nabla\mathbf{p}\cdot\mathbf{A}\nabla\mathbf{p} + W(\varepsilon,\mathbf{p})\right) d\mathbf{x} - \int_\Omega \mathbf{e}_0\cdot\mathbf{p}\, d\mathbf{x} - \int_{\partial\Omega} \mathbf{t}_0\cdot\mathbf{u}\, d\mathbf{S} + \frac{\xi_0}{2}\int_{R^3} |\nabla\phi|^2\, d\mathbf{x} \tag{2.3}$$

where $\mathbf{A}$ is a positive matrix, ϕ is electrical potential, and $\xi_0 = 8.854\times10^{-12}\mathrm{C}^2\mathrm{N}^{-1}\mathrm{m}^{-2}$ is the permittivity coefficient of free space. The physical interpretation of each term is as follows: the

first term is interpreted as the domain wall energy resulting from the spatial change of polarization. Its value depends on the gradient of polarization $\nabla \mathbf{p}$, which means that the distribution of polarization tends to be uniform to achieve minimum energy. However, if the size of the crystal is large enough (the scale depends on the largest eigenvalue of the matrix $\mathbf{A}$), the crystal can contain several domains because this term becomes negligible, compared to other terms in Eq. (2.3).

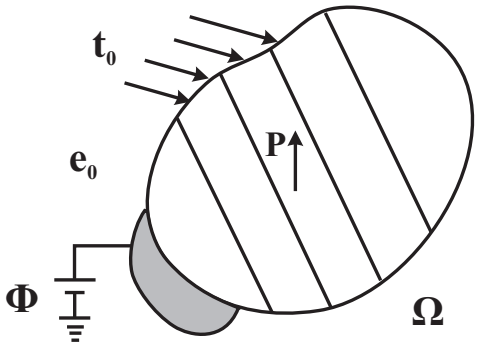


Figure 2.5: A ferroelectric system applied by a dead load $\mathbf{t}_0$ and external electrical field $\mathbf{e}_0$ (modified from [72])

The second term is the free energy density $W(\varepsilon, \mathbf{p})$, which is a function of strain and polarization, representing the stored energy arising from strain and polarization. Therefore, for equilibrium states, the crystal tends to minimise W, which has a well structure. This leads to material points adopting one of a small number of polarisation states, corresponding to the minima of W. In $BaTiO_3$, the minima of W correspond to the six polarization states that were shown in figure 1.6. The third and fourth terms are the potential energy of external electric field $\mathbf{e}_0$ and external mechanical load $\mathbf{t}_0$, respectively. For the third term, the direction of polarization will align with the external electrical field for minimum energy. The fourth term is written as a surface integral involving tractions, which is convenient when considering externally applied mechanical forces. However, it could equally be written as a volume integral involving stresses and strains. This term thus tends to align the strains and stresses in a tensorial sense, so as to minimise energy. The last term is the electrostatic self-energy induced by the electric field in the space occupied by the ferroelectric crystal. The minimum of this term produces an electrical

compatibility condition at the domain wall. We postpone the corresponding discussion to the next section 2.2.2.

To sum up, based on Eq. (2.3), there are the four factors controlling the orientation of a domain wall in the absence of external loading [49]: (1) in stable equilibrium, the domain structures and domain wall orientations should correspond to a local energy minimum; (2) electrical compatibility related to the different spontaneous polarization in the neighbouring domains should be satisfied; (3) mechanical compatibility related to the different spontaneous strains in the neighbouring domains should be satisfied; (4) minimum energy of domain walls.

2.2.2 Electrical and mechanical compatibility

In most practical situations, factors (2) and (3) mentioned in section 2.3.1 play the decisive role in determining the orientation of domain walls. In this section, we will mainly discuss the electrical and mechanical compatibility of the domain wall separating a domain pair.

The electrical compatibility can be deduced from the final term of minimum energy expressed as Eq. (2.3). Going back to final term ($\frac{\xi_0}{2}\int_{R^3}|\nabla\phi|^2\,d\mathbf{x}$), we note that this term is positive, and thus minimum energy requires that the gradient of electric potential, or electric field, be zero. This in turn requires that polarization $\mathbf{P}$ be divergence free:

$$\nabla\cdot\mathbf{P}=0 \tag{2.4}$$

Effectively, this states that the presence of free charge is energetically unfavourable. For a domain pair separated by a domain wall with normal vector $\mathbf{n}$, the two adjacent domains are characterized by spontaneous polarization vectors $\mathbf{P}^i$ and $\mathbf{P}^j$, see figure 2.6. The condition of domain wall neutrality results in

$$(\mathbf{P}^i-\mathbf{P}^j)\cdot\mathbf{n}=0 \tag{2.5}$$

This indicates that the normal component of the polarization vectors is continuous across the domain wall, as shown in figure 2.6. If satisfying the compatibility condition Eq. (2.5), there is no free charge at the domain wall. In contrast, domain walls which cannot satisfy Eq. (2.5) are classified as charged domain walls, and have increased electrostatic energy, as discussed in the next section.

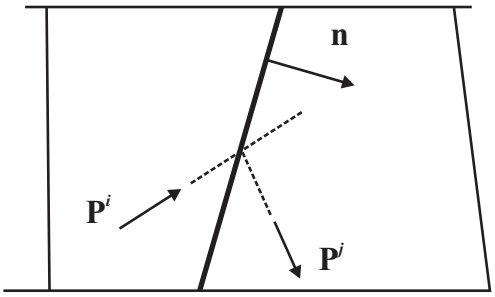


Figure 2.6: Compatibility of polarization and strain in a domain pair

For the tetragonal phase of $BaTiO_3$, two typical situations for mutual orientation of a planar wall and polarization vectors in neighbouring domains are illustrated in figure 2.7a and 2.7b. The figure 2.7a shows the so-called $180°$ wall; its electroneutrality is maintained due to the absence of polarization component normal to the wall. Figure 2.7b represents the so-called $90°$ wall which is also neutral because the polarization component normal to the wall is continuous on crossing the wall.

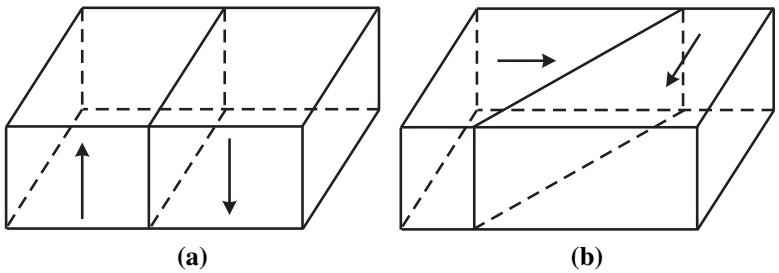


Figure 2.7: (a) $180°$ ferroelectric domain wall (b) $90°$ ferroelectric domain wall [49]

Besides electrical compatibility, the requirement of mechanical compatibility also restricts the orientation of the domain wall for a ferroelectric domain pair [49,72–74]. The tensors

$\boldsymbol{\varepsilon}^i$ and $\boldsymbol{\varepsilon}^j$ are the spontaneous strain in the neighbouring domains, respectively. The normal vector $\mathbf{n}$ of the domain wall which is an interface between adjacent domains is shown in figure 2.6. If $\boldsymbol{\varepsilon}^i$ and $\boldsymbol{\varepsilon}^j$ are suitably chosen, then adjacent domains can fit together at an interface with normal $\mathbf{n}$, without stress. This gives the following condition:

$$\boldsymbol{\varepsilon}^i - \boldsymbol{\varepsilon}^j = \frac{1}{2}(\mathbf{a} \otimes \mathbf{n} + \mathbf{n} \otimes \mathbf{a}) \tag{2.6}$$

where, $\mathbf{a}$ is an arbitrary vector. $\otimes$ is the dyadic product and thus $[\mathbf{a} \otimes \mathbf{n}]_{ij} = a_i n_j$. If $\boldsymbol{\varepsilon}^i - \boldsymbol{\varepsilon}^j = 0$, the strains satisfy compatibility for any vector $\mathbf{n}$ by making $\mathbf{a} = 0$. This is the case in figure 2.7a. If $\boldsymbol{\varepsilon}^i - \boldsymbol{\varepsilon}^j \neq 0$, a compatible wall may still be found, provided the matrix $\mathbf{M} = \boldsymbol{\varepsilon}^i - \boldsymbol{\varepsilon}^j$ is of rank 1. This case corresponds to figure 2.7b. The domain walls fulfilling the mechanical compatibility condition are called permissible walls or alternatively stress free walls [73]. Correspondingly, no additional elastic strains are involved.

2.3 Modelling of needle domains

The appearance of the needle domains affects internal stress and electrical fields in ferroelectric materials. Additionally, the interaction between nearby needle domains is also interesting and significant topic, especially for studying crack propagation. Therefore, a better understanding of interaction and evolution of needle domain structures can support the design of materials. However, previous works focusing on needle domains neglect both anisotropy and electromechanical coupling. In this thesis, we focus on 90° a-a needle domains and build a model to simulate the interaction and evolution of needle domains in $BaTiO_3$ single crystals, including the properties of crystalline anisotropy and electromechanical coupling. In this section, we try to clarify how the formation of needle domains depends on compatibility, how the existence of a needle domain affects the local mechanical and electrical fields, and how to evaluate the fields produced by the needle domain.

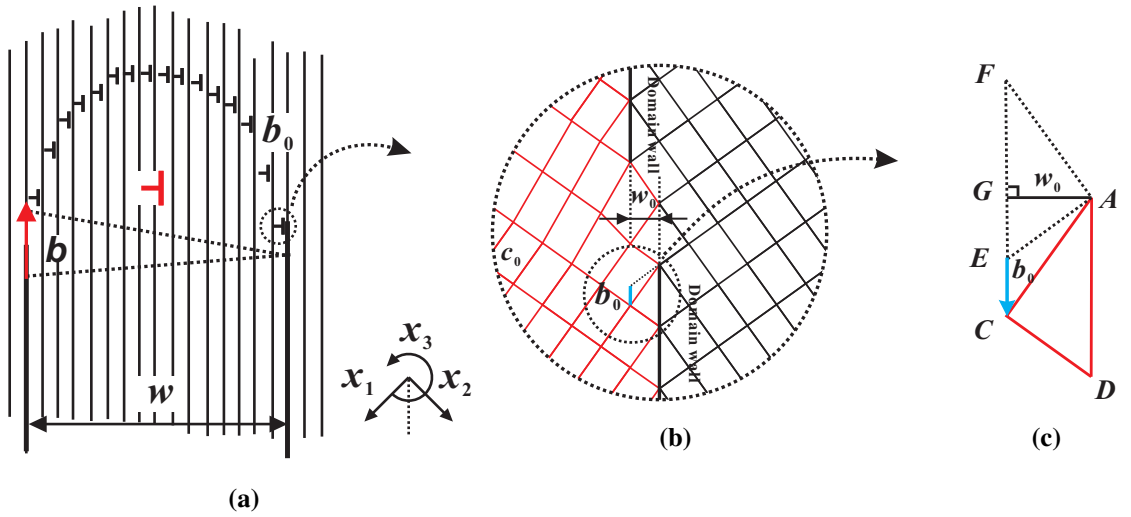


Figure 2.8: Schematic representation of the needle domain, (a) Needle tip as an assembly of equivalent dislocations modified from Bornarel [54], (b) An equivalent dislocation in the $BaTiO_3$ crystal structure, (c) Geometry of unit cells used for calculating Burgers vector $\mathbf{b}_0$

The formation of $90°$ a-a type needle domains results from $90°$ switching. Figure 2.8 shows the tip of one needle domain in a plane perpendicular to the x_3 axis. Here, the polarization vectors of the parent domain and needle domain are $\mathbf{P}^1 = [0\ 1\ 0]^T p_0$ and $\mathbf{P}^2 = [-1\ 0\ 0]^T p_0$, respectively. The two sidewalls of this needle domain are $90°$ domain walls, and satisfy the electrical and mechanical compatibility requirements for a stress-free and charge-free domain wall. However, incompatible jumps in spontaneous polarization and spontaneous strain happen near the needle domain tip.

Near the tip, where the domain walls cannot be in the minimum energy plane, the distortion can be thought of as a dislocation field. As shown in figure 2.8a and 2.8b, each step in the $90°$ domain wall produces a displacement b_0 parallel to the wall. The resulting distortion can be modeled using the fields of a dislocation on the domain wall. The needle tip fields can thus be approximated by those of an assembly of dislocations. Each equivalent dislocation has the Burgers vector $\mathbf{b}_0$, as follows:

$$\mathbf{b}_0 = \int_{c_0} d\mathbf{u} \tag{2.7}$$

where, c_0 is Burgers circuit surrounding the equivalent dislocation, as shown in figure 2.8b. And

u represents the displacement resulting from 90° domain switching.

Considering the thin width of needle domains, the concept of 'effective dislocations' with Burgers vector **b** is now proposed in order to estimate conveniently the field produced by all the dislocations assembling at the domain tip. Especially, the far field around one needle domain tip can be treated as that resulting from a single effective dislocation **b**. The calculation of the effective dislocation is the sum of all step dislocations b_0 through the whole width of needle domain, which are given as follows,

$$|\mathbf{b}| = \frac{w\,|\mathbf{b}_0|}{w_0} \approx 3\varepsilon_0 w \tag{2.8}$$

where, w is the width of the needle domain, and ε_0 is the spontaneous strain of the crystal lattice relative to the cubic state. The lateral step size w_0 can be expressed by the lattice parameters given in table 1-1, and hence is related to ε_0.

As shown in figure 2.8b, the black and red lattices on both sides of domain wall represent parent domain and needle domain, respectively. The corresponding polarization directions are perpendicular to each other. In figure 2.8c, triangle-AFE is the lattice position before switching, while triangle-ACD is lattice position after 90° switching. Due to 90° domain switching, the slipping displacement b_0 (EC) is created. According to the geometric relationship given in figure 2.8c, the slipping displacement b_0 and the lateral step size are calculated as follows,

$$w_0 = \frac{ac}{\sqrt{c^2 + a^2}} \tag{2.9a}$$

$$|\mathbf{b}_0| = \frac{c^2 - a^2}{\sqrt{c^2 + a^2}} \tag{2.9b}$$

where, a and c are the lattice parameters of the $BaTiO_3$ single crystal in tetragonal phase. The lines AF and AC are equal to c, and the lines AE and CD are equal to a.

From Eq. 2.8, we know the effective dislocation is a function of the width of needle domain w and spontaneous strain ε_0. From the classical theory of dislocations, the energy

of the dislocation is proportional to b^2 and consequently the needle energy is proportional to w^2. Widely separated fine needles thus represent a lower energy state than a single coarse needle of the same total width, provided the domain wall energy itself is negligible. Barium titanate crystals commonly form arrays of fine needles with a needle width that balances the contributions of domain wall energy and the energy due to the needle tips.

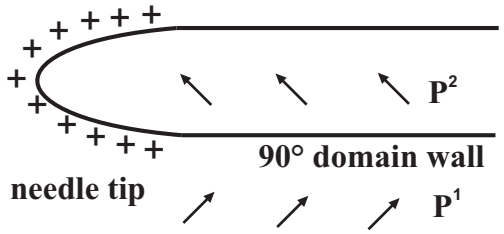


Figure 2.9: Equivalent charge spreading over the needle tip due to the electrical incompatibility

Around a dislocation in a piezoelectric crystal there is generally a region of electric polarization arising from the coupling between elastic strain and polarization [75]. Accordingly, being a source of internal stress, each needle tip is also a local source of electric field [76]. Due to the electric incompatibility, each needle tip is a local source of electric field which can be modelled as the field due to a distribution of equivalent charge which spread over the needle tip, as illustrated in figure 2.9. For a thin, blunt needle, the field may be approximated using a single effective line charge, found from:

$$q = \int (\mathbf{P}^2 - \mathbf{P}^1) \cdot \mathbf{n}_{tip}\, dl \tag{2.10}$$

where, $\mathbf{n}_{tip}$ is the outward normal vector of the domain wall at the needle-tip. The integral in Eq. (2.10) is conducted along the domain wall, around the needle tip. For the 90° a-a needle, the resulting magnitude of effective line charge produced by the electrical incompatibility at the needle domain tip is $\sqrt{2}p_0 w$ per unit depth into the page where p_0 is the spontaneous polarization magnitude. The direction of the Burgers vector and sign of line charge are determined by the relation of the polarization directions between parent domain and needle domain.

According to the above analysis, the absolute value of the equivalent dislocation and line charge only dependent on material constant (ϵ_0 and p_0) and the width of needle domain (w). However, the orientation of needle domain influences the direction of the equivalent dislocation **b** and the sign of the equivalent line charge q. Based on the definition of Burgers vector mentioned in section 2.1.1 and equation 2.10, we give the Burgers vector and line charge for the following needles with different orientations in different quadrant location, as shown in figure 2.10. The polarization direction ($\mathbf{P}^1$) of the parent domain is [0 1 0]. The needles N_1, N_2, N_3, and N_4 are 90° a-a domains. Correspondingly, the polarization directions of four needles are $\mathbf{P}^{N1}$=[-1 0 0], $\mathbf{P}^{N2}$=[1 0 0], $\mathbf{P}^{N3}$=[-1 0 0], and $\mathbf{P}^{N4}$=[1 0 0]. The equivalent Burgers vector and line charge for four needles in different quadrant location are listed in table 2.1:

Table 2.1: The equivalent Burgers vector and line charge for four needles in different quadrant.

Needle	Burgers vector	Line charge
N_1	$\mathbf{b}^1 = 3\sqrt{2}\varepsilon_0 w/2$[1 1 0 0]	$\mathbf{q}^1 = \sqrt{2}p_0 w$[0 0 0 1]
N_2	$\mathbf{b}^2 = 3\sqrt{2}\varepsilon_0 w/2$[1 -1 0 0]	$\mathbf{q}^2 = \sqrt{2}p_0 w$ [0 0 0 1]
N_3	$\mathbf{b}^3 = 3\sqrt{2}\varepsilon_0 w/2$[-1 -1 0 0]	$\mathbf{q}^3 = \sqrt{2}p_0 w$[0 0 0 -1]
N_4	$\mathbf{b}^4 = 3\sqrt{2}\varepsilon_0 w/2$[-1 1 0 0]	$\mathbf{q}^4 = \sqrt{2}p_0 w$[0 0 0 -1]

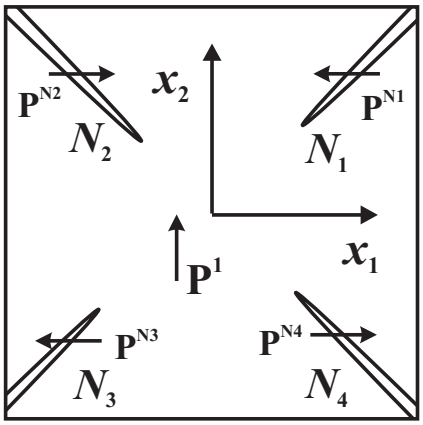


Figure 2.10: Needle domains with different orientations in four quadrant location.

2.4 Fields due to a dislocation with a line charge

In this section, the plane problem of a general dislocation with line charge is discussed for an anisotropic ferroelectric material. Ferroelectric dislocations, as important crystalline defects, influence the electrical, optical, and mechanical properties of ferroelectric materials, and have been studied by many researchers. Merten [77] investigated the electric fields produced by dislocations in piezoelectric media. However, the piezoelectric coupling was ignored, and elastic isotropy was assumed. Later, efforts were made to obtain the coupled electromechanical field of a dislocation with a line charge [78–80]. The following derivation is due to Barnett and Lothe [80] and is summarized here as the results are used in chapter 4.

Following Barnett's theory for anisotropic material, we derive the plane solution to the electromechanical field and energy of an infinite straight dislocation with Burgers vector **b** and an infinite line charge distributed with density q per unit length. The position of line charge coincides with the dislocation core spatially. The constitutive equations for a piezoelectric medium describing the relationship of mechanical stress σ_{ij} and electric displacement D_i with the displacement gradients $u_{k,m}$ and the electric potential gradients $\varphi_{,m}$ are

$$\sigma_{ij} = C_{ijkm}u_{k,m} + e_{mij}\varphi_{,m} \tag{2.11}$$

$$D_i = e_{ikm}u_{k,m} - \kappa_{im}\varphi_{,m} \tag{2.12}$$

where C_{ijkm}, e_{mij}, and κ_{im} are the tensors of elastic, piezoelectric, and dielectric constants, respectively. Additionally, the relation between electric potential φ and electric field E_i is

$$E_i = -\partial\varphi/\partial x_i = -\varphi_{,i} \tag{2.13}$$

The equilibrium equations, in the absence of body forces and free charge are given by

$$\sigma_{ij,i} = 0 \qquad D_{i,i} = 0 \tag{2.14}$$

An arbitrary orthonormal plane basis with unit vectors $\mathbf{m}_0$ and $\mathbf{n}_0$, and orthogonal unit vector $\mathbf{t}_0 = \mathbf{m}_0 \times \mathbf{n}_0$ is defined, so $\mathbf{t}_0$ is along the defect line. This coordinate system ($\mathbf{m}_0$, $\mathbf{n}_0$) is used as the global plane basis, as shown in figure 2.11. Consider first plane strain and electric field conditions, independent of position along $\mathbf{t}_0$ ($u_{k,m}t_m = 0$; $\varphi_{,m}t_m = 0$), Esheby [78] introduced the displacement field in the form

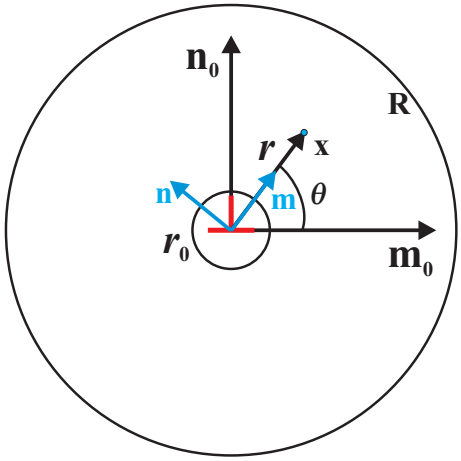


Figure 2.11: The plane coordination system

$$u_i = A_i f(\mathbf{m}_0 \cdot \mathbf{x} + p\mathbf{n}_0 \cdot \mathbf{x}) \qquad (i = 1, 2, 3) \tag{2.15}$$

$$\varphi = A_4 f(\mathbf{m}_0 \cdot \mathbf{x} + p\mathbf{n}_0 \cdot \mathbf{x}) \tag{2.16}$$

where the coefficient p and the vector $\mathbf{A}$ are to be determined. By substitution of Eqs. (2.11, 2.12,2.15, 2.16) into Eq. (2.14), Barnett and Lothe [80] showed that the equilibrium equations produce

$$\left\{(m_0m_0)_{JK} + p[(m_0n_0)_{JK} + (n_0m_0)_{JK}] + p^2(n_0n_0)_{JK}\right\} A_K = 0 \tag{2.17}$$

And hence

$$\det\{(m_0m_0)_{JK} + p[(m_0n_0)_{JK} + (n_0m_0)_{JK}] + p^2(n_0n_0)_{JK}\} = 0 \tag{2.18}$$

The components of the matrices (m_0m_0), (m_0n_0), (n_0m_0), and (n_0n_0) are defined by

$$(ab)_{JK} = a_i E_{iJKm} b_m \tag{2.19}$$

where, a and b any are real three-dimensional vectors. Here lower-case indices run from 1 to 3 while upper-case indices run from 1 to 4. The tensor E_{iJKm} is:

$$\begin{aligned} E_{iJKm} &= C_{ijkm} \quad (J,K = 1,2,3) \\ &= e_{mij} \quad (J = 1,2,3; K = 4) \\ &= e_{ikm} \quad (J = 4; K = 1,2,3) \\ &= -\kappa_{im} \quad (J = K = 4) \end{aligned} \tag{2.20}$$

Component values for barium titanate were given in table 1.1.

It is possible to recast Eq. (2.17) into an eight-dimensional eigenvalue problem given by

$$\mathbf{N}\xi = p\xi \tag{2.21}$$

$$\xi = \left\{ \begin{array}{c} \mathbf{A} \\ \mathbf{L} \end{array} \right\} \tag{2.22}$$

where

$$\mathbf{L} = -\{(n_0m_0) + p(n_0n_0)\}\mathbf{A} = \frac{1}{p}\{(m_0m_0) + p(m_0n_0)\}\mathbf{A} \tag{2.23}$$

$$\mathbf{N} = -\left[\begin{array}{cc} \tilde{\mathbf{S}} & \tilde{\mathbf{Q}} \\ \tilde{\mathbf{B}} & \tilde{\mathbf{S}}^{\mathbf{T}} \end{array} \right] \tag{2.24}$$

In Eq. 2.24 the matrices $\tilde{\mathbf{Q}}$, $\tilde{\mathbf{S}}$, $\tilde{\mathbf{B}}$ are given by

$$\tilde{\mathbf{Q}} = (n_0 n_0)^{-1} \tag{2.25}$$

$$\tilde{\mathbf{S}} = (n_0 n_0)^{-1}(n_0 m_0) \tag{2.26}$$

$$\tilde{\mathbf{B}} = (m_0 m_0)(n_0 n_0)^{-1}(n_0 m_0) - (m_0 m_0) \tag{2.27}$$

The eigenvalues p_α ($\alpha = 1, 2 \ldots 8$) are solutions of the determinant relation Eq. (2.18). Following Barnett's work [80], the normalised eigenvectors are defined by $2A_\alpha \cdot L_\alpha = 1$. The displacement field and the strain field around the dislocation and line charge are then given by

$$u_I = \frac{1}{2\pi i} \sum_{\alpha=1}^{8} \{\pm A_{I\alpha} L_{S\alpha} b_S \pm A_{I\alpha} A_{S\alpha} q_S\} \ln(\mathbf{m}_0 \cdot \mathbf{x} + p_\alpha \mathbf{n}_0 \cdot \mathbf{x}) \tag{2.28}$$

$$u_{I,m} = \frac{1}{2\pi i} \sum_{\alpha=1}^{8} \{\pm A_{I\alpha} L_{S\alpha} b_S \pm A_{I\alpha} A_{S\alpha} q_S\} \frac{(m_0)_m + p_\alpha (n_0)_m}{(\mathbf{m}_0 \cdot \mathbf{x} + p_\alpha \mathbf{n}_0 \cdot \mathbf{x})} \tag{2.29}$$

where the positive sign has to be used for $\alpha = (1, 2, \ldots 4)$ and the negative sign for $\alpha = (5, 6, \ldots 8)$. As before, upper case indices run from 1 to 4. The extended vector **u** expresses the generalized displacement $[u_1;\ u_2;\ u_3;\ \varphi]$. The Burgers vector **b** is also generalized as displacement and electric potential jump, $\mathbf{b} = [b_1,\ b_2,\ b_3,\ \triangle\varphi]^T$; For present purposes, the electric potential jump $\triangle\varphi$ is zero. The magnitude and direction of a dislocation is determined by vector $(b_1\ b_2\ b_3)$. Additionally, the extended line charge vector $\mathbf{q} = [q_1,\ q_2,\ q_3,\ q_4]^T$ is generalized from a line force. The first three components $(q_1\ q_2\ q_3)$ represent an effective line force vector, which for present purposes is zero. The final component q_4 is the line charge density, which is non-zero in the present application.

To further simplify the expression for the strain field, Barnett and Lothe introduce cylindrical coordinates $(r,\ \theta)$ as shown in figure 2.11, and an 'integral formalism', since $A_{I\alpha}$ and $L_{I\alpha}$ are independent of the plane basis. The radius r is the distance between the dislocation core and the point x in the field. The azimuth angle θ is defined by the rotation of the global plane

basis vectors $\mathbf{m}_0$ and $\mathbf{n}_0$ around the dislocation core into the plane basis vectors $\mathbf{m}$ and $\mathbf{n}$ in a right-handed sense, see figure 2.11. Therefore the plane basis vectors $\mathbf{m}$ and $\mathbf{n}$ fulfil $\mathbf{m}\cdot\mathbf{x} = r$ and $\mathbf{n}\cdot\mathbf{x} = 0$. Hence,

$$r = \sqrt{(\mathbf{m}_0\cdot\mathbf{x})^2 + (\mathbf{n}_0\cdot\mathbf{x})^2} \tag{2.30}$$

$$\tan(\theta) = \frac{\mathbf{n}_0\cdot\mathbf{x}}{\mathbf{m}_0\cdot\mathbf{x}} \tag{2.31}$$

$$\mathbf{m} = \cos(\theta)\mathbf{m}_0 + \sin(\theta)\mathbf{n}_0 \tag{2.32}$$

$$\mathbf{n} = -\sin(\theta)\mathbf{m}_0 + \cos(\theta)\mathbf{n}_0 \tag{2.33}$$

Therefore, based on Eqs. (2.32, 2.33), the matrices (mm), (mn), (nm) and (nn) depend on the azimuth angle θ in current plane basis ($\mathbf{m}$, $\mathbf{n}$). The related matrices $\tilde{Q}$, $\tilde{S}$, and $\tilde{B}$ are computed by integrating over θ, yielding 4×4 matrices Q, S, and B given by

$$Q_{KS} = Q_{SK} = -\frac{1}{2\pi}\int_0^{2\pi} (nn)^{-1}_{SK}\, d\theta \tag{2.34}$$

$$S_{KS} = -\frac{1}{2\pi}\int_0^{2\pi} (nn)^{-1}_{KJ}(nm)_{JS}\, d\theta \tag{2.35}$$

$$B_{KS} = B_{SK} = \frac{1}{8\pi^2}\int_0^{2\pi} \left\{(mm)_{KS} - (mn)_{KJ}(nn)^{-1}_{SK}(nm)_{RS}\right\} d\theta \tag{2.36}$$

Equations (2.28) and (2.29) can then be written as

$$u_I = -\frac{1}{2\pi}(S_{IS}b_S + Q_{IS}q_S)\ln|\mathbf{x}| \tag{2.37}$$

$$\begin{aligned} u_{I,m} \;=\; & (2\pi\,|\mathbf{x}|)^{-1}\left\{-m_m(S_{IS}b_S + Q_{IS}q_S) + n_m(nn)^{-1}_{IJ}\right. \\ & \left.[(4\pi B_{JS} + (nm)_{JK}S_{KS})b_S + (S_{SJ} + (nm)_{JK}Q_{KS})q_S]\right\} \end{aligned} \tag{2.38}$$

The total energy U of the dislocated ferroelectric with a line charge is calculated from

summation of the strain energy and the electrical energy:

$$U = \frac{1}{2}\int_{\nu} \{\sigma_{ij}u_{i,j} + D_i E_i\}\ d\nu \tag{2.39}$$

For a cylindrical domain of inner and outer radius r_0 and R, the total energy, integrated using Gauss' theorem U is provided by [80]

$$U = \frac{1}{4\pi}\left(4\pi b_J B_{JS} b_S + 2q_J S_{JS} b_S + q_J Q_{JS} q_S\right) \ln\left(\frac{R}{r_0}\right) \tag{2.40}$$

Note that the derivation of the field and energy of a line charge and dislocation follows that of Barnett and Lothe [80] exactly. However, these results do not appear to have been applied to understanding needle domains before. These results are used to compute strains and electric fields near needle domains in chapter 4.

2.5 Modified Peach-Koehler force

As we mentioned in section 2.1.2, the Peach-Koehler force is defined to describe the mechanical force experienced by interacting dislocations. However, we need a modified Peach-Koehler force to quantify the interactive effect of needle domains, due to the fact that the tips of needle domains are modelled as an effective edge dislocation coupled with a line charge. This means the modified Peach-Koehler force comprises two parts: 1) mechanical force, 2) electrical force. The modified Peach-Koehler force between two needles N_i and N_j is given as follows:

$$\mathbf{F}_{i\to j} = \left(\mathbf{b}^j \cdot \boldsymbol{\sigma}^i\right) \times \mathbf{k} + q^j \mathbf{E}^i \tag{2.41}$$

where, $\mathbf{F}_{i\to j}$ represents the force acting on N_j due to N_i. The needle domain N_j is modelled as an edge dislocation $\mathbf{b}^j$ coupled with a line charge q^j. Accordingly, the stress $\boldsymbol{\sigma}^i$ and electric $\mathbf{E}^i$

fields are produced by needle domain N_i. Based on the formulation of Lubarda $et\ al.$ [81], the existence of each needle domain produces stresses and electric fields that can be superposed. Therefore, we may sum contributions of the form of Eq. 2.41 due to several interacting needles.

Typically, motion of needle domains responding to external loads is by extension or retraction along the longitude direction, without sideways motion. Accordingly, it is reasonable to consider the extension force F_e resolved along the longitudinal direction of a given needle.

$$F_e = \mathbf{F} \cdot \mathbf{n}_{tip} \tag{2.42}$$

where, $\mathbf{n}_{tip}$ is the unit vector in the extension direction. A positive extension force acts to lengthen the needle domain, and vice versa.

An alternative method to calculate the interaction force is through considering energy. The equilibrium state of the interacting needle domains corresponds to a minimum potential energy configuration. Based on the superposition of stress and electric fields produced by interactive needle domains, the total internal energy U can be calculated by Eq. 2.39. Accordingly, the interactive force $\mathbf{F}$ acting on a given needle domain is equal to minus the energy gradient with respect to position of the needle domain.

$$\mathbf{F} = -\frac{\partial U}{\partial \mathbf{x}} \tag{2.43}$$

The extension force F_e can then be calculated from Eq. 2.42.

Considering the process of computation, the calculation of interaction force by using Eq. 2.41 has the advantages in both precision and computing time. The reason is that we only need directly calculate the value of stress and electric field at the location of the needle tip of interest. If Eq. 2.43 is utilized, the energy must be found by integrating over the entire region being modelled. When the needle under consideration moves to a new position, the energy calculation must be updated. This process is likely to be time consuming. Additionally, the selected range

for superposition in the simulation must be finite and must avoid the singular core; these limits will influence the precision of computation. Also, the calculation of gradient operation for obtaining the interactive force results in reducing the precision during the simulation process.

2.6 Relationship between plane strain and plane stress

Barnett's solution provides a plane strain and plane electric field solution. However, a common configuration of crystal is a crystal plate which is extended in the x_1 and x_2 directions, but thin in the x_3 direction. Such plates have a free surface normal to x_3 and due to insulating properties this surface is largely free of charge. Consequently, plane stress and plane electric displacement become appropriate model approximations. In this section, relationships are derived to transform between plane strain-plane electric field conditions and plane stress-plane electric displacement.

For convenience, the constitutive equations modified from Eqs. 2.11 and 2.12, which describe the relationship of mechanical stress $\boldsymbol{\sigma}$ and electric displacement $\mathbf{D}$ with the strain $\boldsymbol{\epsilon}$ and the electric field $\mathbf{E}$, are given in matrix form by:

$$\begin{bmatrix} \boldsymbol{\sigma} \\ \mathbf{D} \end{bmatrix} = \begin{bmatrix} \mathbf{C} & -\mathbf{e} \\ \mathbf{e} & \boldsymbol{\kappa} \end{bmatrix} \begin{bmatrix} \boldsymbol{\epsilon} \\ \mathbf{E} \end{bmatrix} \tag{2.44}$$

where, $\mathbf{C}$, $\mathbf{e}$, and $\boldsymbol{\kappa}$ are tensors of the elastic, piezoelectric, and dielectric properties, respectively. The corresponding inverse of Eq. 2.44 is as follows,

$$\begin{bmatrix} \boldsymbol{\epsilon} \\ \mathbf{E} \end{bmatrix} = \begin{bmatrix} \mathbf{S}^{\mathbf{D}} & \mathbf{g} \\ -\mathbf{g} & \boldsymbol{\beta}^{\boldsymbol{\sigma}} \end{bmatrix} \begin{bmatrix} \boldsymbol{\sigma} \\ \mathbf{D} \end{bmatrix} \tag{2.45}$$

where, $\mathbf{S}^{\mathbf{D}}$ is the elastic compliance matrix under constant electric displacement, and $\boldsymbol{\beta}^{\boldsymbol{\sigma}}$ is equivalent to the inverse of the electrical permittivity under constant stress. Additionally, the

piezoelectric constant g is defined by:

$$\mathrm{g}_{ij} = \frac{\partial \varepsilon_j}{\partial D_i} = -\frac{\partial E_i}{\partial \sigma_j} \tag{2.46}$$

The solution of a problem under either the plane strain or plane stress assumption satisfies both the constitutive equations 2.44 and 2.45. Besides satisfying the constitutive equation, solutions for plane stress or plane strain satisfy the equilibrium equations Eq. 2.14.

In plane stress and plane electric displacement, all stress and electric displacement components perpendicular to the plane $x_1 - x_2$ are assumed to be zero, the only nonzero components being $\sigma_{11},\ \sigma_{12},\ \sigma_{22}$, and $D_1,\ D_2$. Therefore, Eq. 2.45 is reduced to:

$$\begin{bmatrix} \varepsilon_{11} \\ \varepsilon_{22} \\ 2\varepsilon_{12} \\ E_1 \\ E_2 \end{bmatrix} = \begin{bmatrix} S_{11}^D & S_{12}^D & S_{16}^D & \mathrm{g}_{11} & \mathrm{g}_{12} \\ S_{21}^D & S_{22}^D & S_{26}^D & \mathrm{g}_{21} & \mathrm{g}_{22} \\ S_{61}^D & S_{62}^D & S_{66}^D & \mathrm{g}_{61} & \mathrm{g}_{62} \\ -\mathrm{g}_{11} & -\mathrm{g}_{12} & -\mathrm{g}_{16} & \beta_{11}^\sigma & \beta_{12}^\sigma \\ -\mathrm{g}_{21} & -\mathrm{g}_{22} & -\mathrm{g}_{26} & \beta_{12}^\sigma & \beta_{22}^\sigma \end{bmatrix} \begin{bmatrix} \sigma_{11} \\ \sigma_{22} \\ \sigma_{12} \\ D_1 \\ D_2 \end{bmatrix} \tag{2.47}$$

The corresponding inverse of Eq. 2.47 is given by:

$$\begin{bmatrix} \sigma_{11} \\ \sigma_{22} \\ \sigma_{12} \\ D_1 \\ D_2 \end{bmatrix} = \begin{bmatrix} C_{11}^* & C_{12}^* & C_{16}^* & -e_{11}^* & -e_{12}^* \\ C_{21}^* & C_{22}^* & C_{26}^* & -e_{21}^* & -e_{22}^* \\ C_{61}^* & C_{62}^* & C_{66}^* & -e_{61}^* & -e_{62}^* \\ e_{11}^* & e_{12}^* & e_{16}^* & \kappa_{11}^* & \kappa_{12}^* \\ e_{21}^* & e_{22}^* & e_{26}^* & \kappa_{12}^* & \kappa_{22}^* \end{bmatrix} \begin{bmatrix} \varepsilon_{11} \\ \varepsilon_{22} \\ 2\varepsilon_{12} \\ E_1 \\ E_2 \end{bmatrix} \tag{2.48}$$

Eq. 2.48 for plane stress and Eq. 2.44 for plane strain have the same formulations, the only difference being in the coefficients relating the stress (or electric displacement) and strain (or electric field) components. From a mathematical perspective, the plane stress solution simply looks like the plane strain solution for a material with different material constants. The new

elastic constant C^*, piezoelectric constant e^*, and dielectric constant κ^* for plane stress problems are computed by inverting of Eq. 2.47.

The in-plane strain components ε_{11}, ε_{12}, ε_{22}, and electric field components E_1 and E_2 in Eq. 2.48 can now be calculated by Eq. 2.28. After that, we can use equation 2.48 to compute the plane stress plane electric displacement solution, stresses $\sigma_{11},\ \sigma_{12},\ \sigma_{22}$, and electric displacement D_1, D_2. To further calculate the normal components of strain ε_{13}, ε_{23}, ε_{33}, and electric fields E_3, the stress components $\sigma_{11},\ \sigma_{12},\ \sigma_{22}$, and electric displacement D_1, D_2 computed from Eq. 2.48 under plane stress, as well as $\sigma_{13} = \sigma_{23} = \sigma_{33} = 0$ and $D_3 = 0$, are substituted into the expanded form of equation 2.45 as follows,

$$\begin{bmatrix} \varepsilon_{11} \\ \varepsilon_{22} \\ \varepsilon_{33} \\ 2\varepsilon_{23} \\ 2\varepsilon_{31} \\ 2\varepsilon_{12} \\ E_1 \\ E_2 \\ E_3 \end{bmatrix} = \begin{bmatrix} S^D_{11} & S^D_{12} & S^D_{13} & S^D_{14} & S^D_{15} & S^D_{16} & \mathrm{g}_{11} & \mathrm{g}_{12} & \mathrm{g}_{13} \\ S^D_{21} & S^D_{22} & S^D_{23} & S^D_{24} & S^D_{25} & S^D_{26} & \mathrm{g}_{21} & \mathrm{g}_{22} & \mathrm{g}_{23} \\ S^D_{31} & S^D_{32} & S^D_{33} & S^D_{34} & S^D_{35} & S^D_{36} & \mathrm{g}_{31} & \mathrm{g}_{32} & \mathrm{g}_{33} \\ S^D_{41} & S^D_{42} & S^D_{43} & S^D_{44} & S^D_{45} & S^D_{46} & \mathrm{g}_{41} & \mathrm{g}_{42} & \mathrm{g}_{43} \\ S^D_{51} & S^D_{52} & S^D_{53} & S^D_{54} & S^D_{55} & S^D_{56} & \mathrm{g}_{51} & \mathrm{g}_{52} & \mathrm{g}_{53} \\ S^D_{61} & S^D_{62} & S^D_{63} & S^D_{64} & S^D_{65} & S^D_{66} & \mathrm{g}_{61} & \mathrm{g}_{62} & \mathrm{g}_{63} \\ -\mathrm{g}_{11} & -\mathrm{g}_{12} & -\mathrm{g}_{13} & -\mathrm{g}_{14} & -\mathrm{g}_{15} & -\mathrm{g}_{16} & \beta^\sigma_{11} & \beta^\sigma_{12} & \beta^\sigma_{13} \\ -\mathrm{g}_{21} & -\mathrm{g}_{22} & -\mathrm{g}_{23} & -\mathrm{g}_{24} & -\mathrm{g}_{25} & -\mathrm{g}_{26} & \beta^\sigma_{21} & \beta^\sigma_{22} & \beta^\sigma_{23} \\ -\mathrm{g}_{31} & -\mathrm{g}_{32} & -\mathrm{g}_{33} & -\mathrm{g}_{34} & -\mathrm{g}_{35} & -\mathrm{g}_{36} & \beta^\sigma_{31} & \beta^\sigma_{32} & \beta^\sigma_{33} \end{bmatrix} \begin{bmatrix} \sigma_{11} \\ \sigma_{22} \\ \sigma_{33} \\ \sigma_{23} \\ \sigma_{31} \\ \sigma_{12} \\ D_1 \\ D_2 \\ D_3 \end{bmatrix} \tag{2.49}$$

Through the above computation, we can construct the full solution of a plane stress and plane electric displacement problem which satisfies equilibrium and the constitutive equation.

3

Chapter 3 Observation of needle domains

From the previous chapters, it was discussed that needle domains are a commonly occurring microstructure in ferroelectrics. The existence of needle domains gives rise to high stress field and electrical field around needle tips in ferroelectrics. In Chapter 2, considering the mechanical and electrical incompatibility, the needles were modelled as defects producing fields similar to a dislocation and a line charge. This model is based on a 'blunt' needle which is a needle with the same width right up to its tip. It is desirable to explore further the shape, the fields produced, and the patterns in which needle domains are found. To do these, the present chapter uses optical microscopy and X-ray observations of needle domains in $BaTiO_3$ single crystals.

3.1 Optical microscopy

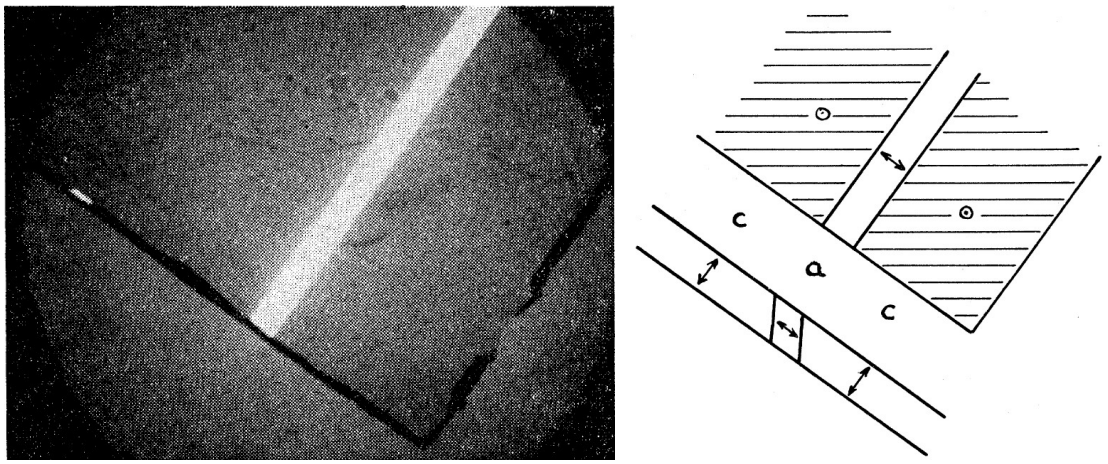
$BaTiO_3$ single crystals are commonly selected to study the microstructure of ferroelectrics because of stable physical properties, simple crystalline structure, availability of suitable size crystals for experiment, and convenience of domain visualisation and measurement. $BaTiO_3$ single crystal is transparent but the domains are optically anisotropic. Because of this, light is reflected at domain walls, so the domains can be easily observed using optical microscopy. Optical methods to visualize domains have a significant advantage of being non-destructive, and

allowing real-time observation of the domain evolution under the electrical, mechanical and thermal loading.

3.1.1 Optical techniques

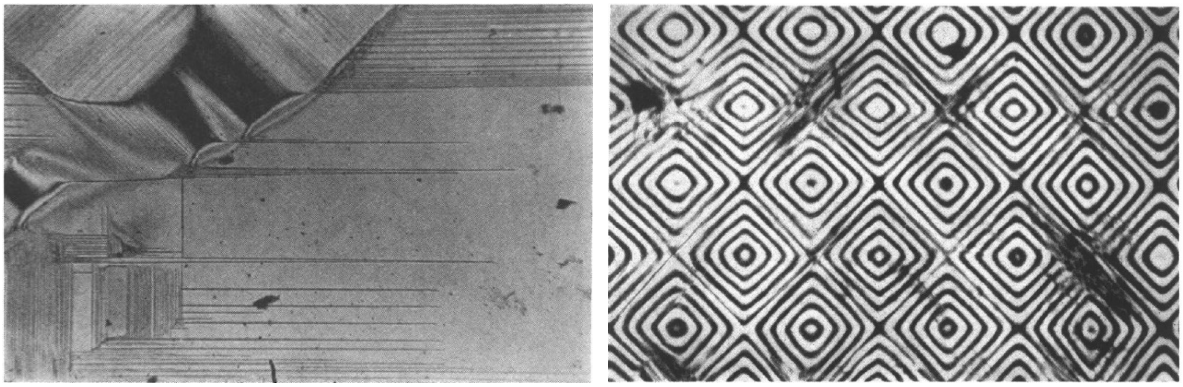
Optical microscopy can utilize the birefringence of $BaTiO_3$ to make domains visible. Birefringence is the optically anisotropic property of crystals having a refractive index that depends on the polarization and propagation direction of light. The domain wall is an interface between two domains with different polarizations. When the light goes through the crystal, birefringence causes orthogonal components of the wave to propagate at different speeds. This difference in refractive index causes a phase shift of the light, equivalent to a rotation of the optical polarization. Since different domains have differently oriented optical axes, the domains can be observed. Accordingly, the domains with different electrical polarization can be distinguished under optical microscopy.

Much effort has gone into investigating the domains and domain evolution in ferroelectrics. Early on, optical microscopy was used by Merz (1954) to investigate dynamic domain evolution in ferroelectric $BaTiO_3$ single crystals. Through microscopy between crossed polarizing filters, a domains (bright) and c domains (dark) can be easily distinguished, see figure 3.1. Forsbergh conducted a systematic study of the domain patterns that are formed due to twinning in $BaTiO_3$ single crystal. Wedge shaped laminar domains and a square-net pattern of domains were observed under crossed polarizers, as shown in figures 3.2. Many studies adopt optical microscopy to observe the domain microstructure in ferroelectrics followed. Salje $et\ al.$ [48] experimentally viewed needle twins in $LaAlO_3$ single crystal. During the experiment, the method of optical microscopy has the advantage of real-time in-situ observation with a large view range to conveniently investigate the change in pattern of microstructure under loads [82].



(a) (b)

Figure 3.1: Optical observation and sketch of a 90° domain wall between an a domain and two c domains in $BaTiO_3$ single crystal [43].



(a) (b)

Figure 3.2: Observation of wedge-shaped laminar domains and square-net domain pattern in $BaTiO_3$ single crystal [12].

3.1.2 Generation and configuration of needle domains

In section 1.5.1, we have introduced methods for the generation of needle domains in $BaTiO_3$ single crystal: (1) When the $BaTiO_3$ crystals cool through Curie temperature, the needle domains are generated and distributed in the crystal; (2) Loading such as three-point bending also generates needle domains at the sample edge. Here, we try to generate the needle domains through changing temperature and further study the evolution of needle domains under thermal loading.

Commercially sourced $BaTiO_3$ single crystals supplied by Marketech International Inc. are investigated using Alicona's InfiniteFocus optical microscope. The size of the specimens was $10 \times 10 \times 0.5$ mm, and they were supplied with both 10×10 mm surfaces polished. The specimen is cut with tetragonal [1 0 0], [0 1 0], and [0 0 1] axes parallel to the specimen edges. A Deben^{TM} heating $\&$ cooling stage with the precision of $0.1°$C is utilized to control the temperature of crystals during observation by optical microscopy.

In the experiment, the specimen of $BaTiO_3$ single crystal was first heated above the Curie temperature ($T_c = 120°$C) with $1°\text{C}/5$ min rate to clear up the disordered microstructure caused by the manufacturing process. Then the specimen was cooled back to room temperature with the same rate of temperature change, $1°\text{C}/5$ min. Needle domains formed when the temperature decreased through the Curie temperature. Figure 3.3 presents the detailed configuration of needle domains observed by optical microscope. The domains are slender with a sharp tip. There are two types of needle domains: one grows from the sample edge, and only one tip terminates within the crystal, marked as 'Type-A' in figure 3.3. Another type marked as 'Type-B', has two tips located at both ends within the crystal.

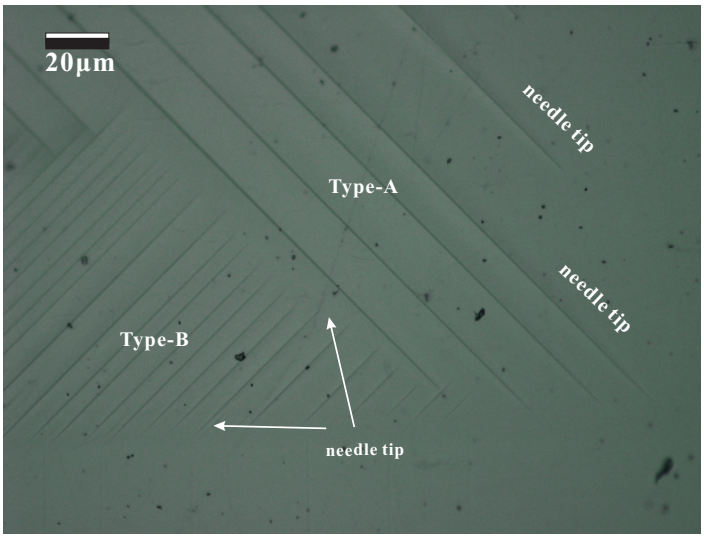
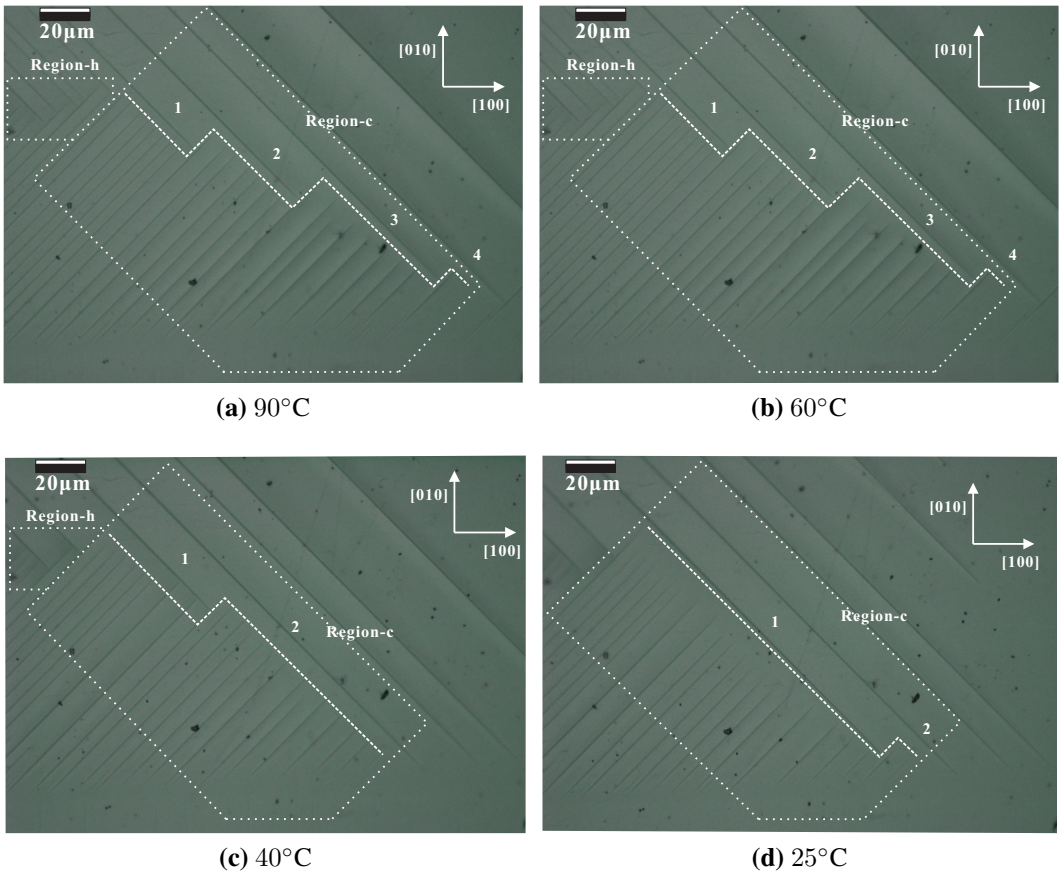


Figure 3.3: Observation of needle domain in $BaTiO_3$ single crystal under optical microscopy.

As cooling continues down from Curie temperature to room temperature ($25°$C), a series



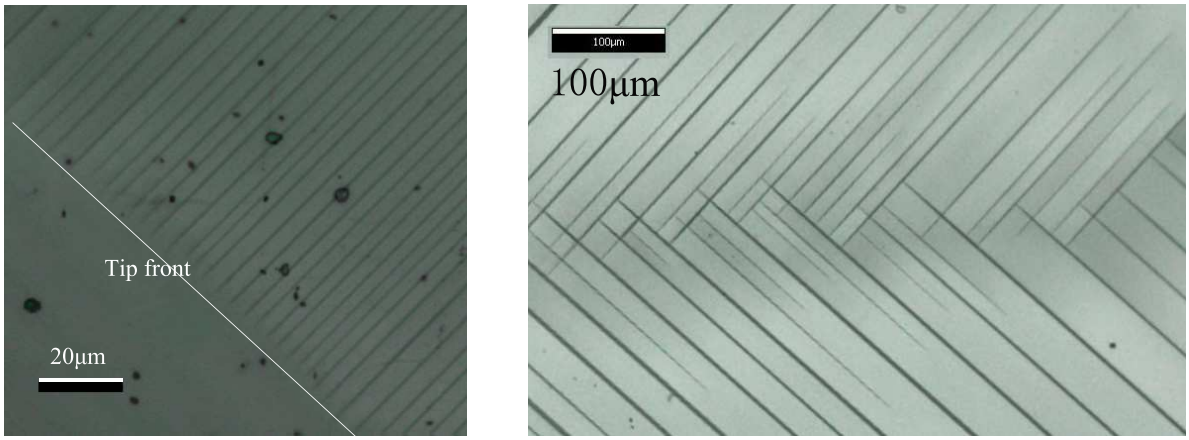
(a) 90°C **(b)** 60°C

(c) 40°C **(d)** 25°C

Figure 3.4: Variation of needle pattern with the changing temperature from 90°C to 25°C.

of changes in pattern happened to the needle domains, as given in figure 3.4. Figure 3.4a shows the groups of needle domains at the temperature 90°C. In region-c, a group of comb-like needle domains along the direction [1 1 0] is formed by the needles with two tips at both ends and the same spacing. The tips at one end align with a horizontal line oriented at 45° to the longitude direction of the needle domains, while the tips at another end stagger, following perpendicular needle domains along the direction [1 -1 0]. The junction between the two groups of needle domains, marked in figure 3.4a, presents a ladder shape with four steps. Additionally, we also find that there is another staggered pattern of needle domains composed of [1 -1 0] needles and perpendicular [1 1 0] needles shown in region-h. These staggered and perpendicular patterns of needle domains are common in $BaTiO_3$ crystals. When the temperature cools down to 60°C, there is no change to the needle pattern.

However, as the temperature drops to $40°C$, we find the staggered pattern of needles in region-c starts to change, as given in figure 3.4c. The tips at the staggered end for [1 1 0] needle domains including the third and fourth steps retreat and some needles disappear. Correspondingly, the perpendicular needle domains with the direction [1 -1 0] extend. The above change causes the stepped interface to flatten and align with the [1 -1 0] direction as the temperature reaches $25°C$. In region-h, Some needles are just visible, but they disappear as the temperature is reduced. In practice, the disappearing needles simply retreated to the boundary. The perpendicular needles with [1 1 0] have no change basically.



(a) **(b)**

Figure 3.5: Patterns of needle domain (a) Comb-like needle domain (b) Herringbone type array of needle domains

In Chapter 2, it was shown that a needle domain will influence the stress and electric fields around its tip and cause the increase of internal energy. To reduce energy, groups of needle domains usually arrange in certain patterns. We found two typical patterns, herringbone (or 'chevron') and comb-like needle domains. Figures 3.4d and 3.5a show comb-like needle domains which compose of similar needle domains with approximately the same spacing. Their tips lie in a line roughly perpendicular to the longitudinal direction of the domains. This suggests that their interactive force positions each needle domain tip in the tip front in the absence of external disturbance. The stability of this needle pattern will be further studied and interpreted

in Chapter 4. Another needle pattern, herringbone needle pattern, is formed by perpendicular domain needles in a staggered pattern, somewhat similar to the observation shown in figures 3.5a and 3.5b. We can hypothesize that the tips are also held in position by interactive forces. The interaction among the needle tips will be also analysed in Chapter 4.

3.2 X-ray observation methods

X-ray diffraction is often used to determine the arrangement of atomic structure within a crystal, based on the angles and intensities of the diffracted beams. The X-ray topographic method is a powerful tool for investigating lattice imperfections and observing domain structures in ferroelectric materials. Compared with optical microscopy, it has advantages of clearly distinguishing and identifying domain types, a^1, a^2 and c domains, and it has ability to measure strains and identify crystal structure and phase transformations. Besides, X-ray technology permits nondestructive studies and facilitates analysis on the evolution of domains in ferroelectrics. Additionally, X-rays easily pass through materials, showing the internal structure.

X-ray diffraction has been used by many researchers in the investigation of domain structures in ferroelectric crystals [83–86]. Niizeki and Hasegawa made use of X-ray diffraction to identify domain types to study antiparallel domains in $BaTiO_3$ single crystals [83]. Park, Kim $et\ al.$ [84, 85, 87] carried out a study of domains and strain fields of $BaTiO_3$ single crystals using white beam X-ray; their experimental results demonstrate the advantage of X-ray versus optical microscopy, see figure 3.6. The image obtained from X-ray has quantitative high-resolution, which is key to understanding local behaviour in ferroelectric materials at micrometer or nanometre length scales. Fogarty $et\ al.$ [88] also observed antiparallel ferroelectric 180° domains using high-resolution X-ray diffraction imaging in barium titanate and strontium barium niobate. This technique permits determining the shape and location of domains, with spatial resolution of $1\ \mu$m or better. The domains are visible in both Laue and Bragg geometry

(reflection topography). They found that the surface domain structure of barium titanate differs significantly from that of interior. In the conventional methods, the strain does not provide direct information on domain nucleation and growth. However, X-ray can be used to study the evolution of domains throughout the polarization reversal process. Nittala $et\ al.$ [89] utilized X-rays to measure thin film microstructural and crystallographic evolution during heating.

X-ray diffraction is also recommended to measure the strain at the very local scale in materials which are not homogeneous [90]. This method is direct, non-destructive and is applicable to all crystalline materials. Though optical birefringence can offer the strain measurement around domain, this measurement is indirect, requiring one to assume bulk piezoelectric and electrio-optic coefficients in the wall region. Additionally, comparing with the measurement of optical birefringence, the X-ray images are more sensitive to small strains. Nakashima $et\ al.$ [89] investigated an electric-field-induced strain in $BiFeO_3$ thin film using time-resoved X-ray direction.

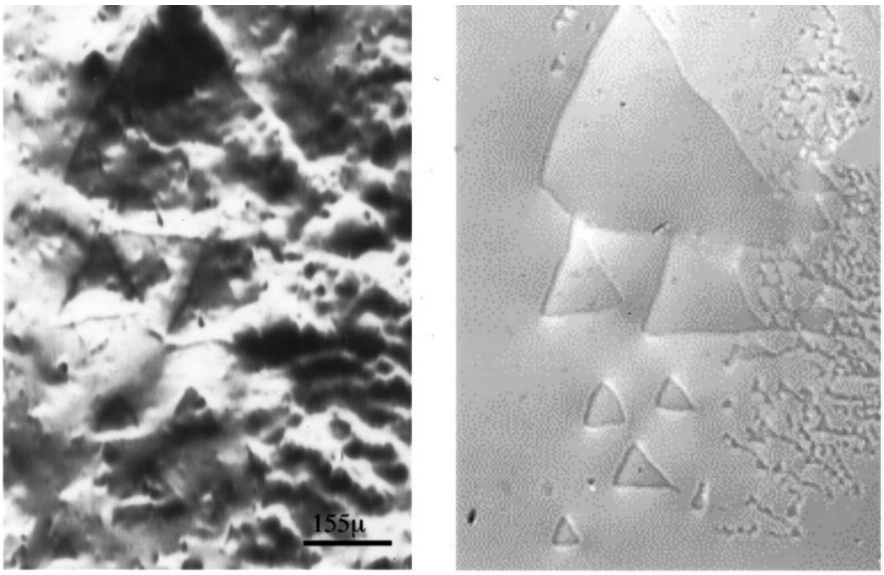


Figure 3.6: Comparison of microstructure for antiparallel $180°$ domains in $LiTaO_3$ crystals imaged by X-ray and Optical microscopy (a) X-ray Bragg-diffraction image, (b) the same area imaged by optical microscopy [84].

The basis of all X-ray diffraction measurements is described in Bragg's Law proposed by W.H. Bragg and W.L. Bragg in 1913. The periodic planes of atoms in a crystalline material

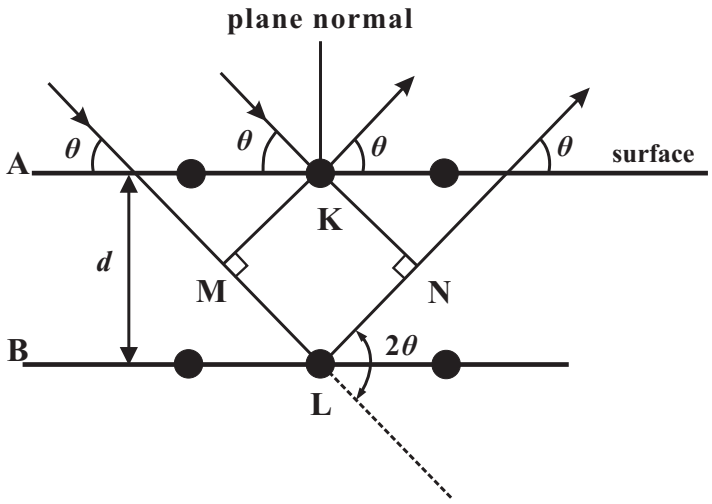


Figure 3.7: Diffraction of X-rays by a crystal lattice.

can cause constructive (destructive) interference patterns by diffraction. As illustrated in figure 3.7, constructive interference happens when the path-length difference ($ML + LN$) between the reflection by two different atom layers (A and B atom planes) is equal to an integer multiple of the wavelength λ, namely,

$$2d \sin\theta = n\lambda \tag{3.1}$$

where d is the spacing between diffracting atom layers, θ is the angle of incident X-ray beam relative to reflection plane, n is any positive integer (it determines the order of reflection), and λ is the wavelength of the X-ray beam. In honour of the discoverers of this equation, the position at the peak of diffraction intensity has been named the Bragg angle θ and the interference peak is termed the Bragg reflection.

Figure 3.8 shows the scattering of X-rays by a crystal of $BaTiO_3$ with tetragonal structure. In figure 3.8a, surface-ABCD is the reflection surface of a square material with c-axis normal to the surface. The X-ray beam is reflected by the specimen and collected by detector. To conveniently understand the working theory of X-ray, the diffractometer angles used in distinguishing domain and measuring strain in crystals are listed as follows. These angles are also illustrated in figure 3.8b.

- 2-theta (2θ)

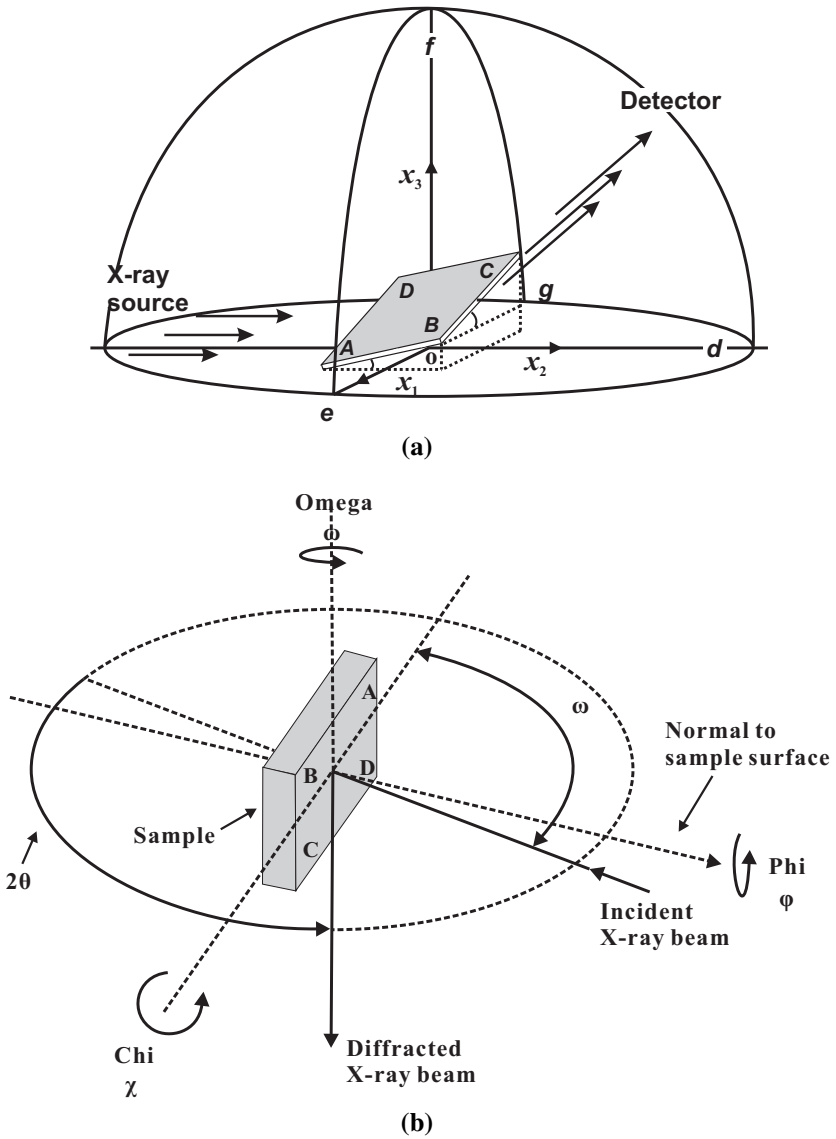


Figure 3.8: (a) Scattering of X-ray by a specimen (b) The diffraction angles used in X-ray analysis (edited from [90]).

θ is the Bragg angle, while 2θ is the diffracted angle between the transmitted incident and diffracted X-ray beams.

- Omega (ω)

  The angle between the incident X-ray beam and the sample surface. Both ω and 2θ lie in the same plane.

- Phi (ϕ)

The angle of rotation of the sample about its surface normal.

- Chi (χ)

  Chi rotates in the plane normal to the plane containing omega ω and 2θ

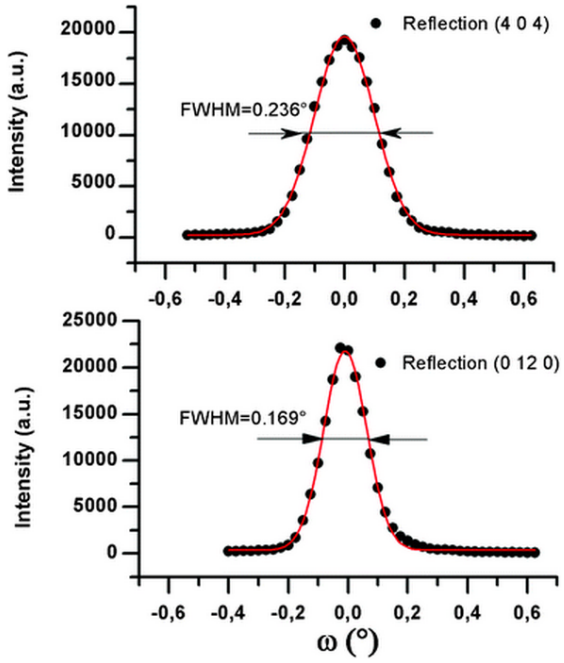


Figure 3.9: Rocking curve of the [4 0 4] and [0 12 0] Bragg reflections of $CaFeO_{2.5}$ single crystal [91].

Types of Scan:

- Rocking Curve

  In an X-ray diffraction experiment, the rocking curves method is a useful way to study the microstructures of single crystals. It is primarily used to study defects such as dislocation density and misorientation in crystalline material. The rocking curve is a plot of X-ray intensity vs. Omega (ω), as shown in figure 3.9. By fixing the detector and X-ray source, the sample is rocked to measure the diffracted intensity. The rocking curve peak position is determined by the Bragg angle and the tilt of the planes. Differences in the Bragg angle which corresponds to the differences in the d-spacing of the crystallographic planes result in the differences in the rocking curve peak position. The rocking curve width and

shape is a product of the material and defects. The rocking curve of a perfect crystal has a sharp peak and an intrinsic width (FWHM) for that material. Different planes of a crystal also have different intrinsic peak widths. Additionally, defects cause the rocking curve to broaden beyond the intrinsic width for the Bragg peak. It is possible to measure strain in crystals through observing diffraction peak broadening or peak shifting.

3.2.1 Distinguishing domain types using X-ray diffraction

Imaging techniques of X-ray diffraction can be used to distinguish the domain types (a^1, a^2 and c domains) of $BaTiO_3$ single crystals through adjusting the angular relationship between incident beam and the specimen. The parallel incoming X-ray is diffracted by the specimen. Using monochromatic (fixed wavelength) light, we can then adjust the azimuth of specimen (ω, χ) to put atomic planes with different d-spacing into the Bragg condition. The different d spacings distinguish the different domain types (a^1, a^2 and c). Figure 3.10a, 3.10b, and 3.10c show the sectional lattice structures of in the plane normal to the incident X-ray beam for different domain configurations of $BaTiO_3$ with tetragonal phase (refer to figure 3.8). The horizontal lines in these figures show the diffraction atom layers. Take the a^1 domain for example, we calculate the spacing between diffracting atom layers d, see figure 3.10a. According to geometry of figure 3.10a, we can get d_1 and χ_1:

$$d_1 = \frac{ac}{\sqrt{a^2 + (2c)^2}} \tag{3.2}$$

$$\chi_1' = \tan^{-1}(\frac{a}{2c}) \tag{3.3}$$

where, a and c are the lattice parameters of $BaTiO_3$ single crystal in tetragonal phase, $a = 3.985$ Åand $c = 4.029$ Å. Based on Bragg's law Eq. 3.1, the incident angle θ is obtained:

$$\theta_1 = \sin^{-1}(\frac{n\lambda}{2d_1}) \tag{3.4}$$

Table 3.1: The diffraction spacing and the second order reflection angles used to distinguish the domains a^1, a^2 and c (Lattice parameters: $a = 3.985$ Åand $c = 4.029$ Å; wavelength of X-ray: $\lambda = 0.67$ Å)

	Spacing d	(χ')	theta (2θ)
a^1-reflection [402]	1.7860 (Å)	26.314°	44.065°
a^2-reflection [240]	1.7821 (Å)	26.565°	44.166°
c-reflection [204]	1.7978 (Å)	26.818°	43.761°

In the same way, we can obtain d_2, χ_2', θ_2 for a^2-type domain, and d_3, χ_3', θ_3 for c-type domain. Therefore, the diffraction angles used to distinguish a^1, a^2 and c domains in $BaTiO_3$ single crystal configured as in figure 3.10 are as given in table 3.1.

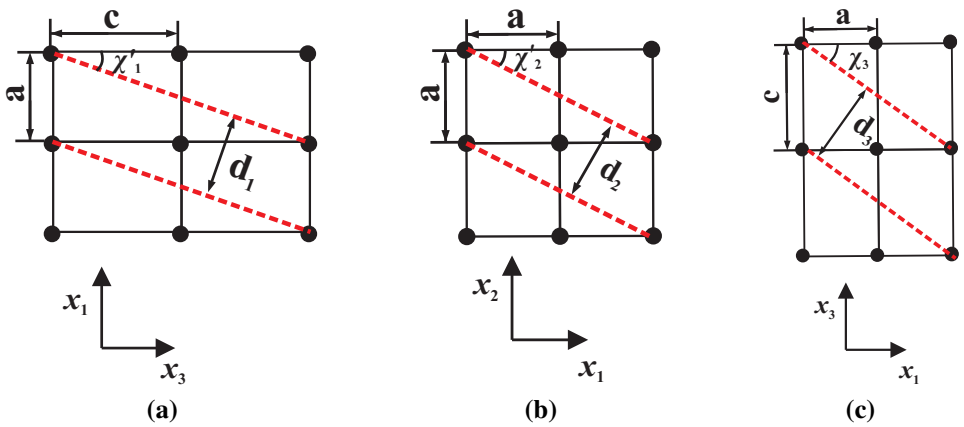


Figure 3.10: Asymmetric reflections of $BaTiO_3$ single crystal with tetragonal phase: (a) a^1-reflection [402], (b) a^2-reflection [240], (c) c-reflection [204].

3.2.2 Strain measurement using X-ray diffraction

X-ray diffraction can detect strain using the distance between crystallographic planes, with the advantage of non-destructive measurement and high accuracy. Besides, it also shows capability in the measurement of residual stresses and mapping of strain.

To perform strain measurements the specimen is placed in the X-ray diffractometer, and it is exposed to an X-ray beam that interacts with crystal lattice to cause diffraction patterns. If the

wavelength of the X-ray beam is fixed, changing the interference-planar spacing d will result in a different diffraction pattern. The interference-planar spacing of an unstrained sample produces a characteristic diffraction pattern. When a sample is strained, elongations and contractions are produced within the crystal lattice, which change the interference-planar spacing of the lattice planes. This change will cause a shift (or broadening) in the diffraction pattern. Figure 3.11 shows the shift in the Bragg peak of rocking curve when the specimen is in tension. The spacing (d_0) between diffracting atom layers of a material that is free from strain will produce a characteristic diffraction pattern. If we know the unstrained inter-planar spacing d_0, we can get strain:

$$\varepsilon = \frac{d - d_0}{d_0} \tag{3.5}$$

From Eq. 3.5, note that measurement of an unstrained sample of the material is required.

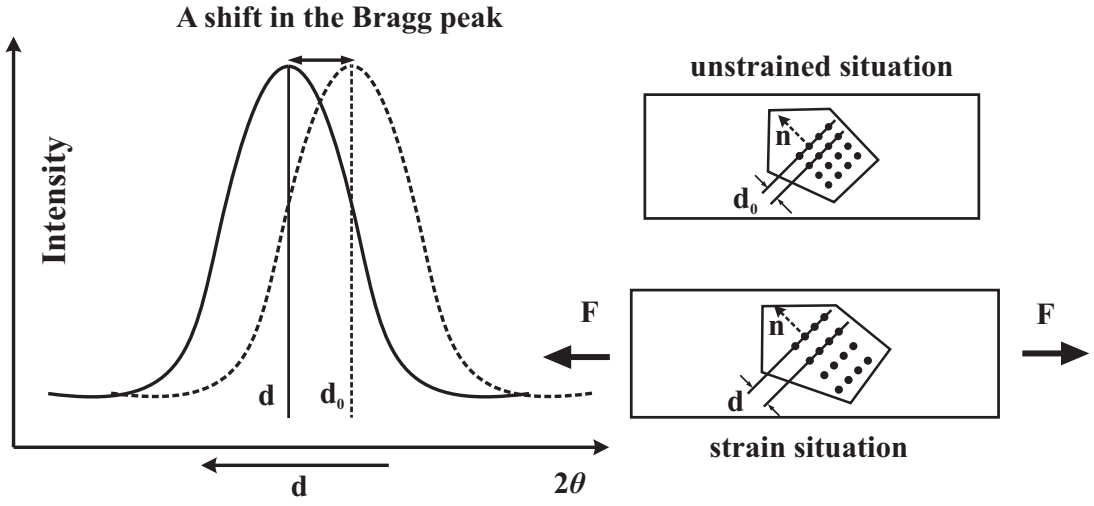


Figure 3.11: Shift in the Bragg peak produced by change in spacing between diffracting atom layers.

The changes in the d-spacings due to the strain in the sample are very small, typically in the third decimal place. According to the Bragg's Law, the d spacing which a diffraction peak is obtained using a particular incident wavelength is a function of $\sin\theta$. Therefore, when there is a change in d-spacing Δd, the change in position of a diffraction peak $\Delta\theta$ is obtained by differentiating Bragg's law as follows:

$$2\left[\Delta d \sin\theta + d\cos\theta\Delta\theta\right] = \Delta\lambda \tag{3.6}$$

Since λ is constant, $\Delta\lambda = 0$, giving the strain as

$$\epsilon = \Delta d/d = -\cot\theta\Delta\theta \tag{3.7}$$

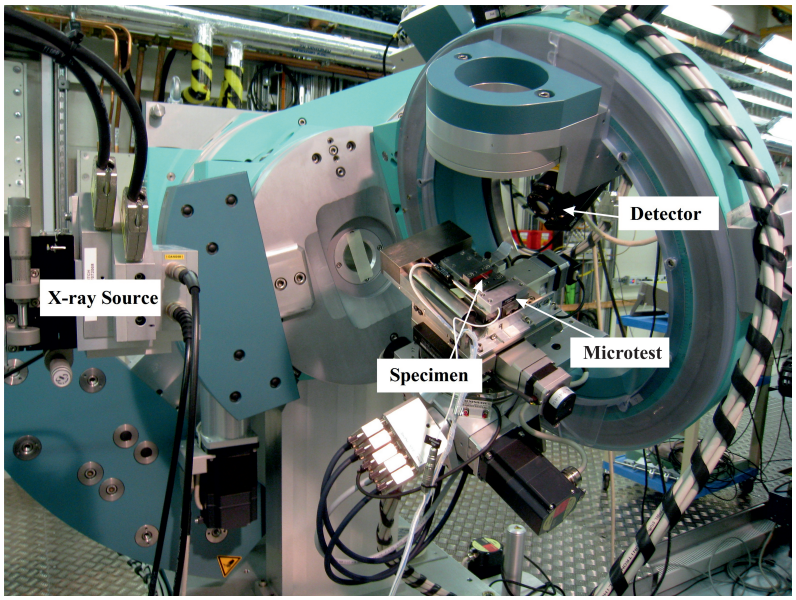
This equation gives the formula for measurements taken normal to the reflection surface.

3.3 Synchrotron X-ray experiment to identify domain needles

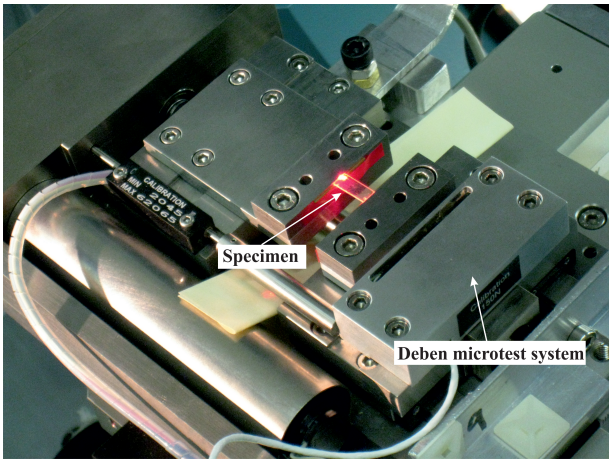
The following experiments were performed using at 18.6 keV light ($\lambda = 0.67$ Å) in reflection topography. Unfocussed, monochromatic synchrotron X-ray light was used at beamline B16, Diamond Light Source, UK. In the experiment, a specimen containing needle domains was mapped using the asymmetric reflections. In the different regions of the specimen surface, the comb pattern with the fine needle domains and coarsely spaced needle were observed. Figure 3.12a gives the general arrangement of the experiment, in which the X-ray beam is reflected by the specimen and collected by the detector. The dimension of the $BaTiO_3$ single crystal specimen with needle domains were $10 \times 4 \times 0.55$ mm, as shown in figure 3.12c. The specimen was mounted in a Deben microtest machine, capable of applying controlled force and displacement to the specimen surface. This was then mounted onto a 5-circle Huber diffractometer, and the 10×4 mm surface of the specimen was exposed to incident light. Figure 3.12b shows the specimen illuminated by laser light, indicating the location of the X-ray beam during the experiment. A Photonic science X-ray eye MiniFDI camera with 1392×1040 pixels (pixel size = 6.5 μm) was used to detect the reflection from the specimen. In the experiment, we adopt the

X-ray topography technique to map the different domain structures and to measure the strain field around a needle tip.

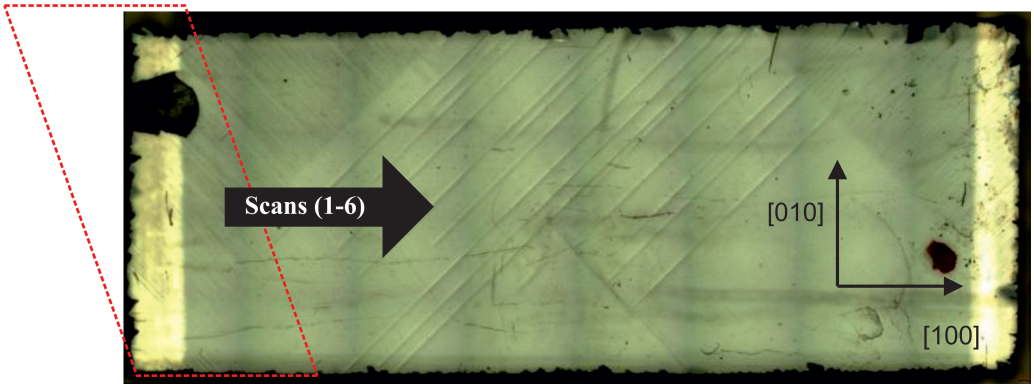
In the experiment, the MiniFDI camera placed at the detector distance 115 mm collects the 2^{nd} order reflections of type [402] at 1 s time intervals. The detailed diffraction angles have been given in table 3.1. The beam was slitted to 2 mm width by 3 mm height, and used to scan the specimen surface. A total of 6 scans were collected to map the entire surface of the specimen, through moving specimen using the $x-y$ stage of the diffractometer with steps of 1.5 mm. Dashed red lines in figure 3.12c show the illuminated region of the specimen at a typical scan position. Overlapping regions in the scans enabled the construction of a collage map of the entire specimen surface. The specimen was rocked in the range of ω between 21.02° and 23.02° with steps of 0.005°. Figure 3.13 gives the rocking curve of scan-1; the presence of a^1, a^2, and c domains on the specimen surface can be distinguished. The scanning direction (scan 1-6) was from left to right relative to figure 3.12c. The domain structure on the specimen surface is composed of a^1 and a^2 comb domains at the upper left corner of sample, fine a^1 needle domains in the central part, embedded in a large area a^2-matrix domain, and c domains (c bottom and c top). According to the rocking curve, each domain type corresponds to a narrow range of ω values around peaks on the rocking curve. For example, the range of 21.975°-22.095° is defined for the a^2-matrix domain, and the range of 21.79°-22.975° is for the configuration of a^2-comb. Due to slight curvature of the crystal surface and tilt between the different domains, only a portion of the specimen surface satisfies the Bragg condition at any one ω angle. Hence the need for the rocking curve to detect different domains and misfit strain. Integrated images can be obtained by summing intensity over the corresponding range of ω values for each domain type. This is a powerful technique because it allows us to identify domains and to map their location/ shape on the sample surface. For example the c (top) peak is barely visible in figure 3.13, but can be clearly identified because the detector images from the corresponding ω angles show a bright spot reflected from the top edge of the sample.



(a)



(b)



(c)

Figure 3.12: X-ray observation (a) Experimental set up of X-ray observation showing X-ray source, specimen and detector (b) Specimen illuminated by the X-ray beam (c) Optical micrograph of $BaTiO_3$ single crystal specimen with needle domains observed by Potnis [92].

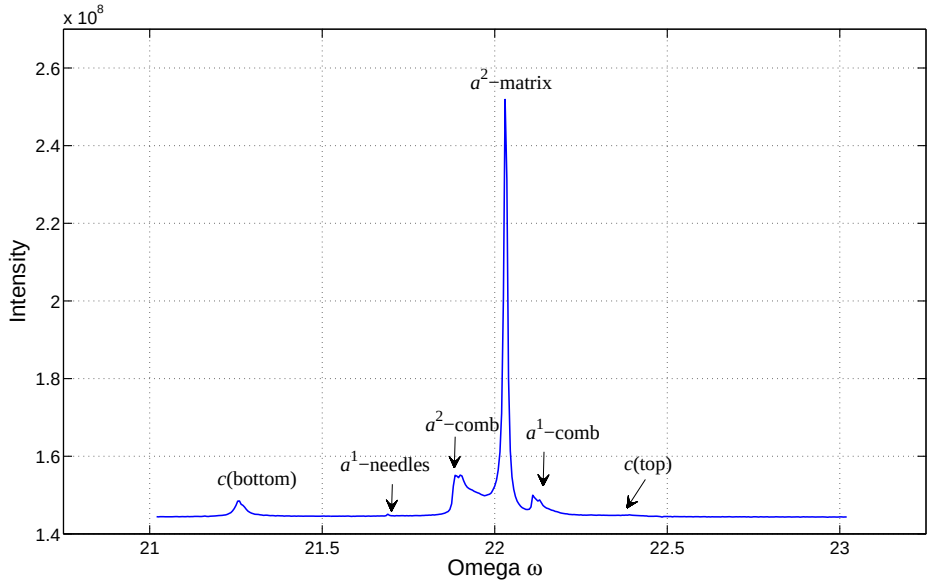
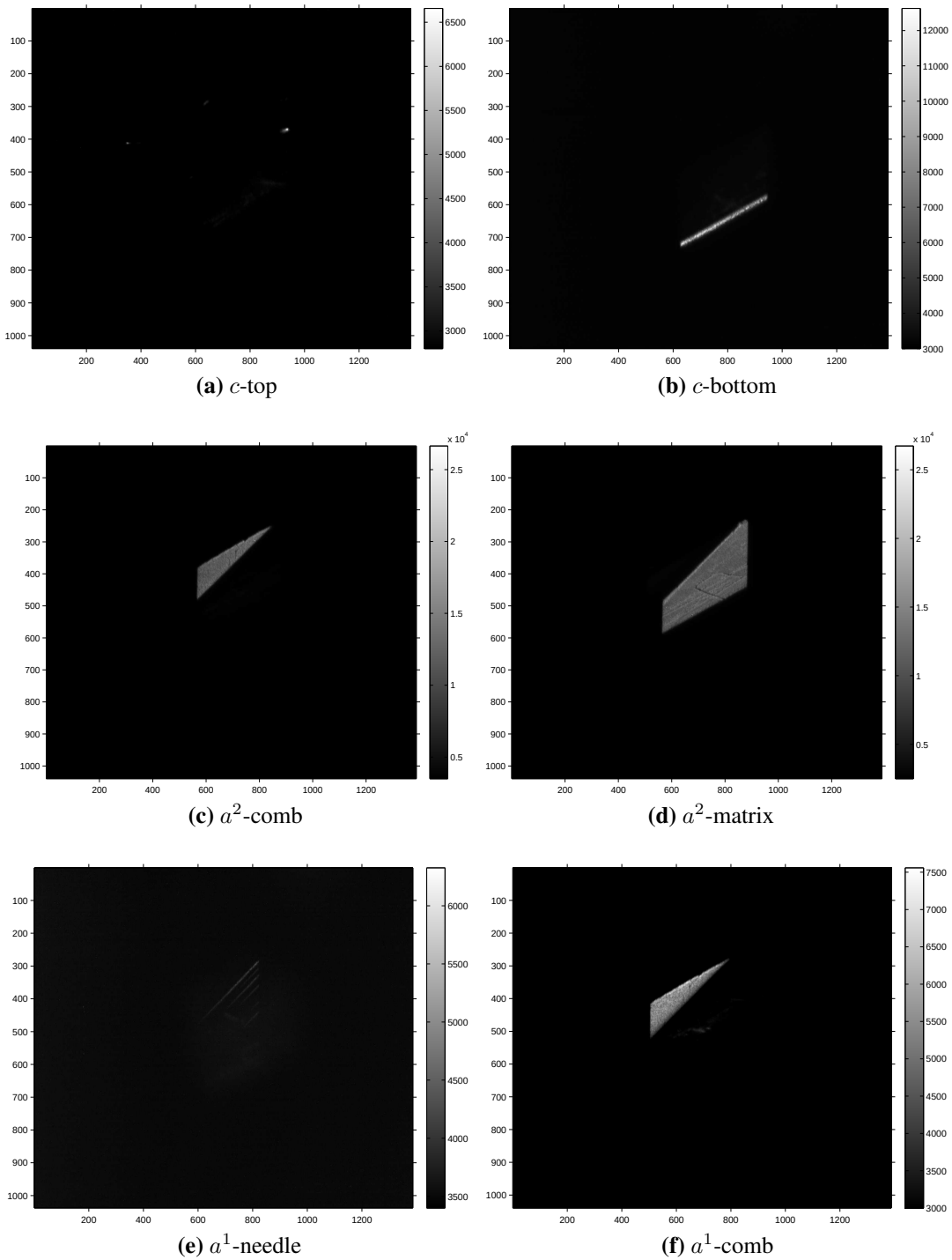


Figure 3.13: Different types of domains showing at scan 1 rocking curve of sample located at $x = -1$ mm and $y = 0.41$ mm, when the specimen is rocked in the range of ω between 21.02° and 23.02° with step of 0.005°.

Figure 3.14 gives the integrated images of each domain type including a^1, a^2, and c domains from scan-1. In these images, the reflections of the different domains are spatially separated due to the difference in angle 2θ and χ listed in table 3.1. The changing angle 2θ corresponds to a vertical displacement in spatial position on the detector. Therefore, reflections with larger angle 2θ appear vertically above those with smaller angle. Hence, the reflections of c domain are vertically displaced downwards, compared to the reflections of a^1 and a^2 domains. In addition, through adjusting the angle χ, the reflections of a^1 and a^2 domains can be distinguished by displacement in the horizontal direction. a^1 domains appear displaced horizontally to the left side of a^2 reflections, according to the diffraction angle given in table 3.1. Therefore, from the results, c domains which were not visible in the measurements result are detected near the specimen edges. The a^1 and a^2 domains are also detected separately. 90° a-a type needle domains are clearly observed. They are arranged in comb-like patterns. The 90° a-a combs appear both as finely spaced structures and as coarsely spaced individual needles.

The integrated images of figure 3.14 each map a single type of domain structure from



(a) c-top **(b)** c-bottom

(c) a^2-comb **(d)** a^2-matrix

(e) a^1-needle **(f)** a^1-comb

Figure 3.14: Integrated images of the different domain types detected by X-ray in $BaTiO_3$ single crystals

the first scan, which corresponds to a section of the sample near the left-hand edge, as seen in figure 3.12c. These topographic maps were further processed by Potinis [52, 92] to combine all the detected domain structures together. After removing foreshortening caused by the ω and χ rotations, and using false colouring to represent the various ω ranges around particular domains types, Potnis produced the image shown in figure 3.15 [92]. The combined image of figure 3.15 shows a good agreement with the optical micrograph presented in figure 3.12. It demonstrates that X-ray mapping can resolve fine structures; the detected fine needles have width about $10\ \mu$m.

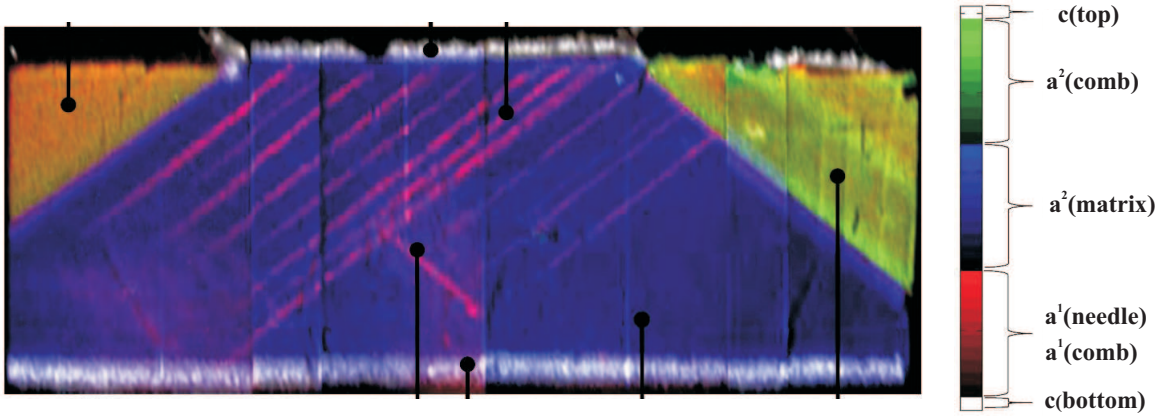


Figure 3.15: Combined image with colourful domains [92].

3.4 Measurement of domain needle shape

In this part, we will further consider the shape of the fine needle domain. The exposure time was increased to 2 s. The range of rocking ω was reduced to between $21.66°$ and $21.72°$ with fine steps of $0.001°$. This allowed us to capture data for the fine a^1 needles in greater detail. All other settings of the X-ray source and detector were kept the same as above. An integrated image obtained through summing intensity over the rocking range ω, is shown in figure 3.16. The shape of this needle domain is made clearer in figure 3.17, which is obtained by subtracting the average background intensity from the whole integrated image (figure 3.16). From this

figure, the shape of the needle domain appears as a sharp wedge. The opening angle of its tip is small, about 1°. The total intensity change along needle longitudinal direction was computed and plotted. To make the plot, the needle longitudinal direction from tip to end is first defined as the x positive direction, as marked in figure 3.17. To smooth the intensity data, a Gaussian spot was multiplied in at each point. We used a spot of size 5 x-pixels by 10 y-pixels over the whole integrated needle. The weighted summation function for the sampling spot was thus the gaussian,

$$f = \exp(-(\frac{x - x_d}{5})^2 - (\frac{y}{10})^2) \tag{3.8}$$

where, x_d is the pixel distance of the sampled spot from the needle tip, and y is transverse distance in pixels. According to distance-pixel conversion, the corresponding value of x_d in the diffractometer x-y coordinate system is from -0.4225 mm to 1.7875 mm, (pixel size=6.5 μm). The scan with maximum summation intensity (I_m) serves as reference; the weighted summed intensity of each spot was normalized by I_m. Figure 3.18 shows the resulting variation of normalized total intensity along the x-axis direction. From this figure, the normalized intensity shows a linear trend: a fitted line is shown (dashed) in the figure 3.18. This indicates that the needle domain has a sharp wedge shape, with a well-defined wedge angle.

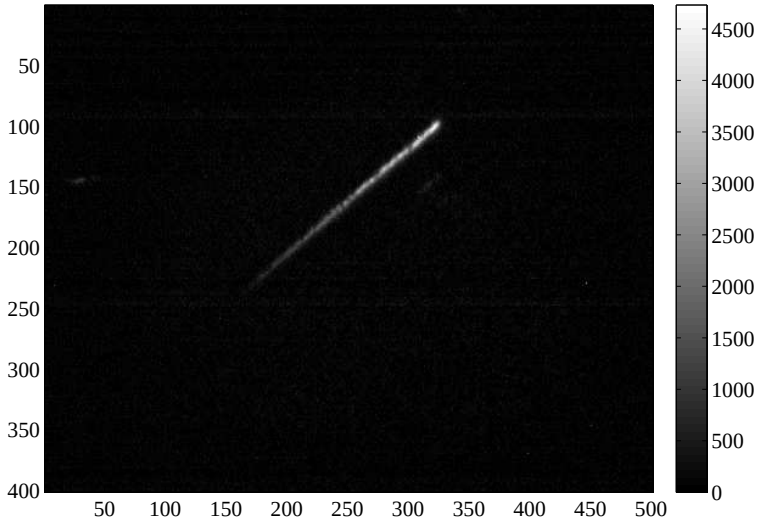


Figure 3.16: Integrated image of a needle domain.

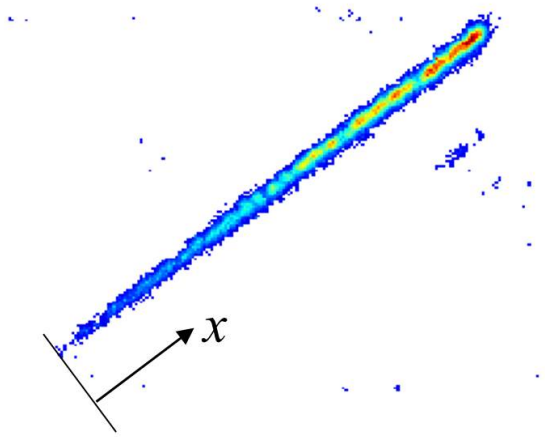


Figure 3.17: Wedge shape of needle domain.

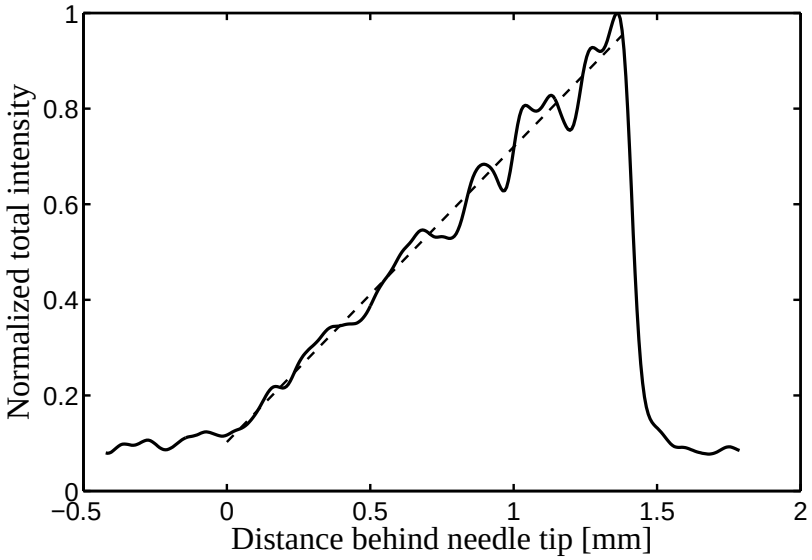


Figure 3.18: Variation of normalized total intensity in spot area along x-axis direction. Solid line is intensity data line; Dash line is linear fitted line.

Based on the result of a sharp wedge shape of needle domain observed in this experiment, we can improve the model of the needle domain and use a group of dislocations coupled with line charge, spreading over the whole wedge length. This more complex modelling will be discussed in Chapter 4. Additionally, the shape of the needle domain can be used to estimate the lattice friction resisting domain wall motion. In Chapter 2, we focused on a blunt needle domain modelled as a single effective dislocation coupled with line charge. This simplification

facilitates the study of interaction of needle domains.

3.5 Measurement of strain field around a needle tip

The existence of a needle domain gives rise to an internal stress field and electric field around the needle tip. The needle domains as crystal defects influence the polarization switching process and induce the crack propagation in crystals. In this section, we will use the X-ray measurements in an attempt to map the strain field distributing around the needle domain.

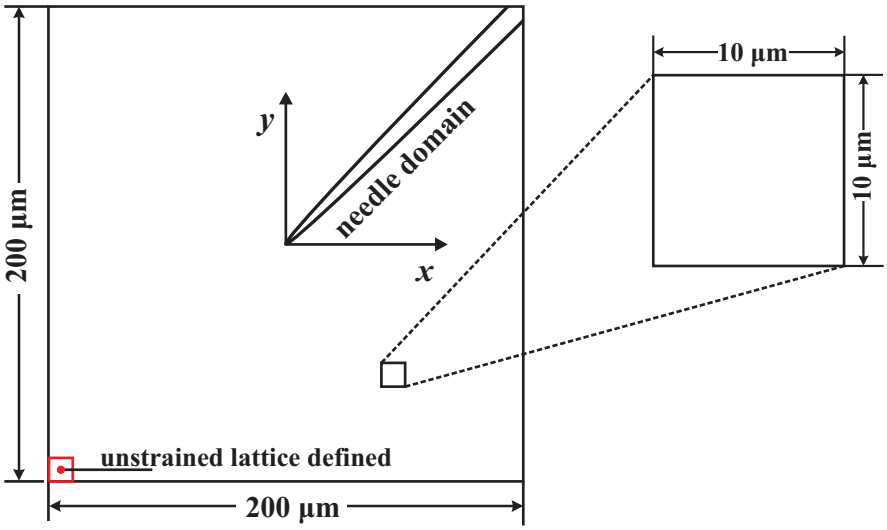


Figure 3.19: The scanning range (200 μm $\times$ 200 μm) around needle tip. The lattice point located at the bottom-left corner was defined as unstrained lattice.

In the experiment, we chose an a^1 needle tip to scan the surrounding field over range of 200 μm $\times$ 200 μm. We examined the a^2 reflection from the surrounding parent domain to look for strain. The corresponding a^2 [240] reflection was measured for strain. During the process of scanning, the X-ray beam was slitted to a spot light of 10 μm $\times$ 10 μm, as a moving and microsize strain gauge to detect the change of d-spacing caused by strain. It scanned the whole range with x-direction step 10 μm and y-direction step 10 μm, as illustrated in figure 3.19. Note that this was done by moving the sample, not the beam slits. The diffraction angles are set as $2\theta = 43.6°$, and $\omega = 22.032°$. The MiniFDI camera was then kept in the same position

which is distant from specimen 115 mm to collect reflection images at 2 s time interval. We defined the bottom-left corner, which is far from the needle tip, as an unstrained lattice point. The measuring strains in the whole scan range are relative to this reference position which is marked in figure 3.19.

According to Eq. 3.7, the calculation of $\Delta\theta$ is a key process in the measurement of strain. The strain induces the change in the d-spacing of the interference lattice planes. When the X-ray beam is fixed, this change will result in a different diffraction pattern through moving the sample. Specifically, the vertical position of the diffracted spot on the MiniFDI camera changes with strain. Because the spot moved by distances only of order a few pixels, it was necessary to compute the centre of intensity of each diffracted spot. To evaluate the difference in the diffraction pattern, the change in mass center of total intensity of each spot scan, relative to the unstrained lattice was found. In each spot scan, the mass center $(\bar{\xi}, \bar{\eta})$ is calculated as follows,

$$\bar{\xi} = \frac{\iint \xi \cdot I(\xi,\eta)\ \mathrm{d}\xi\ \mathrm{d}\eta}{\iint I(\xi,\eta)\ \mathrm{d}\xi\ \mathrm{d}\eta} \tag{3.9}$$

$$\bar{\eta} = \frac{\iint \eta \cdot I(\xi,\eta)\ \mathrm{d}\xi\ \mathrm{d}\eta}{\iint I(\xi,\eta)\ \mathrm{d}\xi\ \mathrm{d}\eta} \tag{3.10}$$

where, the local coordinates of each spot scan image for different positions (in x-y coordinate) are ξ and η. $I(\xi,\eta)$ indicates the intensity of the different position (in ξ-η coordinate) in one spot scan. The total intensity $I_t = \iint I(\xi,\eta)\ \mathrm{d}\xi\ \mathrm{d}\eta$ is the sum of intensity over the surrounding region of the spot on the detector. Due to the the changing angle 2θ corresponding to a vertical displacement in spatial position on the detector, only the changing displacement in η-direction is required to calculate the shift ($\Delta\theta$) of the Bragg peak. Figure 3.20 illustrates that the changing d-spacing caused by the strain induces the change ($\Delta\theta$) in Bragg angle. Through moving the specimen, the different diffraction peaks for the lattice yielding different strain can be located, and the corresponding Bragg angles are obtained. Here the angular changes were sufficiently

small that it was not necessary to rock the sample. The angle θ between the reflection plane and X-ray beam corresponds to the lattice with the unstrained state. When the lattice is strained, the changing d-spacing causes the change in the Bragg angle, which caused the displacement from A to B on the detector. Due to the small angular change, we can treat the distance OA=OB=L and then obtain the calculation of $\Delta\theta$ as follows,

$$\Delta\theta = AB * c/L \tag{3.11}$$

where, $L = 115$ mm is the distance between the detector and specimen. The changing displacement AB is equal to $\bar{\eta} - \bar{\eta}_r$ ($\bar{\eta}_r$ is for reference position). The pixel size c is equal to 6.5 μm. According to Eq. 3.7 and figure 3.10b, we can compute the strain $\varepsilon_{[2\ 4\ 0]}$ field of a^2 reflection around the a^1 needle tip.

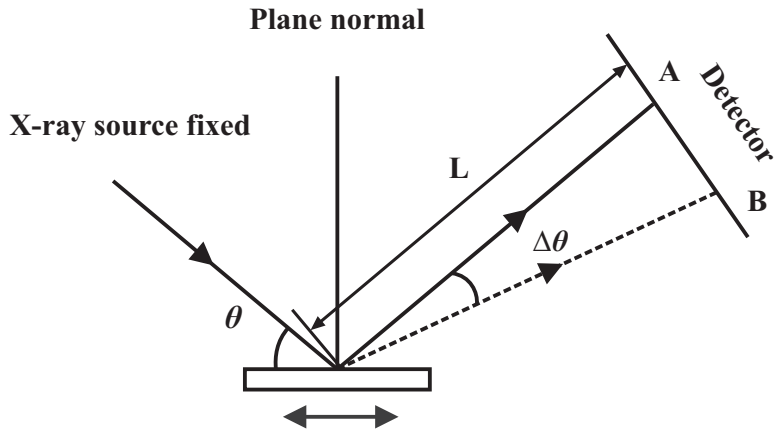


Figure 3.20: Spot scan (10 μm $\times$ 10 μm) over the range of 200 μm $\times$ 200 μm. The lattice located at bottom-left corner is defined as unstrained lattice.

Figure 3.21 shows the contour map of the needle microstrain obtained from experimental measurement. Additionally, the simulation result computed by the model mentioned in section 2.3 is also presented. Considering the shape of the needle domain, we adopt a group of the equivalent dislocations b_s and line charge q_s spreading over the needle tip to model the field due to the needle tip, as illustrated in figure 3.22b. Correspondingly, figure 3.22a gives the simulation result about the contour map of strain $\varepsilon_{[2\ 4\ 0]}$ due to one needle domain under the

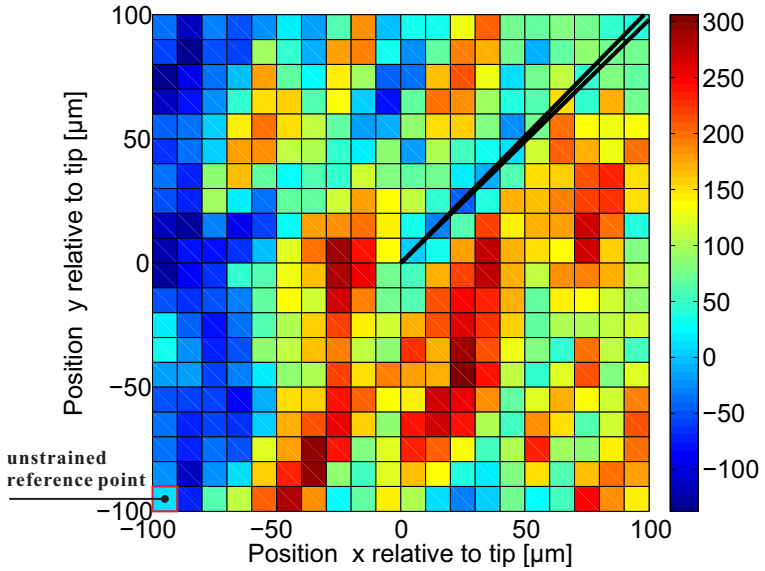
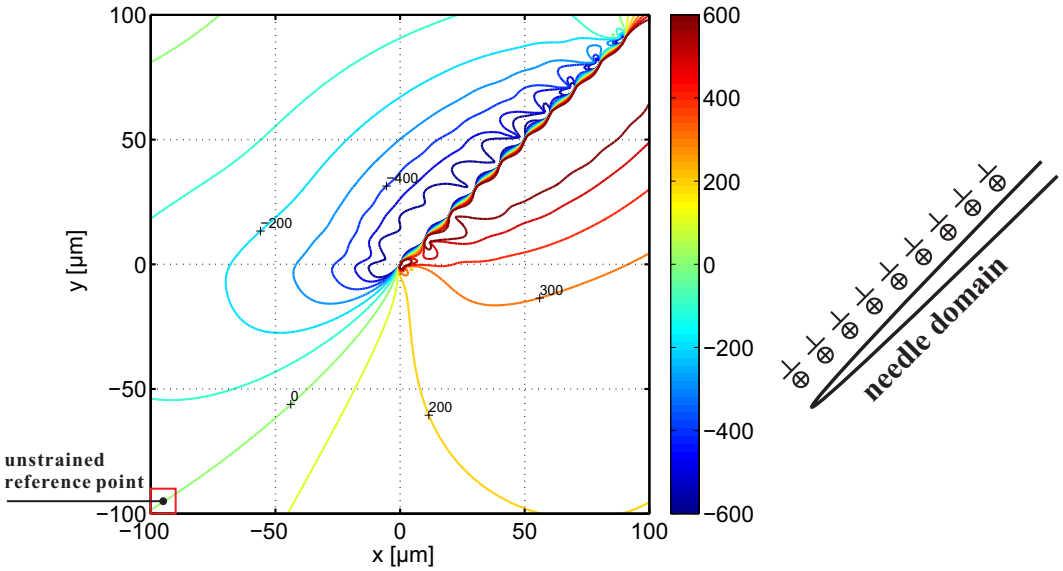


Figure 3.21: Microstrain field around the needle tip in [240] direction measured by X-ray diffraction.



(a) **(b)**

Figure 3.22: Microstrain field around the needle tip in [240] direction calculated using the simulation model.

plane stress condition. Comparing figures 3.21 and 3.22a, we find that they have similar magnitude of microstrain. However, it is obvious that the contours of strain field are different. One reason is the assumption of a perfect crystal adopted in simulation. In the experiment,

the existence of defects can also change the d-spacing, disturbing the precision of strain measurement. In addition, the strain field measured is influenced by the boundary condition and other nearby microstructures. These factors are not considered in simulation. Finally, it should be commented that as the reflected spot size was of order 2-3 pixels, but the movement due to strain was only of order 1 pixel, the measurements were close to the resolution limit of the experiment. This is also part of the reason for difference between the experimental result and simulation pattern.

3.6 Conclusions

- Under the observation of the optical microscopy, the needle domains are found when the $BaTiO_3$ single crystals cool through Curie temperature. Needle domains appear in well defined patterns such as comb and herring-bone.
- The needles align with crystallographic directions according to theory of compatibility.
- From X-ray measurement, the needle-tips are long, wedge shaped regions with opening angle about 1°. The measurement of the needle-tip shape contributes to the improvement of the needle domain model and the estimation of the lattice friction.
- The needles produce near tip strain fields with similar magnitude to the predictions using dislocation fields, though the experiments were not able to give a reliable strain contour map.

4

Chapter 4 Simulation of needle fields

Based on Barnett and Lothe's theory provided in the chapter 2, we will discuss the simulation results of internal stress and electric fields produced by needle domains in $BaTiO_3$ single crystals under the plane strain condition. First, the interaction of pairs of needle domains in an infinite piezoelectric body is studied by computing the interactive force and the total energy. Additionally, groups of needle domains in the comb-like and herringbone patterns are investigated.

4.1 Nondimensionalization

Nondimensionalization is first applied to make the results independent of the influence of physical dimensions, and to help avoid numerical instability during the computing process, especially in matrix inversion.

We choose characteristic parameters including spontaneous polarization magnitude p_0 (0.26 $\mathrm{C/m^{-2}}$), spontaneous strain magnitude ε_0 (0.0073), electric field E_0 (0.1×10^6 V/m) and the width of a typical needle domain w (about 10 μm). Therefore the constitutive Eqs. 2.11 and 2.12 are nondimensionlized by these characteristic parameters as:

Table 4.1: Summary of dimensionless quantities

	Units	Non-dimensional
Stress, σ	Pa	$\sigma^* = \sigma/\sigma_0$
Strain, ε	-	$\varepsilon^* = \varepsilon/\varepsilon_0$
Electric displacement, D	$\mathrm{C/m^2}$	$E^* = E/E_0$
Elastic constants, C	Pa	$C^* = C\varepsilon_0/\sigma_0$
Piezoelectric constants, e	$\mathrm{C/m^2}$	$e^* = E_0 e/\sigma_0$
		$e^{**} = e\varepsilon_0/p_0$
Dielectric constants, κ	F/m	$\kappa^* = E_0\kappa/\sigma$
Burgers vector, b_i	m ($i = 1, 2, 3$)	$b^* = b/\varepsilon_0 w$
	V ($i = 4$)	$b^* = b/E_0 w$
Line charge vector, q_i	N/m ($i = 1, 2, 3$)	$q^* = q/\sigma_0 w$
	C/m ($i = 4$)	$q^* = q/p_0 w$

$$\frac{\sigma}{\sigma_0} = \left(\frac{C\varepsilon_0}{\sigma_0}\right)\frac{\varepsilon}{\varepsilon_0} - \left(\frac{eE_0}{\sigma_0}\right)\frac{E}{E_0}, \qquad \sigma^* = C^*\varepsilon^* - e^*E^* \tag{4.1}$$

$$\frac{D}{p_0} = \left(\frac{e\varepsilon_0}{p_0}\right)\frac{\varepsilon}{\varepsilon_0} + \left(\frac{\kappa E_0}{p_0}\right)\frac{E}{E_0}, \qquad D^* = e^{**}\varepsilon^* + \kappa^*E^* \tag{4.2}$$

where, the dimensionless variables are defined as σ^*, ε^*, E^*, C^*, e^*, D^*, κ^*, and e^{**}, which are listed in table 4.1. To make dimensionless piezoelectric constants $e^* = e^{**}$, we can obtain a stress characteristic variable $\sigma_0 = E_0 p_0/\varepsilon_0 = 3.56$ MPa. Additionally, the generalized Burgers vector $\mathbf{b} = [b_1, b_2, b_3, \triangle\varphi]^T$ components are normalized by $\varepsilon_0 w$ ($i = 1 \ldots 3$) and $E_0 w$ ($i = 4$). The generalized line charge vector $\mathbf{q} = [q_1, q_2, q_3, q_4]^T$ is similarly normalized using $\sigma_0 w$ ($i = 1 \ldots 3$) and $p_0 w$ ($i = 4$).

4.2 Isotropic reference case

Before we compute the field of a needle-shaped domain in the anisotropic case, we will first present the field of an edge dislocation in an isotropic medium. These results will serve as a reference case to check calculations.

The elastic stress fields $(\sigma_{xx}, \sigma_{xy}, \sigma_{yy})$ of this dislocation are well-known [71, 93]

$$\sigma_{xx} = -\frac{Gb}{2\pi(1-\nu)} \frac{y(3x^2+y^2)}{(x^2+y^2)^2} \tag{4.3a}$$

$$\sigma_{xy} = \frac{Gb}{2\pi(1-\nu)} \frac{x(x^2-y^2)}{(x^2+y^2)^2} \tag{4.3b}$$

$$\sigma_{yy} = \frac{Gb}{2\pi(1-\nu)} \frac{y(x^2-y^2)}{(x^2+y^2)^2} \tag{4.3c}$$

where, G is the shear modulus, b is the length of the Burgers vector of the dislocation, and ν is Poisson's ratio. Note that the fields are of order x^{-1} and so linear elasticity will break down as the dislocation is approached. A core region of radius r_0 can be defined such that the elastic fields are assumed to be sufficiently accurate outside the core (distance $r > r_0$). Typically r_0 is taken to be of the order of the lattice spacing or Burgers vector.

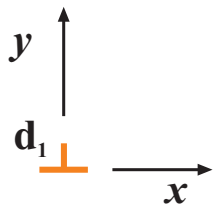
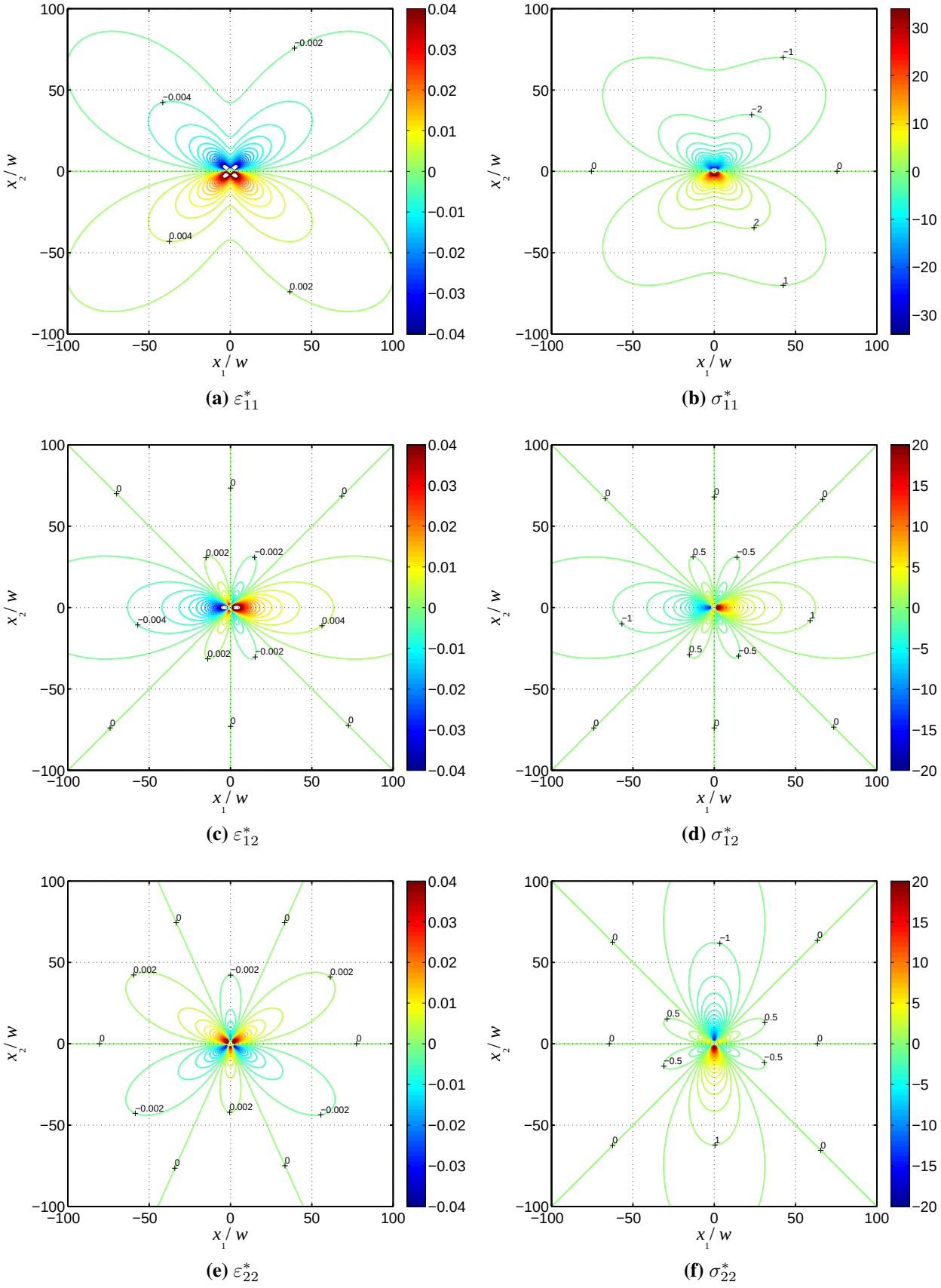


Figure 4.1: An edge dislocation in isotropic material

The solution of dislocations and line charges in anisotropic piezoelectric material derived by Barnett and Lothe can be degenerated to the case of an isotropic dislocation by setting piezoelectric constants $e_{mij} = 0$, namely the electromechanical effect is ignored. Additionally, the isotropic material constants mentioned in section 2.1.2 are also kept in the following simulation. An edge dislocation (d_1) shown in figure 4.1 is considered. This edge dislocation is at the origin of an an $x - y$ coordinate system. Its Burgers vector **b** is in the x direction.

Isotropic dislocation fields are calculated using Barnett and Lothe's method to compare with solutions obtained from Eqs. 4.3. The generalized Burgers vector of the degenerate case is $\mathbf{b} = [1\,0\,0\,0]^T$ and corresponding generalized line charge vector becomes $\mathbf{q} = [0\,0\,0\,0]^T$, namely no line force or charge. Figure 4.2 presents a selection of these fields computed by Barnett and



(a) ε^*_{11} **(b)** σ^*_{11}

(c) ε^*_{12} **(d)** σ^*_{12}

(e) ε^*_{22} **(f)** σ^*_{22}

Figure 4.2: Contour maps for various fields due to an edge dislocation in isotropic medium under plane strain, (a, c, e) the strain distributions, normalized by ε_0; (b, d, f) the stress distributions, normalized by σ_0.

Lothe's method in Matlab, which are in agreement with known theory of dislocations [71, 93], Eq. 4.3. The strain and stress fields shown in figure 4.2 are normalized by ε_0 (0.0073) and σ_0 (3.56 MPa) given in section 4.1, respectively.

4.3 Fields due to a single needle domain

In this section, we will give simulation results about the fields produced by a single needle-shaped domain including the stress, strain, electric field and electric displacement under the plane strain condition for a $BaTiO_3$ single crystal. Note that the $BaTiO_3$ is strongly anisotropic and shows strong electro-mechanical coupling. Better understanding of the fields due to a single needle domain is then used to further investigate the interaction of neighbouring needle domains. The simulation conditions are as follows:

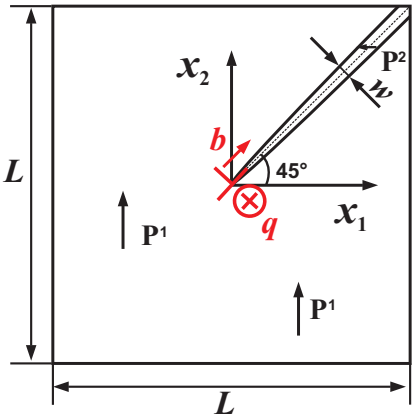


Figure 4.3: Computing range of a single needle domain modelled as one edge dislocation with a positive line charge

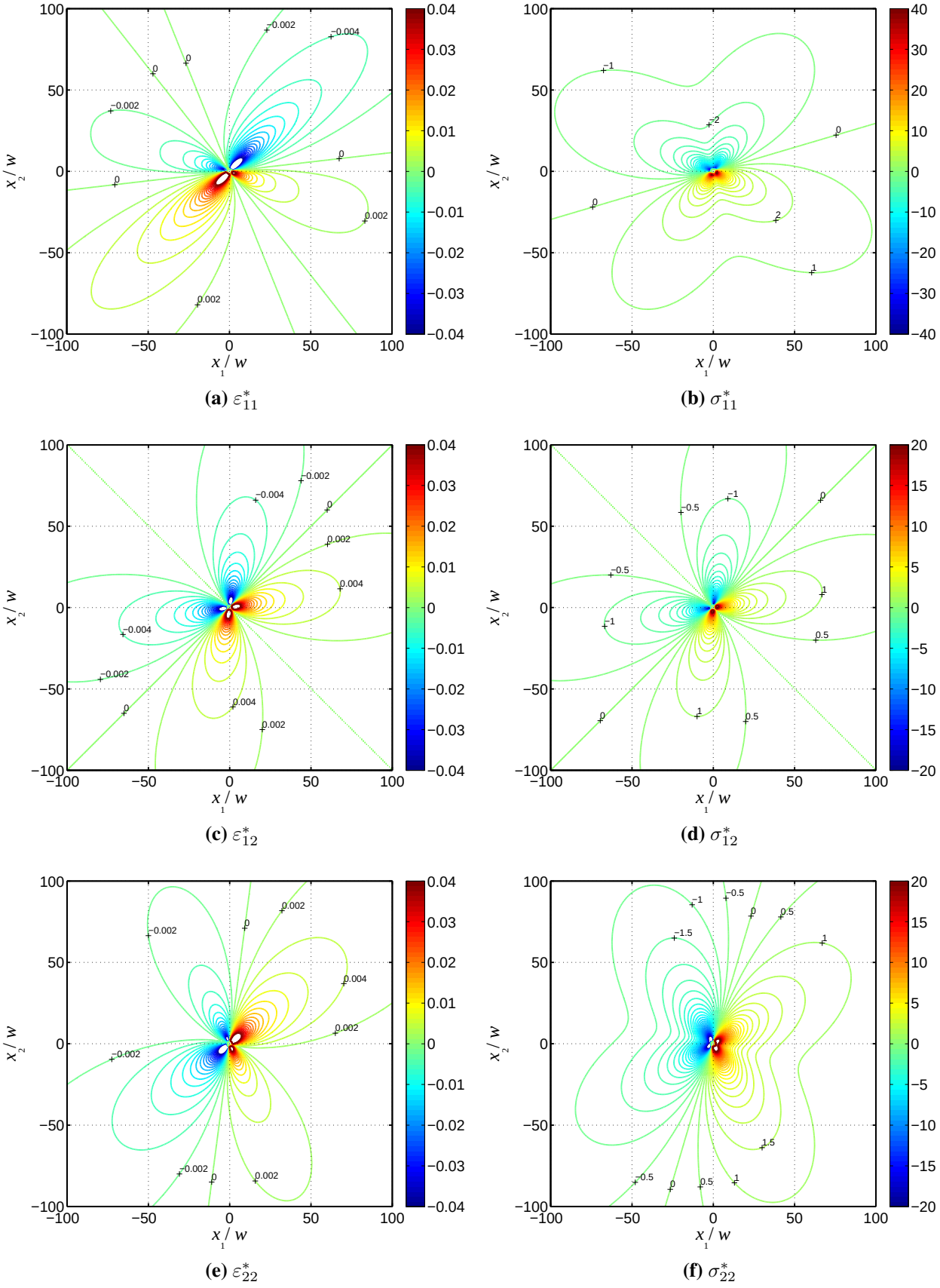
A needle-shaped domain with the width $w = 10$ μm is oriented at $45°$ to the x_1 positive direction. Its needle tip is fixed at the origin of the (x_1-x_2) coordinate system, as shown in figure 4.3. A square area with side of $L = 200w$ is selected for simulation. The polarization vectors of parent domain and needle domain are $\mathbf{P}^1 = [0\ 1\ 0]^T p_0$ and $\mathbf{P}^2$ =[-1 0 0]$^T p_0$, respectively. Based on the analysis in section 2.3, we know that the field of a $45°$ needle domain can be approximated by that of an effective edge dislocation $\mathbf{b} = 3\sqrt{2}\varepsilon_0 w/2\,[1\ 1\ 0\ 0]$ with a positive

line charge $\mathbf{q} = \sqrt{2}p_0 w\,[0\ 0\ 0\ 1]$, which is represented symbolically by $\perp$ and $\oplus$ as shown in figure 4.3.

Figure 4.4 shows the strain and stress fields produced by a single needle domain, which are normalized by ε_0 (0.0073) and σ_0 (3.56 MPa) given in section 4.1, respectively. These results are compared with the isotropic reference case shown in figure 4.2. Because of the difference of Burgers vector direction, the strain and stress fields of the dislocation in an isotropic medium (presented in section 4.2) should be rotated by 45° anticlockwise for comparison. We find there are some characteristics in common between the anisotropic and isotropic cases. (1) The stress and strain fields have central antisymmetry with respect to origin point. (2) The stress and strain fields are singular at the dislocation core as expected. However, there are some obvious differences. The influence of anisotropy and the existence of the line charge distort the contour pattern of stress and strain fields for the anisotropic case. Especially, the zero-value locations in the contour map of stress and strain fields are different, which will influence the equilibrium position of interactive needle domains.

The combination of an effective edge dislocation and an effective line charge results in the generation of coupled mechanical and electrical fields. Therefore, the corresponding electric fields are shown in figure 4.5. This gives the contour maps of electric field components (E_1^* and E_2^*) surrounding a needle domain tip in $BaTiO_3$ single crystal. The electric field components are normalized by characteristic parameter E_0 (0.1×10^6 V/m).

The energy associated with a needle-shaped domain consists of two parts: the strain energy and the electrostatic energy, which is calculated by Eq. 2.39 given in section 2.4. Here, the contribution of domain wall energy is neglected as this is typically much less than the internal energy due to strain and electric fields. To avoid the singularity at the dislocation core, which would make the energy infinite, we cut out a central region ($2w \times 2w$) where the single dislocation model becomes inaccurate, when we integrate the whole field energy. The energy density field produced by one needle domain is shown in figure 4.6, which is normalized by



(a) ε^*_{11} **(b)** σ^*_{11}

(c) ε^*_{12} **(d)** σ^*_{12}

(e) ε^*_{22} **(f)** σ^*_{22}

Figure 4.4: Contour maps of strain and stress components under plane strain which are normalized by ε_0 and σ_0, representatively.

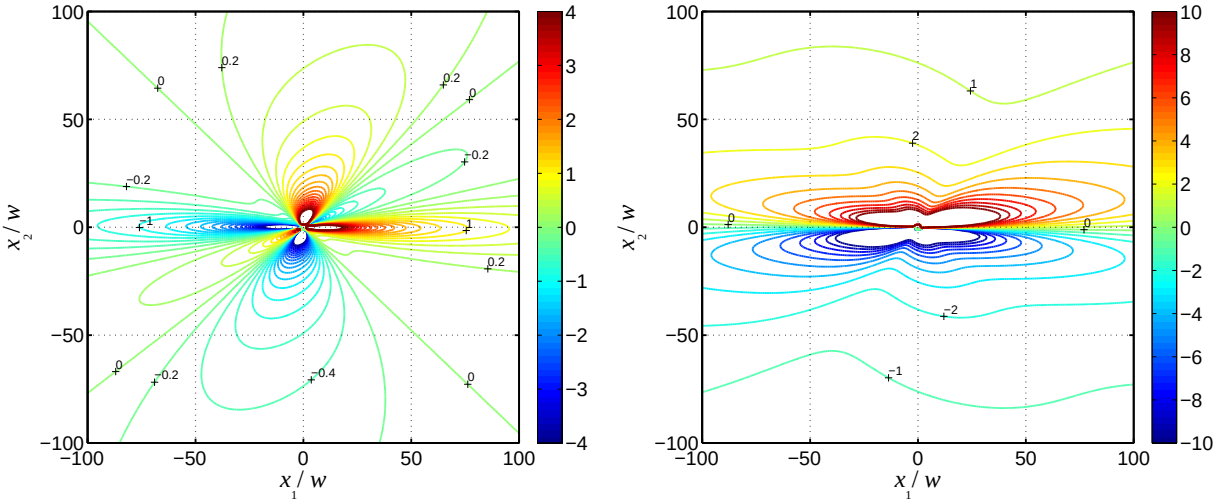


Figure 4.5: (a) Electric field component E_1^* (b) Electric field component E_2^* surrounding a needle domain in $BaTiO_3$ with Burgers vector [1 1 0] and positive line charge

$\varepsilon_0\sigma_0$ ($\varepsilon_0 = 0.0073, \sigma_0 = 3.56$ MPa) or p_0E_0($p_0 = 0.26$ Cm^{-2}, $E_0 = 0.1 \times 10^6$ V/m). The total energy U can be obtained by integrating the energy density over the whole field. The energy of one needle domain is proportional to w^2. Thus from the energetic point of view, the needle domain is driven to be narrow. This is an alternative way of viewing the effect of needle tip compatibility on needle geometry. Since the needles are typically thin, the approximation made by ignoring the inhomogeneity associated with the needle material is expected to be acceptable.

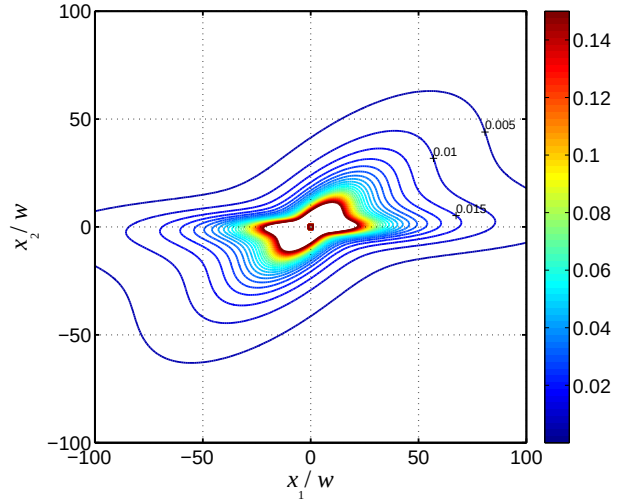


Figure 4.6: Energy density field surrounding a single needle domain, normalized by $\varepsilon_0\sigma_0$.

4.4 Interaction of the needle domains

In section 2.1.2, the interaction of two dislocations in an isotropic medium was discussed. The stability of equilibrium positions was further analysed. What happens to the interaction of the needle domains which are modelled as an edge dislocation coupled with a line charge? Does there exist an equilibrium position for a pair of interactive needle domains? In this section, we will focus on studying pairs of interactive needle domains in an infinite piezoelectric body by computing the interactive force and the total energy.

4.4.1 Identical tips in parallel domains

A pair of similar, parallel needle domains, which are labelled as N_1 domain and N_2 domain respectively, are shown in figure 4.7. The width of each needle domain is 10 μm. The polarization vectors of the parent domain and needle domains are $\mathbf{P}^1 = [0\ 1\ 0]p_0$ and $\mathbf{P}^{N_1} = \mathbf{P}^{N_2} =$[-1 0 0]$p_0$, respectively. Each needle can be represented by a dislocation with generalized Burgers vector **b** along [1 1 0 0] and a positive line charge q. The needle domain N_1 is oriented at 45° to the x_1 positive direction. Its needle tip is fixed at the origin of the (x_1-x_2) coordinate system. The similar needle domain N_2 is introduced at position (x_1, x_2) into the field of N_1. The interaction force on N_2 can be calculated using Eqs.2.41 and 2.42. A contour map of the extension force $F_e(x_1, x_2)$ on the needle N_2 is displayed in figure 4.8, which is normalized by $\sigma_0 w$. From this figure, we note that the position at which $F_e = 0$ lies close to the x_1 axis: these equilibrium positions lie on a line -0.03 (rad) to the positive direction of x_1 axis. When the N_2 needle-tip is located above this line, the extension force on the N_2 needle is negative and vice versa. Once the N_2 needle tip is away from the equilibrium position near the x_1 axis, the interaction force will drive it further away. Consequently the line $F_e = 0$ shows positions of unstable equilibrium. It is of interest that there appear to be no stable equilibrium positions for the pair of parallel needles. Unless the needle N_2 is infinitely far away from needle N_1, which means that they both breaks off the interactive relations.

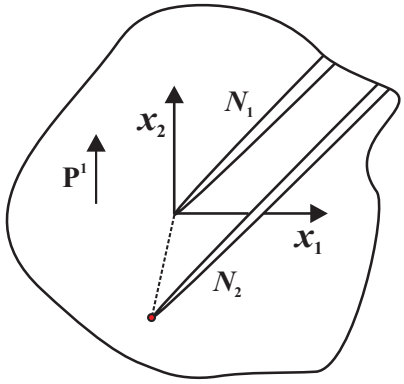


Figure 4.7: Schematic diagram of two parallel needle domains with identical tips.

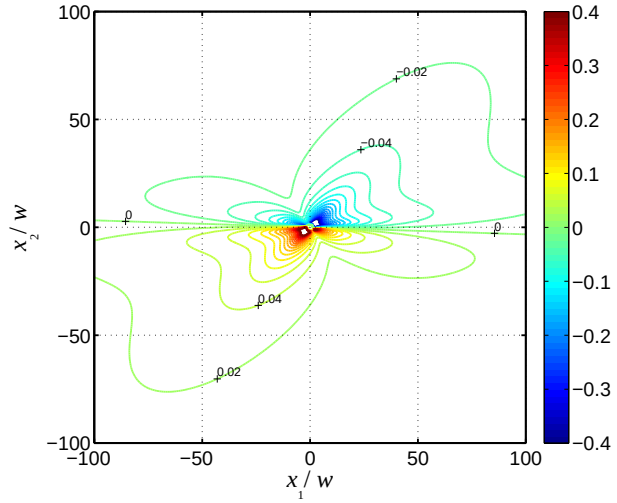


Figure 4.8: Contour map of extension force on N_2 domain for two parallel domains with identical tips.

From the energetic point of view, the absence of a stable equilibrium can also be shown. Two parallel needle domain (N_1&N_2) with spacing $s = 10w$ are considered, as shown in figure 4.9. The N_1 needle domain tip is fixed at the origin of the (x_1-x_2) coordinate system, while the N_2 needle domain keeps spacing s along the x_1 axis and moves along its longitude direction. Figure 4.9 show the normalized energy U/U_1 as a function of the normalized extension distance d/w from the crossing point of the needle domain N_2 and the x_1 axis. Here U is the total internal energy due to the two needle domains, and U_1 represents the energy produced by a single needle domain alone. The energies were computed approximately using the integral of Eq. 2.39 over a square region of side $800w$ which is enough to contain the interactive range of two needle domains. A square core region ($2w \times 2w$) around each needle tip was excluded from

the calculation. From this figure, it is evident that the position of d/w ($F_e = 0$) is an unstable position because the energy is at a maximum.

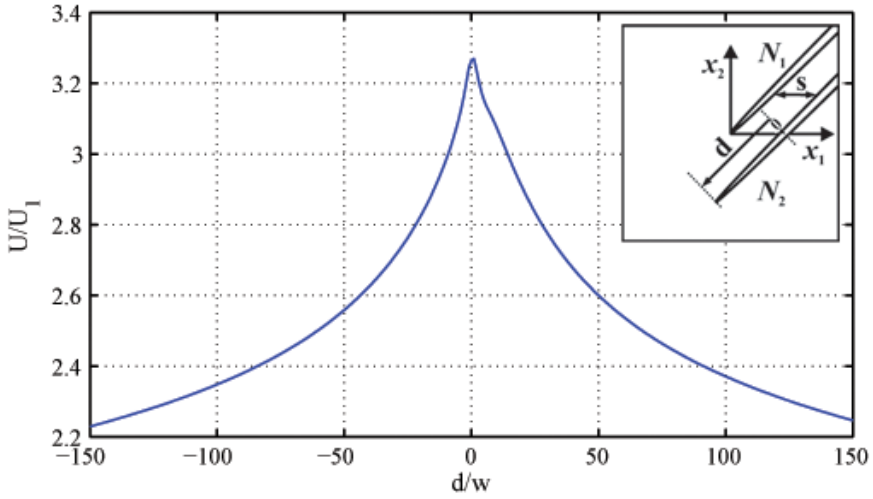


Figure 4.9: Normalized energy for two parallel domains with identical tips.

By including electromechanical coupling and anisotropy in the calculation, the result is qualitatively different from the interaction of parallel needle domains discussed by Bornarel [54, 55], where stable equilibrium positions were found. The key difference here is the presence of similarly signed effective line charges in $BaTiO_3$ that play a dominant role and tend to repel the needle tips. The presence of the effective line charges is based on the assumption of insulating behaviour: relaxing this assumption would allow the formation of a space charge distribution to partially screen the electric field component of the needle tip fields. Since comb-like arrays of parallel needle domains are observed in barium titanate, it appears likely that one or more of the following conditions is met: (1) Conduction allows a screening space charge distribution to form; (2) Lattice friction or crystal defects resist the needle tip motion; (3) Boundary conditions on a finite crystal can hold the needle domains in place. It should also be noted that needle domains can form with wedge-like tips that spread out the equivalent charges. A fuller discussion of these issues is deferred to later sections.

4.4.2 Perpendicular needle domains

In this section, we consider a pair of needle domains in a perpendicular configuration as shown in figure 4.10. As previously, the N_1 needle domain is located at the origin of the (x_1-x_2) coordinate system, while the needle N_2 which is perpendicular to the N_1 needle domain is located at position (x_1, x_2). The parent domain has polarization $\mathbf{P}^1 = [0\ 1\ 0]^T p_0$ and needle N_1 has polarization $\mathbf{P}^{N_1} =$ [-1 0 0]$^T p_0$. However, N_2 has opposite polarization $\mathbf{P}^{N_2} = [1\ 0\ 0]^T p_0$ and consequently its effective line charge has opposite sign to that of N_1. What happens to the interaction between two perpendicular needle domains when N_2 is positioned around the fixed needle domain N_1?

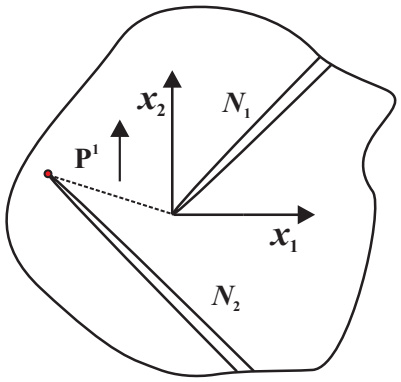


Figure 4.10: Schematic diagram of two perpendicular domains.

The extension force acting on needle N_2 is readily obtained from Eqs. 2.41 and 2.42, and a contour map is presented in figure 4.11. The position of zero extension force which occurs close to the x_1-axis is a stable equilibrium position: when the tip of the N_2 needle is perturbed away from an equilibrium position, the interaction force between the needle domains is a restoring force towards equilibrium. An approximate computation of the total energy of the configuration as a function of the extension of needle N_2 is shown in figure 4.12. The calculations were carried out with needles spaced a distance $10w$ apart along the x_1-axis and extension d is measured from the x_1 axis along the direction of [-1 1 0]. Figure 4.12 confirms the stability of the equilibrium position with respect to extensions of needle N_2. However, this

only gives a stable equilibrium assuming that N_1 is fixed. If, instead, the extension force on N_1 with fixed N_2 is calculated, it is found that there are again equilibrium positions close to the x_1-axis, but on a different line. The only intersection of these sets of equilibrium positions occurs when the two needle tips are coincident. However, when the needle tips lie on the x_1-axis the extension forces are extremely low and lattice friction may be sufficient to hold the needle domains in place.

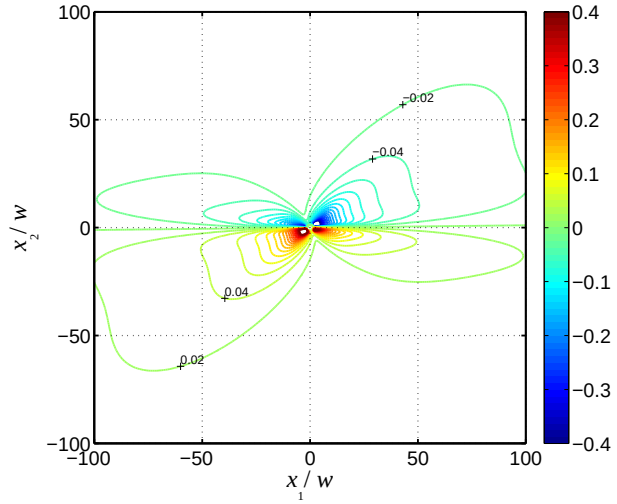


Figure 4.11: Contour map of extension force on N_2 domain for perpendicular needle domains.

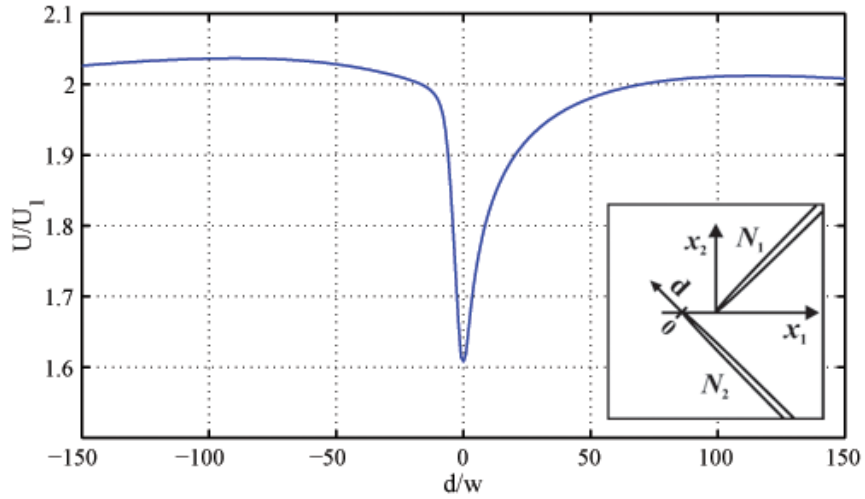


Figure 4.12: Energy variation with the changed length of N_2 domain

4.4.3 Opposite parallel domains

A similar analysis carried out on pairs of parallel needle domains with opposite tips also reveals a stable equilibrium. The configuration is shown in figure 4.13. Here the polarization states are $\mathbf{P}^1 = [0\ 1\ 0]^T p_0$, and $\mathbf{P}^{N_1} = \mathbf{P}^{N_2} = [\text{-}1\ 0\ 0]^T p_0$. The needle domain N_2 in this configuration has an effective dislocation with Burgers vector along $[\text{-}1\ \text{-}1\ 0]^T$ and a negative effective line charge. From figure 4.14, stable equilibrium positions for needle N_2 are found, close to the x_1 axis. In this case the stable equilibrium configuration for N_2 is also a stable equilibrium for N_1.

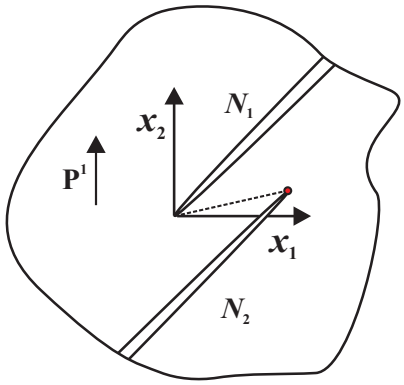


Figure 4.13: Schematic diagram of parallel needle domains with opposite tips.

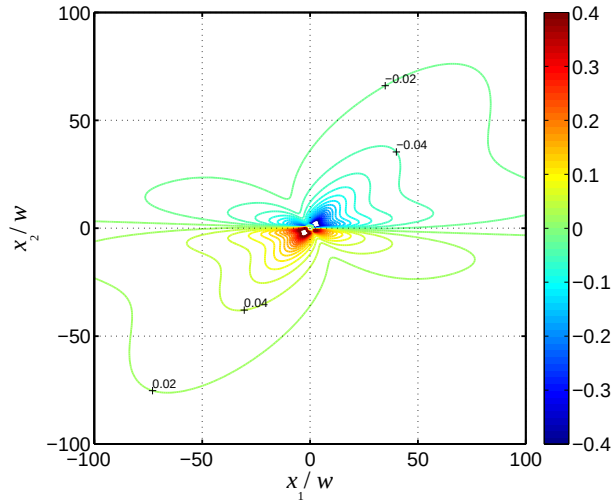


Figure 4.14: Contour map of extension force on N_2 domain for parallel needle domain with opposite tips.

In summary, the equilibrium configurations of pairs of needle domains in an infinite parent

domain were determined by finding configurations with zero force driving needle extension, or equivalently, minimum internal energy. Surprisingly, it is found that there is no equilibrium position for certain pairings of needle domains and this is attributed to the presence of effective line charges of the same sign. In contrast, pairs of needle domains with effective line charges of opposite sign exhibit stable equilibrium configurations. It can be concluded that in barium titanate the needle tip interactions are significantly affected by electrostatic terms.

4.5 Groups of needle domains

Groups of needle domains commonly occur in ferroelectric single crystals, formed by many needle domains in a certain pattern. The formation of group structures can be caused by the phase transition to the tetragonal phase when the $BaTiO_3$ crystals cool down through the Curie temperature. We have so far analysed the interaction of two needle domains and equilibrium distributions, with varying the position of the needle domain. The analysis will now be extended to group structures. The method of minimum potential energy will be adopted to explain why the needle domains exist in certain patterns.

4.5.1 Herringbone pattern of needle domains

Figure 4.15a shows herringbone-type patterns of needle domains observed by optical microscopy. Single crystal $BaTiO_3$ plates were obtained from Marketech International Inc. (USA). The crystal plates had thickness 0.5 mm and were provided in an unpoled state polished on both sides. Optical microscopy shows the domains due to changes in refractive index across domain walls. Similar observations were reported by Matsumoto $et\ al.$ [51].

Based on the above study about interaction between two perpendicular needle domains, the configuration shown in figure 4.16 was modelled to further analyse the herringbone-type pattern. The pattern domain with $\mathbf{P}^1 = [0\ 1\ 0]^T p_0$ is kept. Here, needle domains 1 & 2 have

the same effective dislocation with positive line charge, and spaced a distance $s = 10w$ along the x_1 axis direction. The needle domains 3 & 4 keeping the same spacing ($s = 10w$), are perpendicular to domains 1 & 2, and have negative effective line charge. The spacing s_m between needles 1 and 3 is half of the spacing s along the x_1 axis direction.

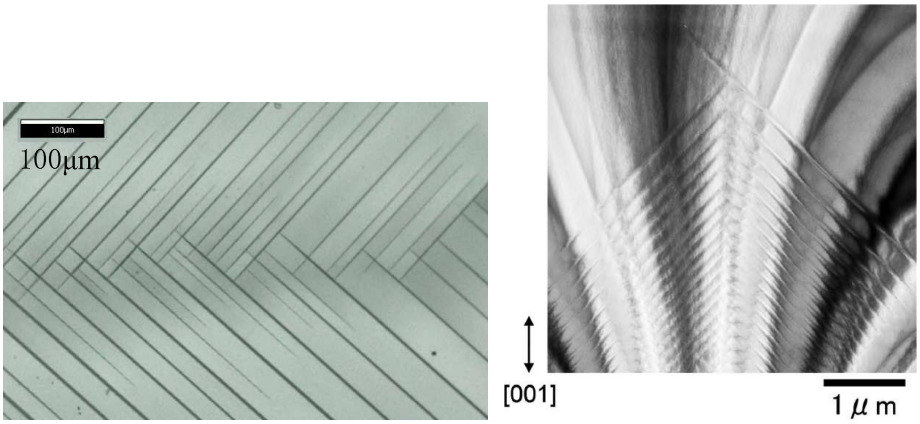


Figure 4.15: (a) A Herringbone type array of needle domains observed by optical microscopy in $BaTiO_3$ specimen with thickness of 1 mm; (b) Herringbone needle domains observed by TEM in thin film of $BaTiO_3$ with 300 nm [51].

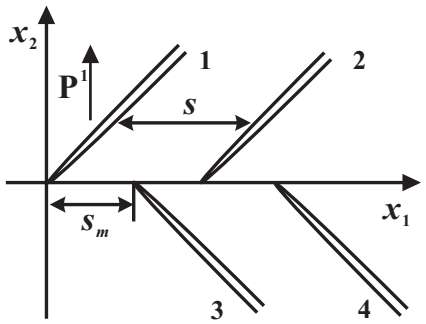


Figure 4.16: Schematic of a herringbone pattern of needle domains.

The stability of this structure was studied by computing the variation in internal energy resulting from changing the length of each needle domain independently by an amount d from the equilibrium position. As shown in figure 4.17, each needle tip is positioned in an energy well and the configuration is thus in a stable equilibrium. It is interesting to note, however, that the needles can be pulled out of a stable configuration with relatively small extensions or

retractions. In particular, the energy barrier to the escape of edge needles 1 by extension, or needle 4 by retraction is small, and a displacement of less than $20w$ can remove these needles from the stable configuration. Similar calculation on a longer pattern with 30 needles indicated that there is a low energy barrier to the escape of needles towards the end of the herringbone arrangement. The calculations appear consistent with the observed herringbone-type patterns found in $BaTiO_3$ single crystals. Additionally, it is found that the depth and width of energy potential well becomes deeper and wider as the herringbone pattern comprises more needle domains. This means that a structure with a longer herringbone pattern of more needles should be more stable from an energetic point of view.

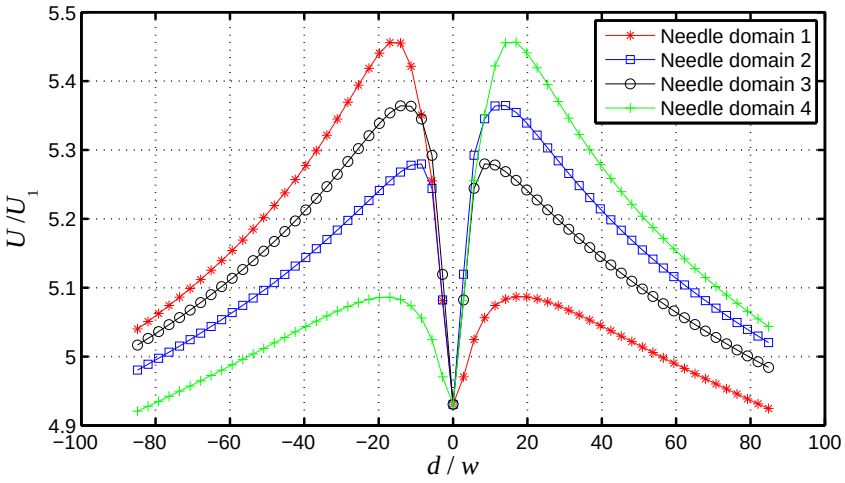


Figure 4.17: Energy variation due to change in length of needle domains in a herringbone-type pattern.

4.5.2 Comb-like needle domains with identical tips

Combs of needle domains with identical tips are also characteristic of barium titanate single crystals. However, the study of pairs of needle domains with identical tips suggests that there is no stable equilibrium configuration. This problem is considered further by modelling comb-like arrays of needle domains. For illustration, an array of four needle domains is shown in figure 4.18. In figure 4.19, each needle is close to a maximum energy position when the needle tips lie along the x_1 axis.

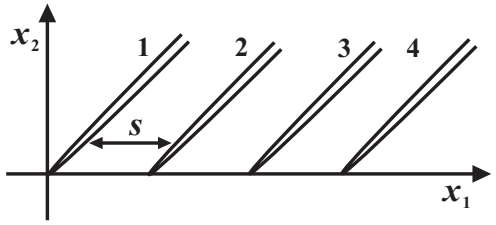


Figure 4.18: Schematic diagram of comb of needle domains with identical tips.

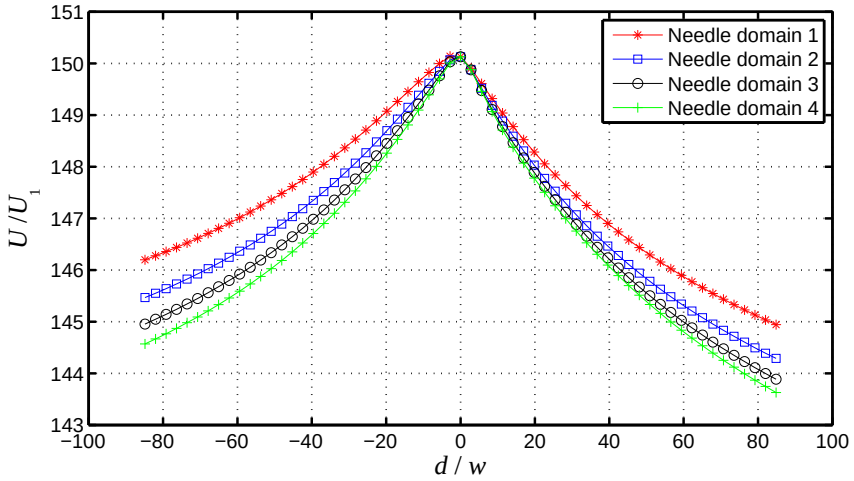


Figure 4.19: Energy variation due to change in length of needle domains in a comb-like pattern.

Consequently, the model of needle domains as an effective dislocation and line charge in an infinite medium does not account for the existence of comb-like arrays of 90° a-a needle domains. Since the electrostatic terms appear to dominate the interaction of nearby needles, the comb of similar needles produces fields equivalent to a charged layer along the edge of the comb, with high energy. In the herringbone-type pattern, the presence of alternating effective charges reduces the overall energy resulting in a stable configuration. To account for the existence of stable comb-like structures, some combination of screening space charge, lattice friction and boundary conditions is needed as an additional ingredient in the model. Therefore, we will first discuss the effect of varying the polarization charge equivalent to allowing screening, on the stability of comb-like structure in the next section.

4.6 The effect of polarization charge on stability

The above paradoxical results lead us to pay more attention to the effect of charge produced by the polarization jump at a needle tip on domains interaction. In section 4.4, the results indicate that the electrostatic terms appear to dominate the interaction of nearby needles. But this was based on the assumption of perfectly insulating behaviour. In fact $BaTiO_3$ is a semiconductor, and the strong electric fields near a needle tip many promote conduction in a region near the tip. The polarization charge would then be reduced and may then produce a new equilibrium. Forsbergh [12] also observed that a surface polarization charge existing at needle domain tip could be neutralized by electric conduction.

The following work focuses on studying the interaction of pairs of needle domains with identical tips, when polarization charge is varied in the range $Q = 0$ to $\sqrt{2}p_0w$. Other simulation conditions are kept the same as section 4.4.1. From the results, it is found that the existence and position of stable equilibrium states are very sensitive to a change in the quantity of polarization charge. There is no stable equilibrium configuration until the polarization charge is reduced to 73.4% of the full theoretical value $q = \sqrt{2}p_0w$. In figure 4.20, the relation of the stable equilibrium position to the reducing charge is described. The vertical coordinate θ indicates the angle between the stable equilibrium line and the x_1 axis negative direction. This angle varies in the range between 44.5° and 58.6°. In addition, figure 4.21 presents selected contour maps of extension force with reducing polarization charge for a pair of parallel needles. For the two cases of full charge $Q = q$ and $Q = 0.8q$, there is no stable equilibrium position for pair of needle domains with identical tips. The reason may be that the electrostatic force is still strong enough for the needle tips to repel each other. When the polarization charge reduces further, a stable equilibrium position appears, as shown in figures 4.21c-4.21f. The stable equilibrium positions are labelled 'SS' and angle θ is about 45° at minimum.

Based on the above analysis of the sensitivity of the equilibrium configuration to polarization charge, the total energy of two parallel needle domains in equilibrium state is calculated

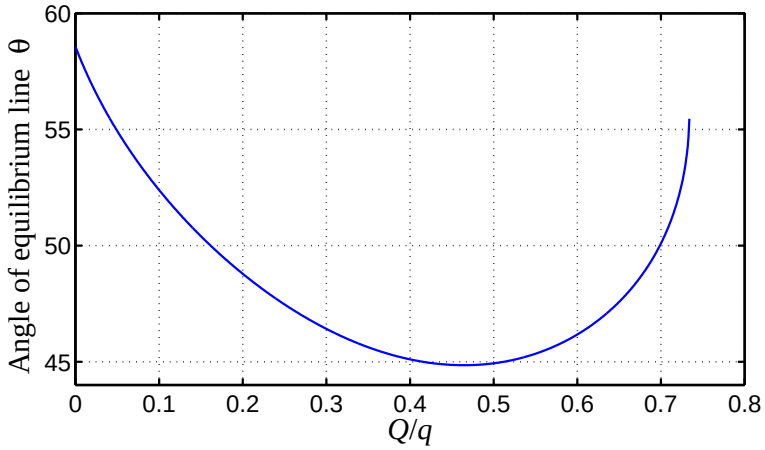
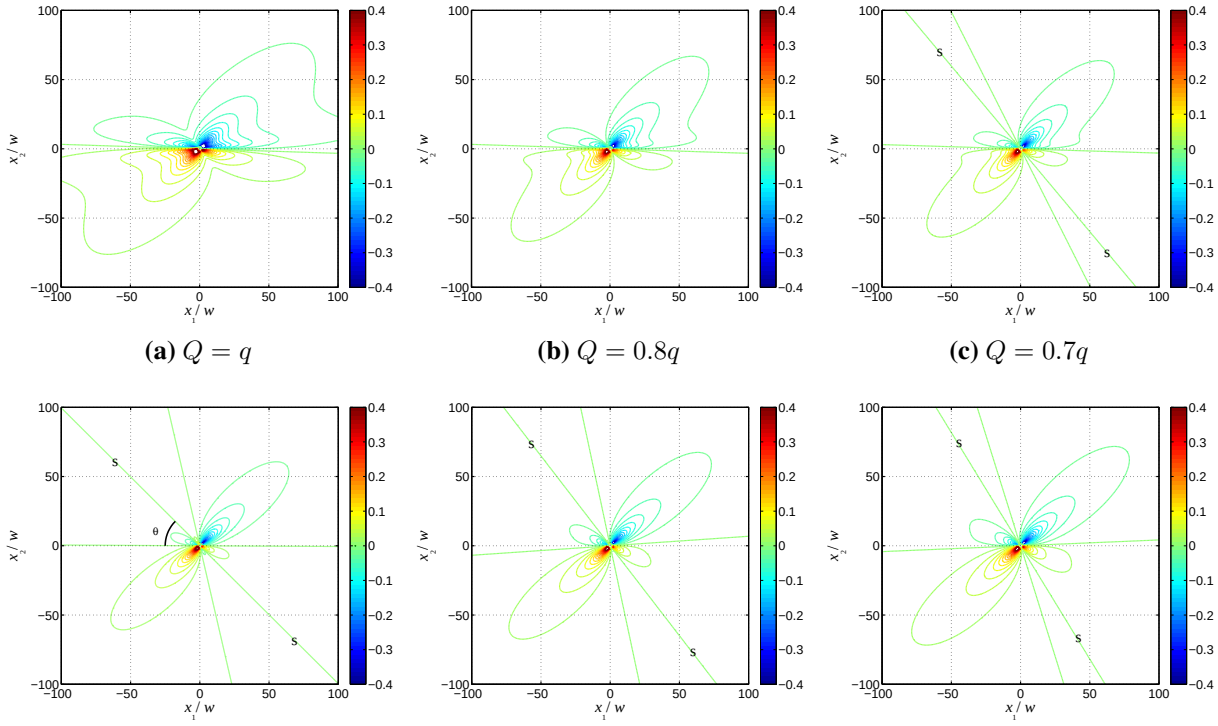


Figure 4.20: Variation of the stable equilibrium position with changing the polarization charge.



(a) $Q = q$ **(b)** $Q = 0.8q$ **(c)** $Q = 0.7q$

(d) $Q = 0.48q$ **(e)** $Q = 0.1q$ **(f)** $Q = 0$

Figure 4.21: Contour map of extensions force on N_2 domains for two parallel domains with identical tips as varying the change of polarization charge.

for varying polarization charge. It is expected that a stable configuration with minimum energy over all values of Q can be obtained. The internal energies U are computed over a square region of side $200w$ without the core region ($2w \times 2w$). The needle domain N_1 is fixed at the center of the calculated region. The similar needle domain N_2 with spacing $10w$ away from N_1 along

the x_1 axis is placed at the corresponding equilibrium position taken from in figure 4.20, with polarization charge in the range 0 to $0.734q$. In addition, the total internal energy is normalized by the reference energy U_f which is produced by the needle domains with full polarization charge q and is computed over the same region ($200w \times 200w$) without the same core region ($2w \times 2w$).

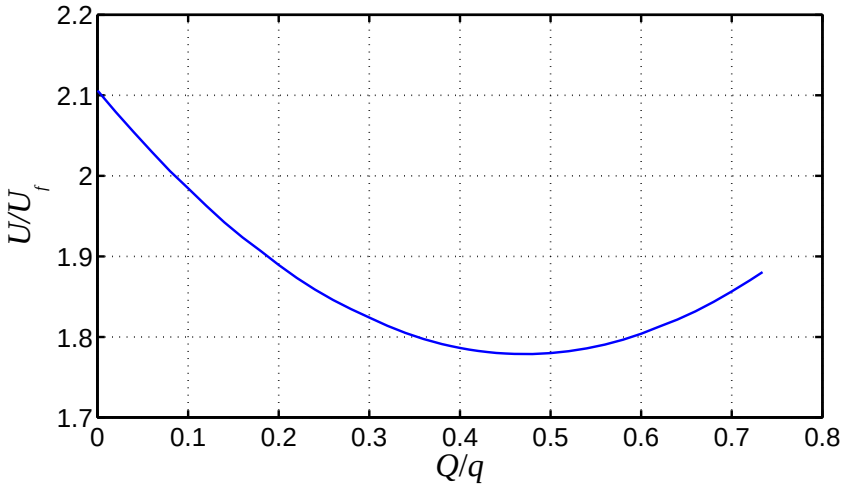


Figure 4.22: Variation of the total internal energy with changing the polarization charge.

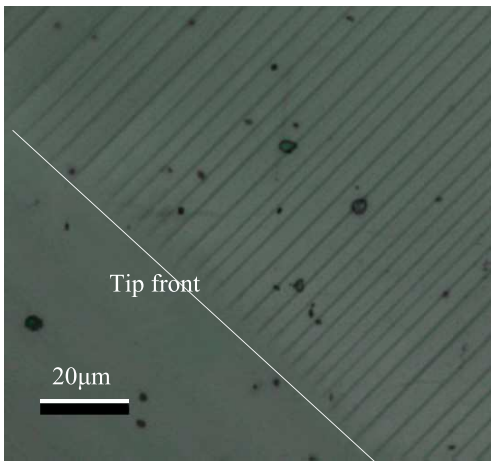


Figure 4.23: The comb-like needle domains observed by optical method.

Figure 4.22 displays the relation of the internal energy due to two interactive needle domains in the equilibrium state to the changing polarization charge. We are at first surprised to find that the energy generated by two interactive needle domains without polarization charge

can be greater than twice the energy of an individual needle domain with full polarization charge. The internal energy firstly decreases as the polarization charge is varying from 0 to $0.48q$. When the polarization charge increases over $0.085q$, the energy begins to be less than that of two individual needle domain with full polarization charge, namely $2U_f$. With continually rising polarization charge, to $0.734q$, the internal energy starts to increase. But the energy is still less than $2U_f$. Consequently, the internal energy has a minimum as the polarization charge increases from 0 to $0.734q$. It is expected that the configuration with minimum energy is most stable, and this leads to a polarization charge and angle θ of $0.48q$ and $44.9°$, respectively. It is natural to interpret that as consistent with the domain tips fronts seen in experiment observation, which are perpendicular to the needles' longitude direction, as shown in figure 4.23.

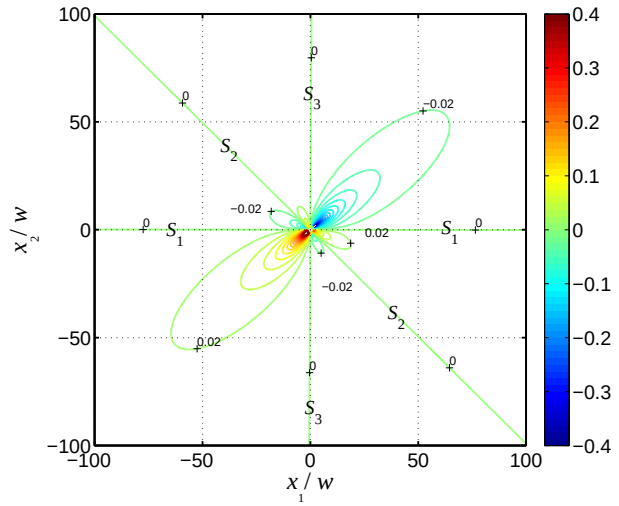


Figure 4.24: Contour map of extension force on N_2 which is perpendicular to the needle N_1 for the reduced polarization charge $Q = 0.48q$.

What happens to the interaction of two perpendicular needle domains, when the polarization charge existing in the needle tip is reduced to $0.48q$? Figure 4.24 presents the contour map of extension force on the needle N_2 which is perpendicular to the needle N_1. There are three lines marked as S_1S_1, S_2S_2, and S_3S_3 for equilibrium position in the result of interaction of two perpendicular needle domains. One of them S_2S_2 is really interesting, which is the equilibrium line oriented at $45°$ to the negative direction of x_1 axis. Equivalently, if the tips of two perpen-

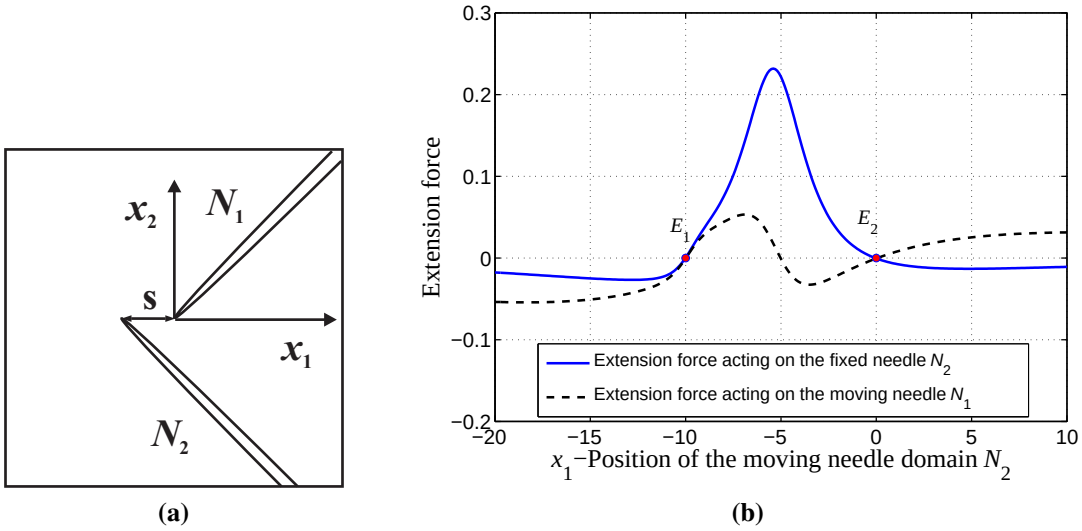


Figure 4.25: Interaction between of two perpendicular needle domains (a) Schematic of two perpendicular needle domains with the spacing $s = 10w$; (b) the extension force acting on each needle domain.

dicular needles or the extension lines of two needle tips along their own longitudinal direction are coincide at the origin position, the two perpendicular needles (whatever the distance of the two tips) are always in a stable equilibrium state. However, the situation is quite different when the extension lines of two needle tips along their own longitudinal direction do not coincide at the origin position. First, we find that the equilibrium line S_3S_3 at the x_2 axis is an unstable line. Once any perturbation causes the needle N_2 to extend or shorten, the interaction force due to two perpendicular needles will make the needle tip situated at the line S_3S_3 move away from this unstable equilibrium position. However, the equilibrium line S_1S_1 which lies at the x_1 axis is a stable equilibrium position. The interaction force is a restoring force to constrain the needle tip at this equilibrium position. To illustrate this, we choose two perpendicular needle domains with charge $Q = 0.48q$ and the spacing $s = 10w$, as shown in figure 4.25a. The needle N_2 changes its length in the range from position $(-20w,\ 10w)$ to position $(10w,\ -20w)$, while the needle N_1 is fixed at the origin. During the process of movement, the needle N_2 passes through two equilibrium lines S_1S_1 and S_3S_3. The extension force acting on each needle domain is presented in figure 4.25b. The intersection E_1 is situated at the equilibrium line S_1S_1, and the

intersection E_2 is at the equilibrium line S_3S_3. When the needle N_2 situated at E_1 tries to extend under external perturbation, the negative extension force will act on this needle to drive it back to the equilibrium position E_1. From the extension force produced by the needle N_2, if the needle N_1 is not fixed, it also has a trend to keep to the line parallel to the x_1 axis when needle N_2 starts to move away from the position E_1. Therefore, from this figure, we can easily understand that the position E_1 is a stable equilibrium position. This stable equilibrium position is consistent with the case of two interactive perpendicular needles with full polarization charge. Therefore, even though the polarization charge in needle tip is reduced to $0.48q$, this does not influence the stability of the herringbone needle domains.

4.7 A needle domain detached from the comb

What happens if a needle domain tip becomes detached from the tip fronts of a stable comb? Using the above results, the polarization charge existing at the needle domain tip is taken as $Q = 0.48q$ in the following analysis. Based on the contour map of interaction force between two parallel needle domains shown in figure 4.21d, the behaviour of a needle domain detached from the tip fronts is discussed. For convenience, the equilibrium positions shown in figure 4.21d are presented in figure 4.26a. The line l_0 which is oriented at 44.9° to the x_1 negative direction provides a set of stable equilibrium positions. However, the other two lines l_1 and l_2 located at the x_1 axis and 33° (angle β) to the line l_0 are unstable equilibrium positions. In addition, the line $l_{2'}$ is obtained by the reflection of the line l_2 with respect to the stable equilibrium line l_0; this will be used to explain the interaction of the detached needle domain with other nearby needles.

A comb-like configuration consisting of five identical needle domains is selected to analyse the behaviour of the detached needle domain N_0, as shown in figure 4.26b. Firstly, consider the interaction between the neighboring needle domains N_0 and N_1. To utilize the contour map

shown in figure 4.21d, the needle N_1 is taken as the needle fixed at the origin. And then the influence of the detached needle under the fields due to the needle domain N_1 is discussed. The original position 0 is marked in figure 4.26b, which is situated at the line of stable tip fronts l_0. If needle N_0 starts to extend and detach from its equilibrium position 0 under the action of an external load, the detached needle domain is captured back to origin position 0 if the new position of the extensional tip is not beyond the position 1. Once the displaced tip N_0 goes beyond the position 1, the detached needle domain will become free of needle N_1. Likewise, interaction between the fixed needle N_{-1} and the detached needle N_0 is discussed. The critical position is now on $l_{2'}^{-1}$. The line l_2^1 intersects the line $l_{2'}^{-1}$ at the position 1, illustrated in figure 4.26b. By such analogy, when we consider the effect of each individual needle (N_2 & N_{-2}) on the detached needle N_0, the critical position is position 2. If the detached needle within the range between position 0 and position 2, the force acting on the detached needle N_0 from the both needles of N_2 and N_{-2} is a restoring force provided. However, we have known that the detached needle beyond position 1 has broken free of needle N_1 and N_{-1}. Therefore, Considering the configuration symmetry and superposition of forces, the critical position for this detached needle should appear in the range between position 1 and position 2. By such analogy, the longer comb has a larger range between the original position 0 and critical position for the detached needle domain. Figure 4.27 presents the corresponding evidence through comparing the extension force on a detached needle for a short comb and a longer comb. This figure shows the extension force of the detached needle N_0 under the effect of the whole comb which comprises of 5 and 51 needles, respectively. For the 5-needles comb which is the same as the schematic comb shown in Figure 4.26b, the critical position C marked in figure 4.27 is confirmed within the range between position 1 and position 2. When the needle domain tip is detached beyond the critical position C, the positive extension force provided by the whole comb acts on the detached needle pushing it away from the tip fronts of the comb. Finally, this detached needle escapes from the constraint of the tip front. Additionally, we find that as the central needle detaches from the tip front of the comb, the restoring force provided by a longer comb acting

on this detached needle is greater than that of a short one. Therefore, we can conclude that the longer comb is more stable to restrain the needle tips along the stable equilibrium position l_0. Keeping the above analysis in mind, the case of N_0 shortening and detaching is symmetric with respect to the stable equilibrium line l_0.

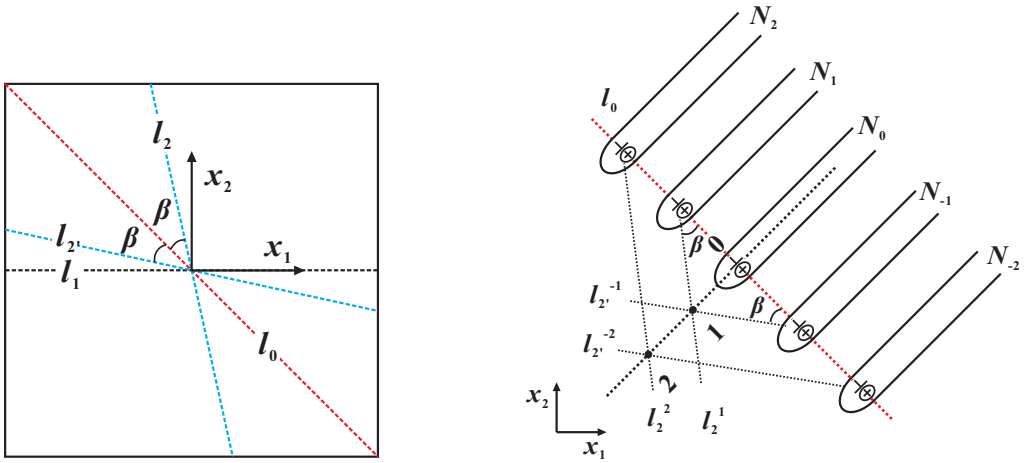


Figure 4.26: (a) Outline of equilibrium position and its reflected line in order to explain the interaction of detached needle with the whole comb, (b)Interaction of parallel needle domains on the detached needle domain

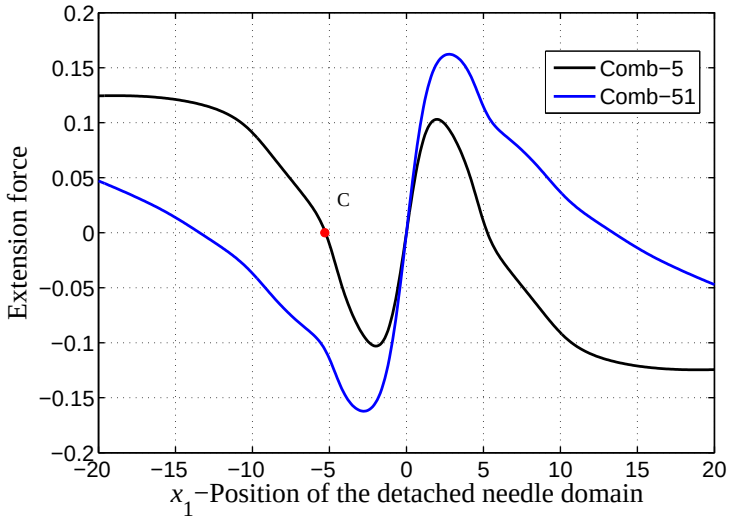


Figure 4.27: The detached needle acted by longer and shorter comb.

4.8 Influence of external perturbation on groups of needle domains

In section 4.7, a needle domain detached from the tip front of a comb-like pattern was analysed. In practice, the more likely situation is that groups of needle domains exist with tips in various positions. What will happen to them? To analyse this problem a simple model for the evolution of needle domain patterns is developed.

4.8.1 Viscous model for the motion of needle domains

During analysis of the motion of interactive needle domains, we adopt a viscous model to link the tip velocity with the driving force for extension of the needle domain. We already know the interaction force calculated by Eq. 2.41. The resultant force acting on the needle domain is found by superposing the interaction force due to the effect all other needles excluding itself. A simple model can be developed by assuming linear kinetics. Similar methods have been used for simulating dislocation dynamics [94]. The moving velocity ν of the needle domain is computed as follows,

$$\nu = \eta F \tag{4.4}$$

where, η is a positive viscosity term. F is the resultant extension force acting on the moving needle domain. If instead, lattice friction is considered for the moving needle domains, the relation of velocity ν to the acting force F could be as shown in figure 4.28a. If $F > F_{cr}$, where F_{cr} is the value of the lattice friction, the needle domain extends. If $F < -F_{cr}$, the needle domain shortens. Only $|F| \leq F_{cr}$, the needle domain will stop (velocity $\nu = 0$). The lattice friction will be considered further in later discussion. When we do not consider the effect of lattice friction on the motion of needle domains, the linear relation of Eq. 4.4 can be used, see figure 4.28b. In this chapter, we consider this ideal case without friction.

During the analysis of evolution for needle domains, we assume the quasi-static process for the moving needle domains. Therefore, in the simulation, the viscous law is transformed as follows:

$$s_d = \eta F \tag{4.5}$$

where, s_d is the moving distance corresponding to force F at the same unit time. Additionally, the value of viscous coefficient η determines the moving step length under the action of the same force. To find the equilibrium configuration, a sufficiently small viscous coefficient is required to approach the equilibrium position and get the convergent results. However, when the dynamic behaviour of needle domains under external loading is investigated, the value of viscous coefficient is obtained from the experiment through measuring velocity and the acted force of needle domain.

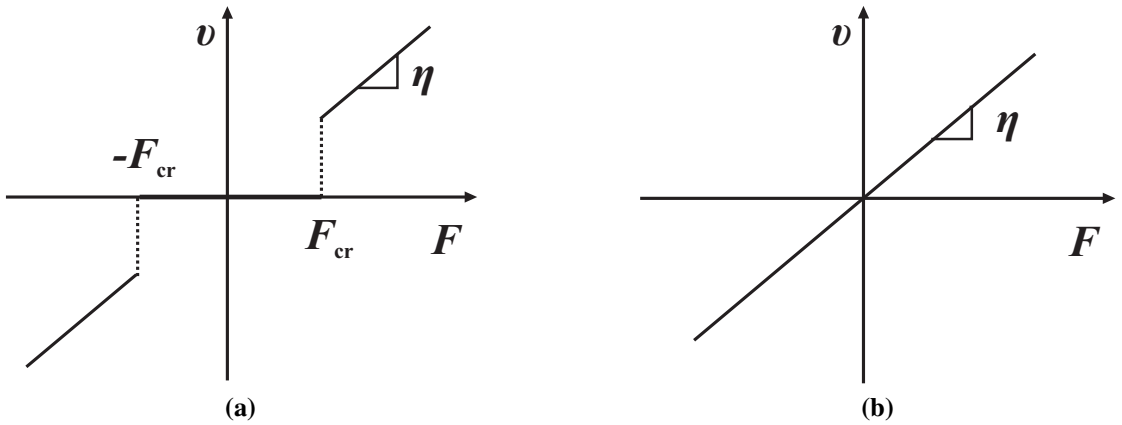


Figure 4.28: The relation of velocity to the acting force on needle domain (a) Friction $= F_{cr}$, (b) No friction

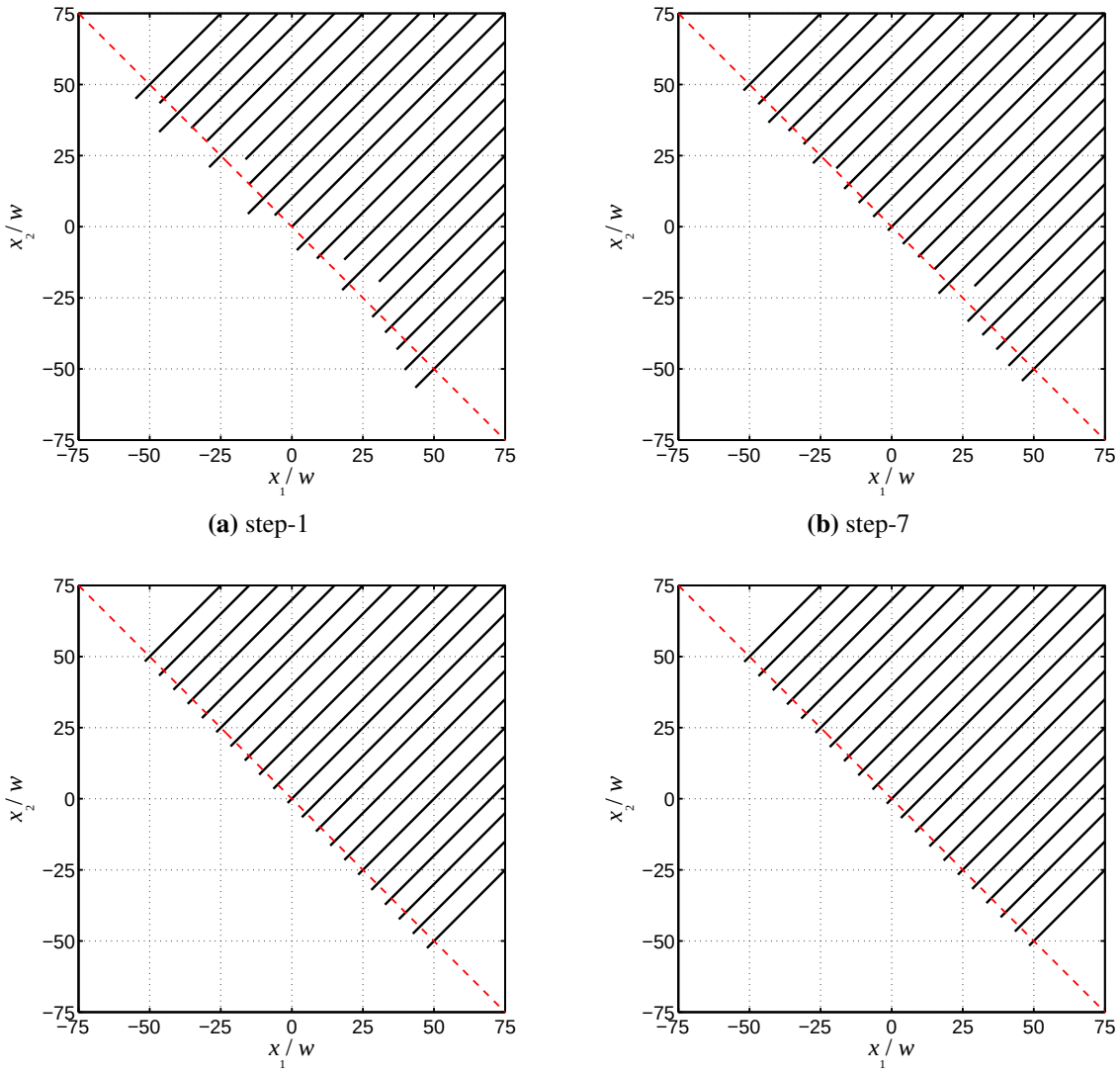
4.8.2 Comb of needles with a small perturbation

In the section 4.7, detaching one needle from a comb-like pattern was considered. It was found that the detached needle domain experiences a restoring force over a limited range of perturbation. In this section, we will analyse the motion of needles in a comb-like pattern under small

perturbation.

An array of comb-like needle domains comprising 21 needle domains is studied. Their tips are located on the line orientated at 45° to the negative x_1 axis. The spacing of needle domains is still kept as $10w$ along the x_1 direction. The equivalent polarization charge at each needle tip is set equal to $0.48q$. When the comb-like needle domains suffer a small perturbation, their tips experience extensional force. In the simulation process, a random position is given to each needle tip, in the range $(-10w/\sqrt{2}, +10w/\sqrt{2})$ along the longitude direction for each needle domain, namely within the angular range of 2β mentioned in section 4.7. The relative position of each needle tip pair can be calculated and used to obtain the extension force on each needle by superposition. Then the velocity of each needle tip is computed by the linear viscous model mentioned in section 4.8.1. Next, we update every tip position according to the distance moved in a small, fixed time increment. This is repeated until the interaction force becomes zero, and the motion of the needle domains will then stop in an equilibrium state. During the evolution, a sufficiently small viscosity coefficient η is required to avoid the problem of no convergence. Combining the computing time with the data convergence, the normalized viscosity coefficient $\eta_0 = 7 \times 10^4$ (w/σ_0) is adopted in simulation for per unit time to achieve the accuracy of 1×10^{-8}.

Figure 4.29 presents the evolution of an array of 21 comb-like needle domains under the influence of a small random perturbation. The dotted line is located at $x_2 = -x_1$ where the stable original position of tip fronts without any perturbation is. Initially, the needle tips are displaced from the stable line by varying degrees, as shown in figure 4.29a. The process of changes in tip positions is displayed in figures 4.29a-4.29d. We found that the detached needle domains experience fast moving at early steps and sluggishly approaching to the equilibrium position at later steps (after step-20). The reason is that the value of the restoring force resulting from interaction among the needle domains becomes small gradually when the needle domains are approaching to the equilibrium configuration. The tip line of final equilibrium configura-



(a) step-1

(b) step-7

(c) step-20

(d) step-125

Figure 4.29: The evolution of the detached needle tips under small perturbation

tion shown in figure 4.29d moves slightly relative to original position (red dashed line). This simulation result suggests that the structure of the comb-like needle domains is stable to small perturbations. A consistent conclusion is obtained from repeating the test (20 times) with different random starting conditions. The common conclusion from repeating work is that comb of needles with a small perturbation will snap back to a new equilibrium position and the tip line of final equilibrium configuration still keeps $45°$ to the negative direction of x^1 axis. However, the comb with different random starting conditions experiences the different the process

of evolution back to the comb pattern with 45° tip line.

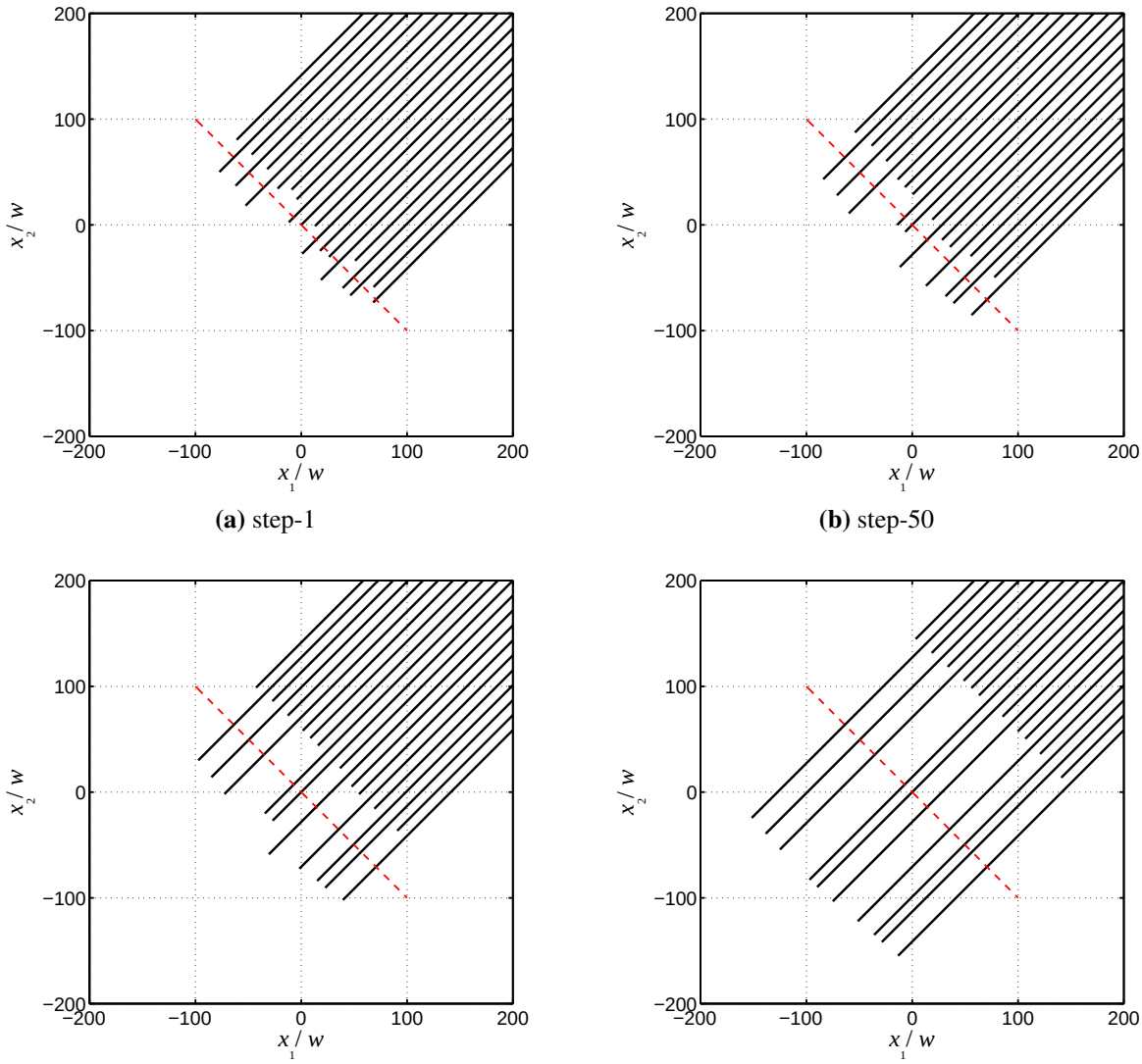
4.8.3 Comb of needles with a large perturbation

In section 4.8.2, it was found that a comb of needle domains has stability to small perturbations. If the comb-like needle domains experience a large perturbation, what will happen?

During the process of simulation, the calculation conditions are kept the same as in section 4.8.2, except that the initial position of each tip is within a large random range $[-20w/\sqrt{2}, +20w/\sqrt{2}]$. The linear viscous model is used as before.

Figure 4.30 presents the motion of the comb-like needle domains after the large perturbation. The dotted line is located at $x_2 = -x_1$ and figure 4.30a shows the initial position of the needle tips. It is found that the detached needle tips do not return to the unperturbed position, as shown in figures 4.30a-4.30d. Interestingly, the new tip fronts appear to align along 45° lines, with some shortening needle tips and some extending needle tips. As displayed in figure 4.30d, the detached needles with a large perturbation develop to two detached combs whose tip fronts become 'free' and are far away each other. In practice, the lattice friction will pin two new tip fronts within crystals before the detached needles become completely free. This appears consistent with experimental observations by Potnis and Huber [52] where a fine comb of needles is seen, with some detached needles aligned in a coarser array, see figure 4.31.

We have studied the influence of external perturbation on groups of needle domains. The conclusions suggest that the configuration of the comb-like needle domains have ability to resist to small perturbations. However, the comb-like needle pattern under the effect of a large perturbation does not snap back to a perfect arrangement and finally develops to dual comb structure. In future work, we will further identify critical value for a comb with two families of needle lengths with varying number of comb needle domains and spacing of needle domains in comb-like pattern. This critical value can be used to estimate the stability of comb-like needle domains.



(a) step-1 **(b)** step-50

(c) step-80 **(d)** step-150

Figure 4.30: The evolution of the detached needle tips under strong perturbation

4.9 Domain bundle boundaries in a $BaTiO_3$ single crystal

In this section, we will introduce another type of structure consisting of $90°$ a-a needle domains to further test the model of needle domains. First, we study the interaction between two parallel needle domains with opposite tips, as shown in figure 4.32. The polarization direction of the two needle domains (N_1&N_2), which are $90°$ a-a needle domains, is along [1 0 0] and [-1 0 0], respectively. The polarization direction of parent domains (P_1&P_2) whose intersection is separated by $180°$ domain wall is [0 -1 0] and [0 1 0], respectively. The tip of N_1 needle is

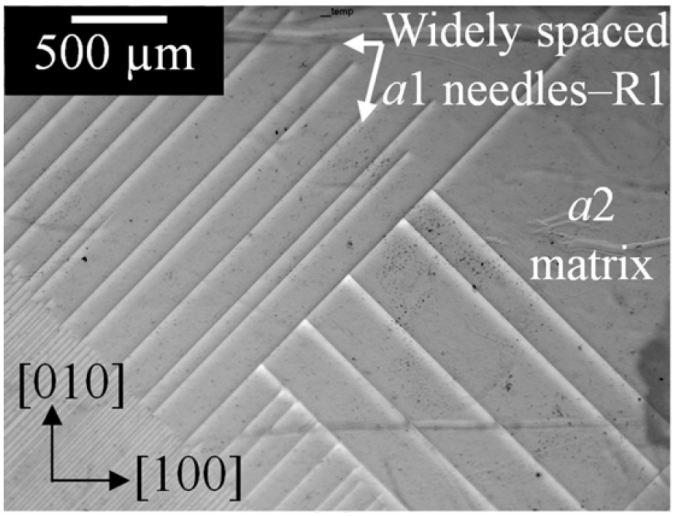


Figure 4.31: The comb needles with two detached tip fronts [52].

located at the origin, and the needle N_2 can move relative to N_1. Both needles are at $45°$ to the x_1 axis. According to the modelling in section 2.3, the field of the needle N_1 is equivalent to that of an effective edge dislocation $\mathbf{b}_1 = (3\sqrt{2}\varepsilon_0 w/2)[1\ 1\ 0\ 0]$ with a negative line charge $\mathbf{q}_1 = -\sqrt{2}p_0 w[0\ 0\ 0\ 1]$. Correspondingly, the needle N_2 is approximated by an edge dislocation $\mathbf{b}_2 = 3\sqrt{2}\varepsilon_0 w/2$[-1 -1 0 0] with $\mathbf{q}_2 = -\sqrt{2}p_0 w[0\ 0\ 0\ 1]$. The model in section 2.3 was based on have a uniform parent domain, but here the parent domain is in two pieces with opposite polarization. This difference causes the change in the material constants for the parent domains with the different polarization direction. In fact, the opposite polarizations of parent domains only affect piezoelectric constants and the elastic and dielectric constants keep the same. As before $Q = 0.48q$ is used here.

After introducing the needle N_2 to the field generated by the needle N_1, interaction between of them is calculated using Eqs. 2.41 and 2.42. A region of $100w \times 100w$ is considered, and the corresponding contour map of extension force on N_2 is presented in figure 4.33a. Three equilibrium lines a,b and c are found in this figure. The lines a and c are the location of stable equilibrium states for needle N_2. Taking an example of two needle domains with spacing $20w$ along the x_1 direction, the extension force on the moving needle N_2 along its longitude direction is presented in figure 4.33b as a function of the x_1 coordinate of the tip of N_2. The

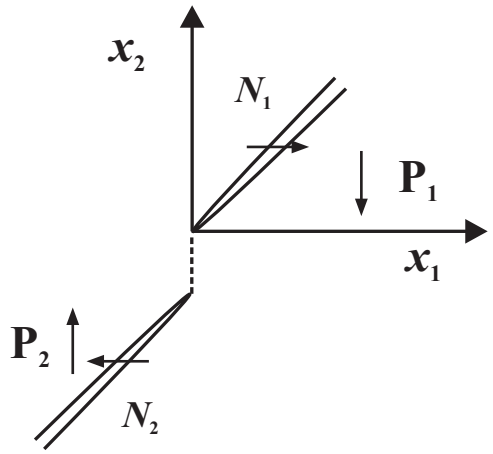
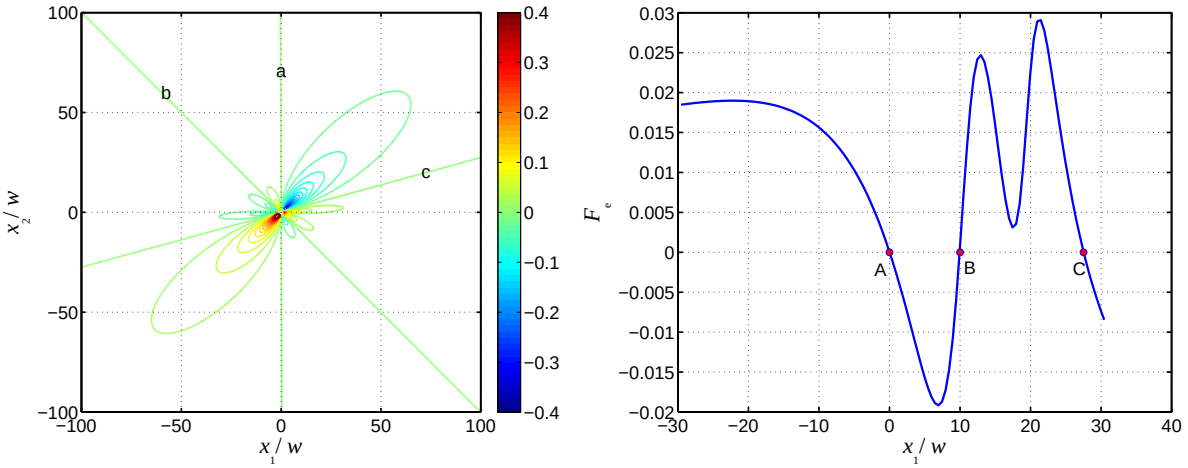


Figure 4.32: A pair of parallel needle domains with opposite tip

moving range of needle tip (N_2) is from $(-30w, -50w)$ to $(30w, 10w)$. In figure 4.33b, three zero-crossover points are marked by A, B, and C on the x_1 axis. The points A and C (which belong to the line a and c respectively) are the stable equilibrium points. However, location B is an unstable equilibrium position. It means the needle tip will not keep on this position once the needle experiences an external perturbation.



(a) **(b)**

Figure 4.33: (a) Contour map of extension force on needle N_2; (b) extension force acting on needle N_2 moving along the line $x_2 = x_1 - 20w$.

What will happen to a domain bundle composed of needle domains with opposite tips and opposite parent polarization domain? Is the arrangement of this domain bundle in equilibrium?

Here, we choose one group of needle domains having six needle domains to dynamically search for a stable equilibrium pattern. Its initial arrangement is given schematically in figure 4.34a. In this pattern, two comb-like needle domains with opposite tips are staggered and keeping the same spacing $5w$ along the x_1 direction between each needle. The tips of needles N_1, N_2, N_3 are on the line $x_2 = -x_1$, while the tips of needles N_4, N_5, N_6 are on the line $x_2 = -x_1 - 5w$. The viscous model of section 4.8.1 is adopted to move each needle tip according to the extension force acting on each needle. Finally, we obtain an equilibrium pattern that is close to the initial arrangement, as shown in figure 4.34b. A straight line is used to represent each needle in the simulation result 4.34b. Comparing initial position, only a small tip displacement happens to each needle. The tip line of needle domains in the equilibrium pattern has a zigzag shape.

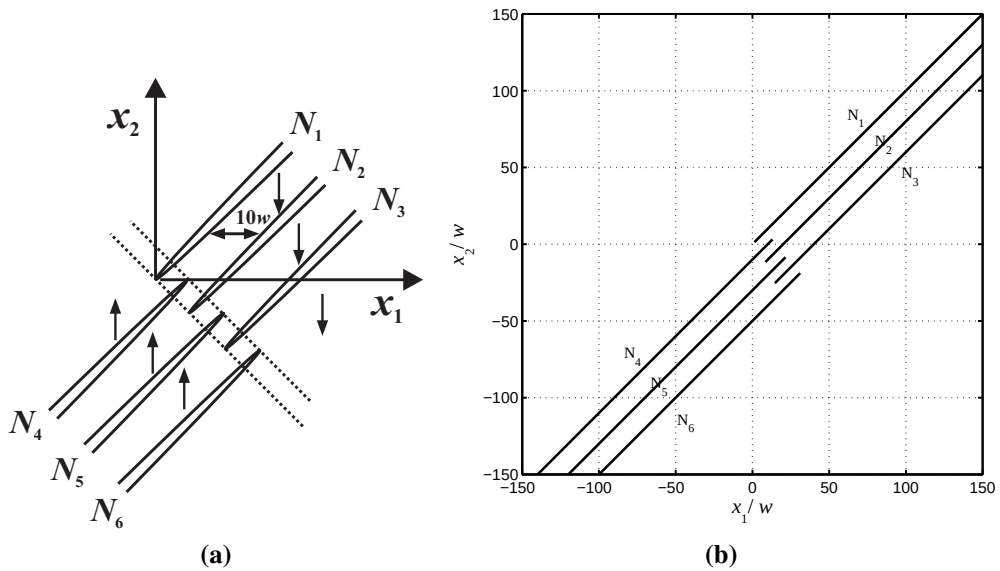


Figure 4.34: (a) Staggered arrangement of needle domains with opposite tips; (b) equilibrium pattern of needle domains obtained using dislocation method.

Experimental observation of domain bundle boundaries in $BaTiO_3$ single crystals was studied by McGilly [95] using both piezoresponse force microscopy (PFM) and scanning transmission electron microscopy (STEM), as given in figure 4.35. In this figure, it is also found that the needle domains with the opposite tips can exist in a staggered pattern in a $BaTiO_3$ single crystal. Additionally, the zigzag bundle boundary composed of local 180° domain walls is

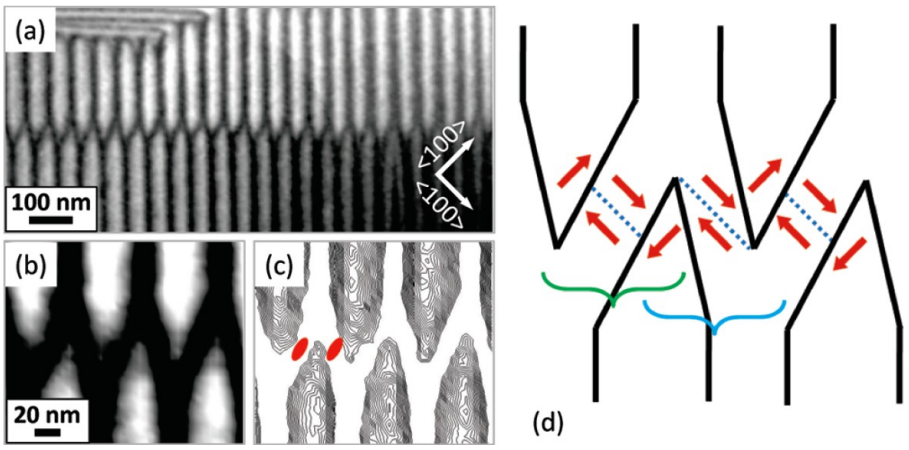


Figure 4.35: STEM images showing two parallel sets of 90° domain bundle and a bundle boundary [95]

found. This observed result is consistent with the simulation result of figure 4.34b. Topological information from STEM shows domain bundle boundaries can support chains of dipole flux closure and quadrupole nanostructures. This kind of boundary can exist in a single crystal, but it is comparatively rare. In the simulation, when a small displacement perturbation disturbs the needle tip away from equilibrium, we find that the equilibrium arrangement is restored, hence it is stable. However, strong perturbation will cause needle tips to escape and grow continually. In this case, part of the needle bundle extends, while another part will shorten, resulting in the needle tips leaving the initial equilibrium position. In conclusion, the dislocation and line charge model of needle domains works well to explain and analyse the fields and interaction of needle bundle domains.

4.10 Estimation of friction F_{cr}

The generation of needle domains is due to non-uniform stress field which induces the polarization switching of a partial domains. The source of non-uniform stress field could be uneven temperature change, and non-uniform mechanical and electrical loading. As stated in section 3.1.2, Cooling through Curie temperature and three-point bending are usually used to generate needle domains in the experiment. Firstly, certain intensive field existing at the boundary or the

crack front actives the domain switching. As the domain switching further develops into crystal interior until stop under the resistance effect of lattice friction. Finally, the needle domains are formed.

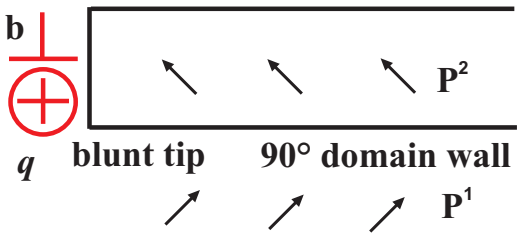


Figure 4.36: The blunt needle tip modelled as the coupling fields of an effective dislocation **b** and line charge q.

In this section, we will discuss how to estimate the resistance to the polarization switching at the needle tip or the development of needle domain, based on the shape of a needle domain model in equilibrium, considering the field due to an assembly of edge dislocations and line charges. And a model with lattice friction, as indicated in figure 4.28a, is also considered. In section 2.3, we adopt an effective dislocation **b** and line charge q to model the field produced by a blunt needle, as given in figure 4.36. This simplified model facilities the study of interaction of needle domains. However, in practice, the needle domain tip is not blunt. The needle domain tip, as the local source of stress and electric fields, can be represented by a set of discrete dislocations b_s coupled with line charge q_s spread over the needle tip. Summation of b_s and q_s over the needle tip is equal to the effective dislocation b and charge q. The growth and movement of needle domains can be treated as the result caused by the interaction of the equivalent dislocations and charges. When the balance among these dislocations and charges distributed over the needle tip is broken under the action of external loads (e.g., mechanical, electric, and thermal loads), the needle domain will extend or shorten to adjust forces among these discrete dislocations and achieve new balance. There should be friction to balance the repellent forces among the group of dislocations and charges over needle tip. Their balance will influence the development of needle domain (extension and shortening) and the configuration of the needle tip including the length L and the opening angle θ, as illustrated in figure 4.37a. Since we know the needle width

w, the needle length, L and the opening angle θ through experimental measurement, we can calculate the friction F_{cr} according to the theory of a dislocation pile-up.

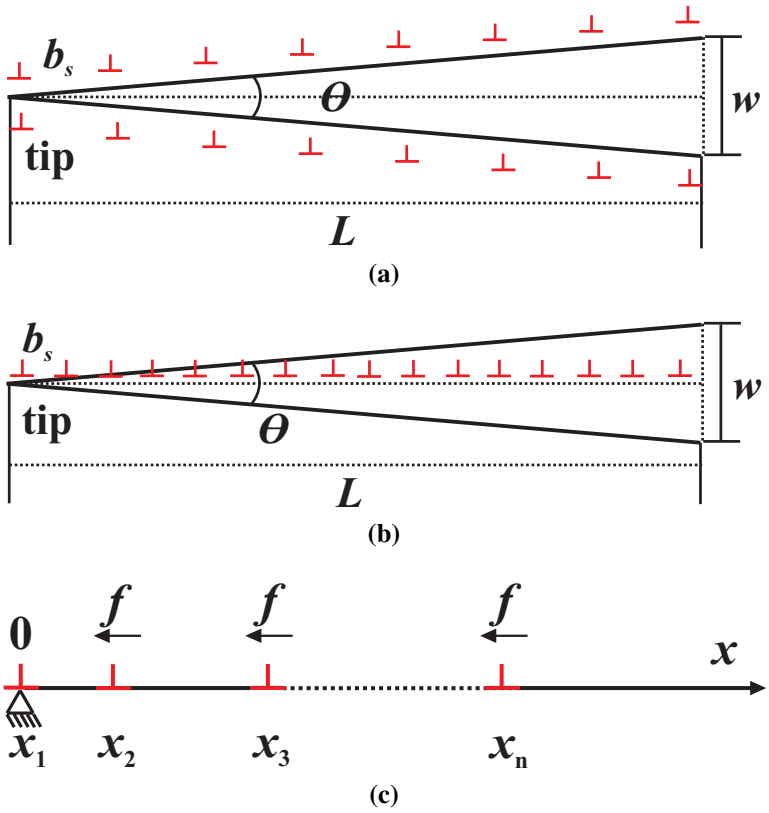


Figure 4.37: Needle domain tip with a distribution of dislocation coupled to line charges (a) Triangle tip distributing the equal dislocation coupling charge. (b) Due to the small opening angle of needle tip, all the equivalent dislocations coupling charge are distributed along one straight line. (c) The relationship of each dislocation coupling charge along the x-axis.

Typical needle domains have narrow width ($w \sim 10$ μm) and a sharp tip (about $1°$). As illustrated in figure 4.37a, we assume that the wedge shaped needle tip with the length L is made up by equal dislocations b_s and charges q_s over two domain walls. The relationship of the effective dislocation b and charge q with dislocation b_s and charge q_s is given by:

$$b_s = \frac{b}{n} \qquad q_s = \frac{q}{n} \tag{4.6}$$

where, n is total number of the equivalent dislocations and charges distributed over the needle tip. Each equivalent dislocation coupling charge has equal value, but the distance between

adjacent dislocations need not keep the same spacing. Their spacing depends instead on the equilibrium relationship between the cumulative modified Peach-Koehler force F_{cr} and resistance force from the lattice.

The opening angle θ of the needle tip is usually small. Therefore, we can think of all the equivalent dislocations and charges distributed along one straight line (longitude direction of needle domain), as shown in figure 4.37b. Fix the first dislocation at the tip and define this as the origin of the x_1-axis. Other dislocations are successively placed at positions x_i, as shown in figure 4.37c. Correspondingly, the final one is situated at x_n, which is fixed and equal to the length of needle tip. Additionally, the spacing between first one and final one, which is $x_n - x_1 = L$, is determined by the needle width and opening angle, measured from experiment. Each discrete dislocation is assumed to be acted upon by the resistance force $f = F_{cr}$, whose direction is marked in figure 4.37c. This resistance force is a function of the burger's vector b and friction stress τ_0:

$$f = \tau_0 b_s \tag{4.7}$$

First we can take an example of the case $n = 2$, where the modified Peach Koehler force F is obtained directly from Eq. 2.41. The resistance force f can be calculated using the equilibrium state of a second dislocation and line charge, namely $f = F$. Then an estimate of the friction stress τ_0 will be obtained. Now, if we increase the number of dislocations and charge distributed on the needle tip, the calculated friction stress τ_0 will change. How can we choose the number n to get a consistent friction stress τ_0?

From Eq. 2.41, we know the relationship of the modified Peach Koehler force acting on each dislocation and charge as follows:

$$F_i \propto b_s^2 \sum_{i=1, i\neq j}^{n} \frac{1}{x_j - x_i} \tag{4.8}$$

Now, let $n \to \infty$; the approximate solution of x_i [70] is given by:

$$n \to \infty, \quad x_n \propto \frac{b_s}{n\tau_0}(n-1)^2 \tag{4.9}$$

And then,

$$L \approx x_n \propto \frac{b}{n\tau_0}(n-1)^2 \tag{4.10}$$

Therefore,

$$\tau_0 \propto \frac{b}{L}\frac{(n-1)^2}{n^2} \tag{4.11}$$

According to Eq. 4.11, the relationship between friction stress τ_0 and the number n of distributed dislocations and charges is as sketched in figure 4.38. We find that the friction stress τ_0 increases as the number n increases, when the number n is less than 30. When $n > 30$, the friction stress obtained from simulation is approaching a stable value.

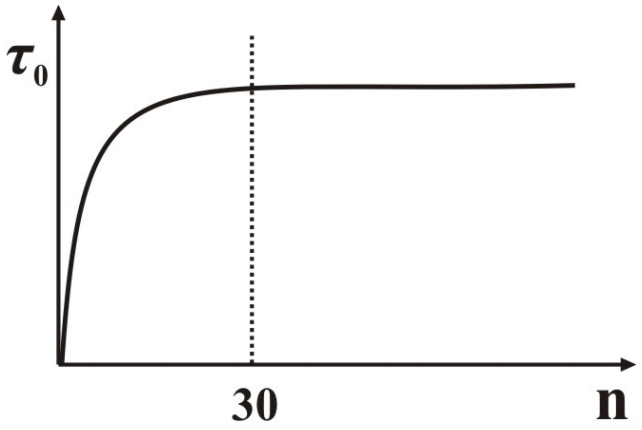


Figure 4.38: The relationship between friction stress τ_0 and the number n of distributing dislocations coupling charge

In computation, we adopt the following information: opening angle $\theta = 0.8^\circ$ and width $w = 10$ μm. Figure 4.39 then gives the nondimensional friction stress (τ) for an effective dislocation $\mathbf{b} = 3\sqrt{2}\varepsilon_0 w/2\,[1\ 1\ 0\ 0]$ with a positive line charge $\mathbf{q} = \sqrt{2}p_0 w\,[0\ 0\ 0\ 1]$, based on different numbers of the distributed dislocations and charges from n =2 to n =50. This friction stress is normalized by σ_0 given in section 4.1. It is found that the calculated friction

stress increases as the number of discrete dislocations increases, which is in agreement with the expected trend shown in figure 4.38. When the selected number n in the simulation is greater than 30, the obtained friction attains a stable value, approximately $\tau_0 = 2.3$. The corresponding friction can be calculated by Eq. 4.7. Hence the measured needle parameters ($\theta,\ w, and\ L$) determine the value of the friction stress, and thus F_{cr}.

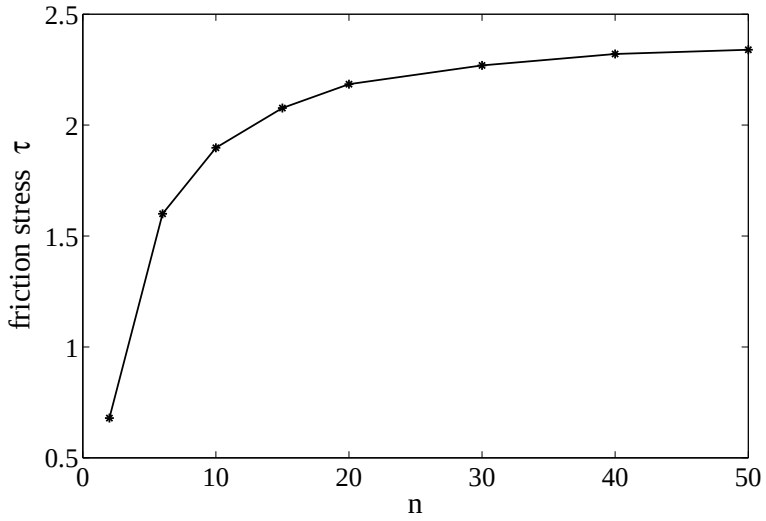


Figure 4.39: The relationship between friction stress (τ) and the number n of distributing dislocations coupling charge

4.11 Conclusions

The electromechanical fields produced by 90° a-a needle domains in $BaTiO_3$ single crystals have been modelled as the field of an effective edge dislocation and line charge. Due to material anisotropy and electromechanical coupling, the interaction of needle domains differs significantly from classical results for interaction of dislocations in isotropic media. For pairs of identical parallel needle domains, no stable equilibrium configuration is found. However, pairs of needles with opposite effective charge can form stable equilibrium configurations. The results suggest that the needle tip interactions tend to be dominated by electrostatic terms in $BaTiO_3$ single crystals.

Herringbone-type arrays of needle domains were confirmed to be stable, though the needles towards the end of such a pattern are only weakly bound to the array. Conversely, the comb-like arrays of needle domains with identical tips are unstable within the model, which is not consistent with the experimental observation. This paradoxical result leaded to a more careful analysis of the influence of screening by space charges on the stability of needle pattern.

Through studying the interaction between two needle domains with identical tips, the existence and position of stable equilibrium states were found to be sensitive to a change in the quantity of polarization charge. Especially, when the polarization charge was reduced to $Q = 0.48q$, the inclining angle θ of tip line of these two needles was $44.9°$. The corresponding configuration had minimum energy, which means that this configuration was most stable. It is noteworthy that the tip front of comb-like needles observed in experiment were perpendicular to the longitude direction. Additionally, based on the study of domain bundle boundaries in a $BaTiO_3$ single crystal, the model of needle domain works well to explain and analyse the fields and interaction of needle bundle domains.

Finally, according to the shape of a needle domain, the friction stress could be estimated using the theory of dislocation pile-up group. It was found that the normalized frictional shear stress τ_0 was about 2.3, equivalent to a shear stress resistance of about 6 MPa to the motion of needles.

5

Chapter 5 Boundary effect

In chapter 4, we have analysed the fields due to the needle domain without the effect of boundary conditions. However, in practice, the size of specimen is finite. How does the existence of a boundary affect the distribution and arrangement of needle domains? This chapter will discuss the boundary value problem based on the superposition theory proposed by Van der Giessen $et\ al.$ [64, 94].

5.1 Superposition theory for boundary condition

We have known the constitutive equations for a piezoelectric medium describing the relationship of mechanical stress σ_{ij} and electrical displacement D_i with the displacement gradients $u_{k,m}$ and the electric potential gradients $\varphi_{,m}$ are

$$\sigma_{ij} = C_{ijkm}u_{k,m} + e_{mij}\varphi_{,m} \tag{5.1}$$

$$D_i = e_{ikm}u_{k,m} - \kappa_{im}\varphi_{,m} \tag{5.2}$$

where C_{ijkm}, e_{mij}, and κ_{im} are the tensors of elastic, piezoelectric, and dielectric constants, respectively. Additionally, the relation between electric potential φ and electric field E_i is

$$E_i = -\partial\varphi/\partial x_i = -\varphi_{,i} \tag{5.3}$$

Superposition theory is used to calculate the fields due to the needle domains, as illustrated in figure 5.1. The fields produced by the needle domains are equivalent to the fields of an edge dislocation coupling with a line charge, which is stated in Chapter 2. In figure 5.1, the needle domain is represented as an edge dislocation ($\perp$) and a line charge ($\oplus$). The initial problem, which is considered to be subject to traction (T_0) on S_f, displacement (U_0) on S_u, charge (q_0) on S_q and electric potential (ϕ_0) on S_ϕ, can be decomposed into singular fields ($\sim$) without boundary conditions and the image field ($\wedge$) as a complementary solution. The displacement, stress, electric potential and electric displacement fields of the original problem are written as,

$$u_i = \widetilde{u}_i + \widehat{u}_i \tag{5.4a}$$

$$\sigma_{ij} = \widetilde{\sigma}_{ij} + \widehat{\sigma}_{ij} \tag{5.4b}$$

$$\varphi_i = \widetilde{\varphi}_i + \widehat{\varphi}_i \tag{5.4c}$$

$$D_i = \widetilde{D}_i + \widehat{D}_i \tag{5.4d}$$

Corresponding strain ε_{ij} and electric E_i fields can be calculated by constitutive equations Eqs. 5.1 and 5.2.

The ($\sim$) fields are the superposition fields associated with the individual needles, keeping their current configuration but in an infinite medium. For a set of N needles,

$$\widetilde{\varepsilon}_{ij} = \sum_{J=1}^{N} \widetilde{\varepsilon}_{ij}^{(J)}, \;\; \widetilde{\sigma}_{ij} = \sum_{J=1}^{N} \widetilde{\sigma}_{ij}^{(J)}, \;\; \widetilde{E}_i = \sum_{J=1}^{N} \widetilde{E}_i^{(J)}, \;\; \widetilde{D}_i = \sum_{J=1}^{N} \widetilde{D}_i^{(J)} \tag{5.5}$$

where, $\widetilde{\varepsilon}^{(J)}$, $\widetilde{\sigma}^{(J)}$, $\widetilde{E}^{(J)}$ and $\widetilde{D}^{(J)}$ represent the strain, stress, electric field and electric displace-

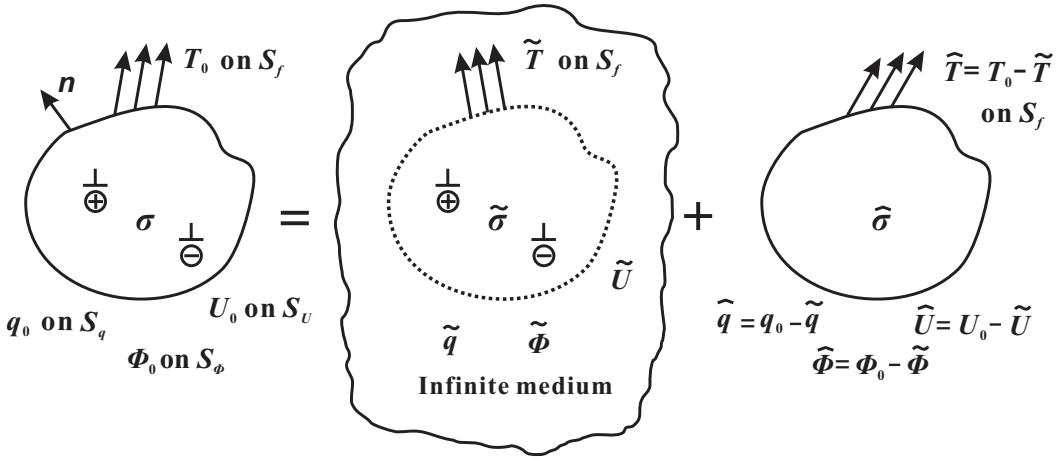


Figure 5.1: Decomposition of the boundary value problem into the sum of the singular ($\sim$) fields associated with the individual needles and the image ($\wedge$) fields that enforce the prescribed boundary conditions.

ment of the J^{th} needle domain in an infinite medium, respectively. The boundary values at the actual boundary S are:

$$\widetilde{\sigma}_{ij} n_j = \widetilde{T} \qquad \text{on} \quad S_f \tag{5.6}$$

$$u = \widetilde{U} \qquad \text{on} \quad S_u \tag{5.7}$$

$$\widetilde{D}_i n_i = -\widetilde{q} \qquad \text{on} \quad S_q \tag{5.8}$$

$$\varphi = \widetilde{\phi} \qquad \text{on} \quad S_\phi \tag{5.9}$$

where, n is the outer unit normal to boundary S, and $S = S_u \cup S_f$, $S = S_q \cup S_\phi$. These boundary conditions facilitate the solution of the image field.

In the ($\sim$) field, the sum of the individual needle fields does not in general satisfy the prescribed boundary conditions. The image($\wedge$) fields are used to correct for the actual boundary conditions by solving the image problem in a region with no dislocations or point charges. Therefore, the image field serves as a complementary field. Since the ($\wedge$) fields are smooth and continuous fields without singularities, the boundary value problem can be solved by any convenient numerical method such as the finite element method or the boundary element method. Here, we adopt the finite element method to obtain the complementary solution. The boundary

loads of the complementary ($\wedge$) fields are:

$$\widehat{T} = T_0 - \widetilde{T} \tag{5.10}$$

$$\widehat{U} = U_0 - \widetilde{U} \tag{5.11}$$

$$\widehat{q} = q_0 - \widetilde{q} \tag{5.12}$$

$$\widehat{\phi} = \phi_0 - \widetilde{\phi} \tag{5.13}$$

The potential energy is contributed by three parts including strain energy, electrical energy, and traction and charge imposed on the boundary edge. Total potential energy is calculated as follows:

$$U_E = \frac{1}{2}\int_v (\sigma \cdot \varepsilon + E \cdot D)\, dv - \int_{S_f} T_0 \cdot U\, ds - \int_{S_q} \phi \cdot q_0\, ds \tag{5.14}$$

Variations of the total potential energy can be considered in order to find a steady equilibrium pattern formed by the needle domains.

The interaction force of the needle domains is also needed. This can be calculated by:

$$F_m^{(I)} = \varepsilon_{ilm} k_l (\widehat{\sigma}_{ij} + \sum_{J \neq I}^{N} \widetilde{\sigma}_{ij}^{(J)}) b_j^{(I)} + (\widehat{E}_m + \sum_{J \neq I}^{N} \widetilde{E}_m^{(J)}) q_4^{(I)} \tag{5.15}$$

where, $F_m^{(I)}$ represents the components of the force acting on the needle N_I. The needle domain N_I is modelled as an edge dislocation $b^{(I)}$ coupled with a line charge $q^{(I)}$. ε is the permutation tensor, k is the unit vector along the coordinate x_3, and N is the total number of interactive needles.

5.2 The boundary influence on the fields and arrangement of the needle domains

The boundary value problem with free traction ($T_0 = 0$) and zero potential ($\phi_0 = 0$) will be discussed in this section, which is a common condition in practice. We choose a square region of 5 mm$\times$ 5 mm ($500w \times 500w$) to investigate the effect of the boundary on needle domains. According to above superposition theory, the boundary value problem is decomposed into two parts: (1) infinite solution; (2) complementary solution, which are illustrated in figure 5.2. The polarization direction of the parent domain (P^1) is along x_2. The 90° a-a needle domains are studied.

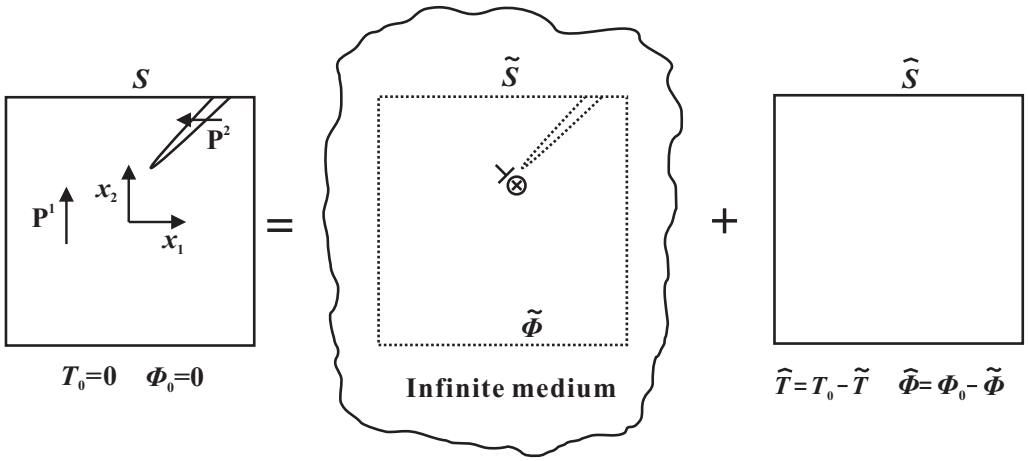


Figure 5.2: Decomposition of the boundary value problem with free traction and zero potential

The boundary loads are prescribed or computed as follows:

(1) The original problem: $T_0 = 0, \quad \phi_0 = 0$

(2) Infinite part ($\sim$): $\widetilde{T} = \widetilde{\sigma}_{ij} n_j, \quad \widetilde{\phi} = \varphi$, computed from solution of ($\sim$) problem

(3) Complementary part ($\wedge$): $\widehat{T} = T_0 - \widetilde{T}, \quad \widehat{\phi} = \phi_0 - \widetilde{\phi}$

In ($\sim$) field, the solution of the stress $\widetilde{\sigma}$ and electric potential $\widetilde{\phi}$ is computed by the theory given in section 2.4. The corresponding stress field and electric field are superposed from each discrete dislocation and line charge, as calculated by Eq. 5.5. Additionally, the boundary condi-

tion on virtual edge $\widetilde{S}$ is found for the calculation of boundary condition in the complementary problem.

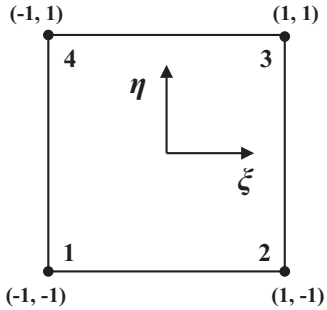


Figure 5.3: The element unit with the local coordinate (ξ, η).

The complementary problem was solved using the finite element method in the commercial software ABAQUS. The region of $500w \times 500w$ was meshed using a 4-node bilinear plane-stress piezoelectric quadrilateral element, CPS4E. Due to the regular shape, the structured meshing technique was adopted to generate a structured mesh with the element size $1w \times 1w$. The 4-node shape function was used to interpolate the solution between the discrete values obtained at the mesh nodes, given as follows:

$$N_1 = \frac{1}{4}(1-\xi)(1-\eta) \tag{5.16a}$$

$$N_2 = \frac{1}{4}(1+\xi)(1-\eta) \tag{5.16b}$$

$$N_3 = \frac{1}{4}(1+\xi)(1+\eta) \tag{5.16c}$$

$$N_4 = \frac{1}{4}(1-\xi)(1+\eta) \tag{5.16d}$$

where, N_i $(i = 1,\ 2,\ 3,\ 4)$ are interpolation functions at each node. The local coordinate (ξ, η) in the element is shown in figure 5.3.

The anisotropic material constants of the $BaTiO_3$ single crystal are obtained from the table 1.1. Nondimensionalization as listed in table 4.1 is used in the computation, and the same characteristic parameters are also adopted. Due to the anisotropic properties of $BaTiO_3$ single crystal, we need to specify material orientation in the process of analysis. Here, the polarization

direction is set along the x_2 axis.

5.2.1 Single needle domain under the effect of BC

For the finite problem, we now ask how are the needles affected by the traction free, zero voltage boundary condition? Comparing the infinite case given in Chapter 4, what is the influence of boundaries?

In this section, one 90° a-a needle domain placed at different positions in the region is used to discuss the effect of the boundary. This needle domain has width w and is oriented at 45° to the x_1 positive direction. Its tip position is set in the range from the point $(-240w, -240w)$ to $(240w, 240w)$, on a line along its longitude direction (the line of $x_2 = x_1$). We consider the case of a needle tip with charge $Q = 0.48q$ where $q = \sqrt{2}p_0 w$.

To analyse the effect of the boundary on the needle domain, the change in the contour maps of stress σ_{11}, as an example, is tracked for the needle tip placed at the different positions. Figure 5.4 gives a contour map of stress σ_{11} for the single needle domain without boundaries. Figure 5.5 selectively gives the contour maps of stress σ_{11} for the needle tip located at $(0, 0)$, $(60w, 60w)$, $(160w, 160w)$, and $(220w, 220w)$. The stress fields in both figures 5.4 and 5.5 are normalized by σ_0. From figures 5.5a-5.5d, the values of stress σ_{11} at the edges of $x_1 = -250w$ and $x_1 = 250w$ are always equal to 0, as required by the boundary condition of free traction on these edges.

First, the stress σ_{11} for the needle tip located at the origin is analysed, as shown in figure 5.5a. Comparing with the reference case given in figure 5.4, the stress (σ_{11}) field close to the needle tip in the range of about $200w \times 200w$ is almost unaffected by the boundary. Out of this range, a slight influence due to the boundary appears. When the needle tip is at position $(60w, 60w)$, the central region $(200w \times 200w)$ remains basically uninfluenced. This suggests that when a needle tip is far from the boundary, we can ignore the boundary effect and use the infinite-case model to analyse interaction among needle domains.

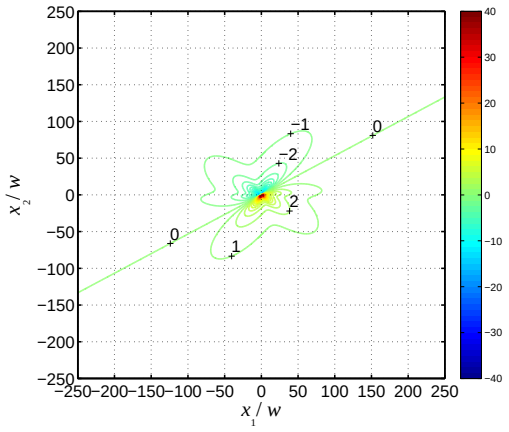
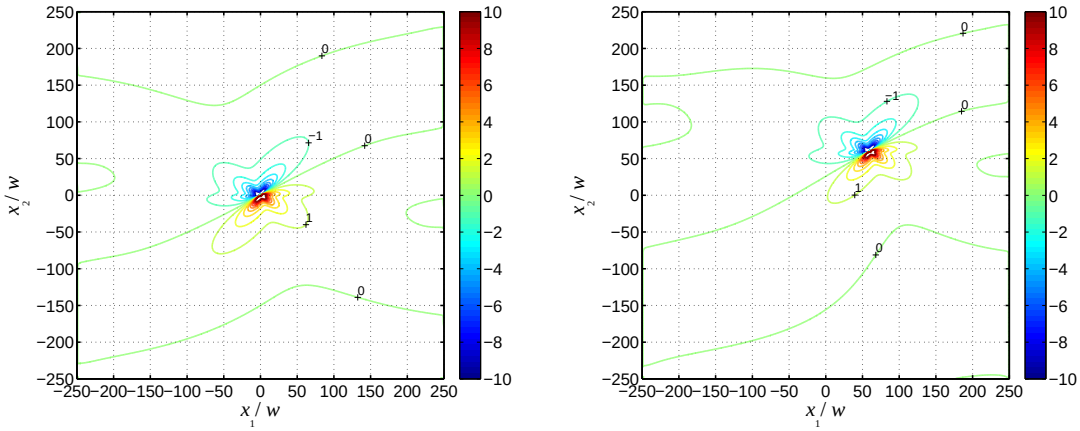
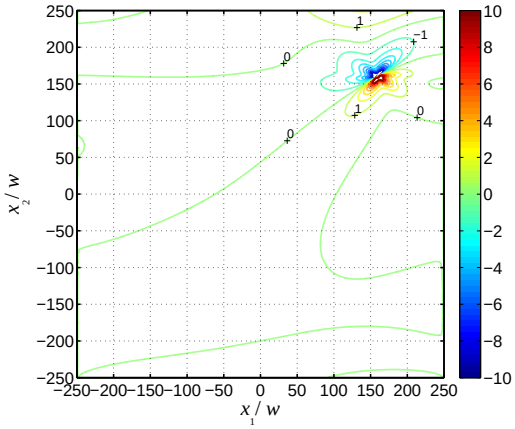


Figure 5.4: Contour map of stress σ_{11} for one single needle domain with $0.48q$ charge at its tip for the infinite case.

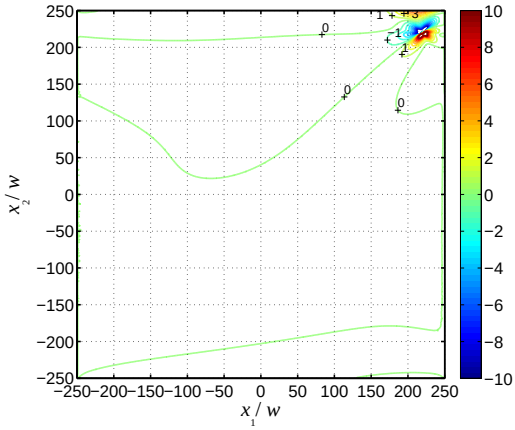


(a) Tip position (0, 0)

(b) Tip position $(60w,\ 60w)$



(c) Tip position $(160w,\ 160w)$



(d) Tip position $(220w,\ 220w)$

Figure 5.5: Stress σ_{11} fields produced by a single needle domain located at different position, (0, 0), $(60w,\ 60w)$, $(160w,\ 160w)$, and $(220w,\ 220w)$.

As the needle tip approaches the boundary, the influence of the boundary becomes strong, see figures 5.5c and 5.5d. When the needle tip is really close to boundary, as in figure 5.5d, the gradient of stress around the tip becomes large, and the action range of the needle shrinks (stresses drop off rapidly with distance). Similar changes happen to the fields of other stress components and electric field.

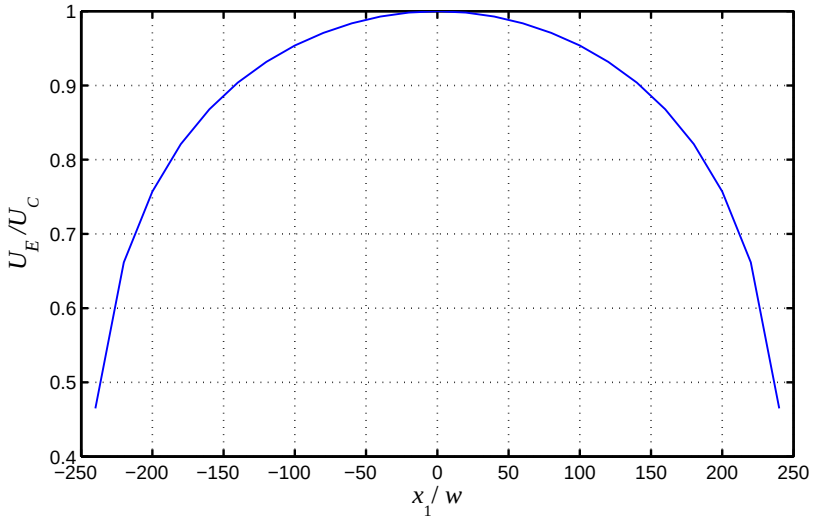


Figure 5.6: Change in energy as the needle domain approaches to an edge.

The internal energy U_E due to a single needle domain, in the $500w$ by $500w$ region, was calculated using Eq. 5.14. The corresponding fields from Eq. 5.4 are found by superposition of the infinite solution and complementary solution. The energy (U_C) due to the needle domain placed at the origin is used as reference case and used to normalize the needle domain energy when situated at the different positions. The figure 5.6 shows the change of non-dimensional energy (U_E/U_C), as the needle tip varies in distance from the boundary. From this figure, it is found that energy (U_E/U_C) is decreasing when the needle tip is close to an edge. This means that a single needle domain is energetically driven to either shortening until it disappears or extending through the whole crystal. Only if the needle domain is pinned by lattice friction or some other resistance, it terminates within the crystal in equilibrium. A similar result is well known for dislocations in isotropic media.

5.2.2 A pair of needle domains in a finite crystal

In section 5.2.1, we found that single needle domain fields are affected by nearby boundaries. Next consider whether the boundary affects the interaction of adjacent needle domains. Through studying a pair of needles with $Q = 0.48q$ in section 4.6, we found that the configuration of needle tips aligned on a line at about $45°$ to the x_1 negative direction. Does this stable equilibrium configuration still exist near a boundary? Experimental evidence [52, 92] suggests that it might do. To analyse the interaction of two adjacent needle domains, a pair of identical needle domains (N_1&N_2) oriented at $45°$ to the x_1 positive direction are chosen, as illustrated in figure 5.7. The polarization vectors of the parent domain and needle domains are $\mathbf{P}^1 = [0\ 1\ 0]p_0$ and $\mathbf{P}^{N_1} = \mathbf{P}^{N_2} =$ [-1 0 0]p_0, respectively. Each needle domain is modelled as an effective edge dislocation ($\mathbf{b} = (3\sqrt{2}\varepsilon_0 w/2)\,[1\ 1\ 0\ 0]$) coupled with line charge ($\mathbf{Q} = 0.48q[0\ 0\ 0\ 1]$, $q = \sqrt{2}p_0 w$).

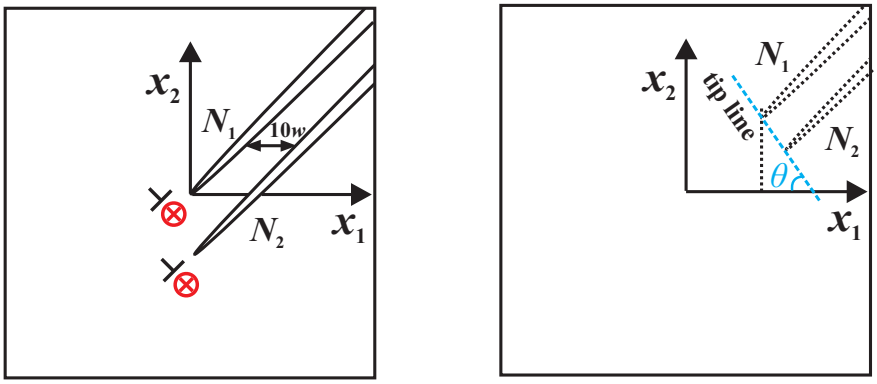


Figure 5.7: Two interactive needle domains approaching to edge

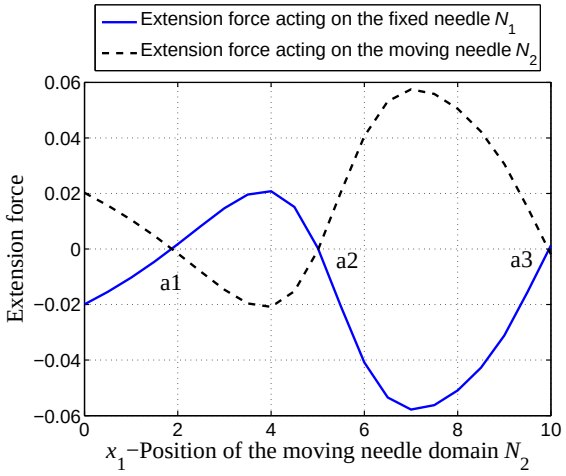
First, we study interaction between of a pair of needle domains with spacing $10w$ (along the x_1 direction). The needle N_1 is placed at the three different initial positions including the origin (0, 0), a near-center position ($50w$, $50w$) and a near-boundary position ($200w$, $200w$), respectively. The needle N_2 is moved around each fixed N_1 needle tip along its longitude direction $x_2 = x_1 - 10w$. The extension force and total energy are computed using Eq. 5.15. Figure 5.8 shows the extension force acting on each needle and total energy due to two interactive

needle domains (N_1 & N_2). The extension force is normalized by $\sigma_0 w$, and the energy by U_C.

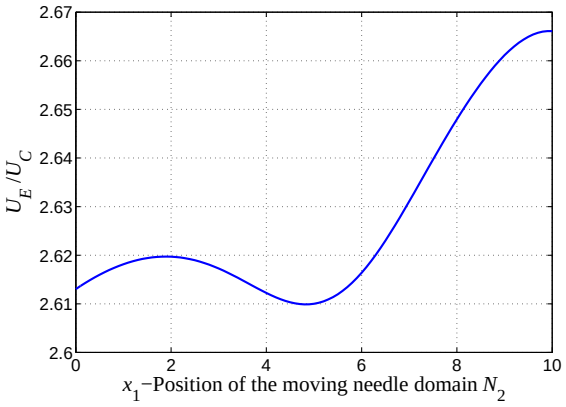
Figure 5.8a shows the change of extension forces acting on each needle domain as the needle N_2 moves around N_1 which is fixed at the origin. Note that the extension forces have the same absolute value but have opposite sign. The same result appears in the infinite case of two adjacent needle domains. We can explain this result based on Eq. 5.15. The first and third terms in Eq. 5.15 come from contribution of complementary field which varies with boundary condition related to the positions of needles. If the effect of boundary condition is small enough, it means that the values of first and third terms could be ignored. This causes the above interaction to degenerate to the infinite case. Therefore, we can conclude that there is almost no influence from the boundary on this pair of needle domains.

In addition, we find that there are three equilibrium positions a1, a2, and a3 in figure 5.8a. However, only position a2 is stable for both needle domains. The variation of energy due to two needle domains shown in figure 5.8b confirms that position a2 is in a potential well. Correspondingly, the tip line of two needles in stable equilibrium is at 45° to the x_1-axis positive direction, as in the infinite case.

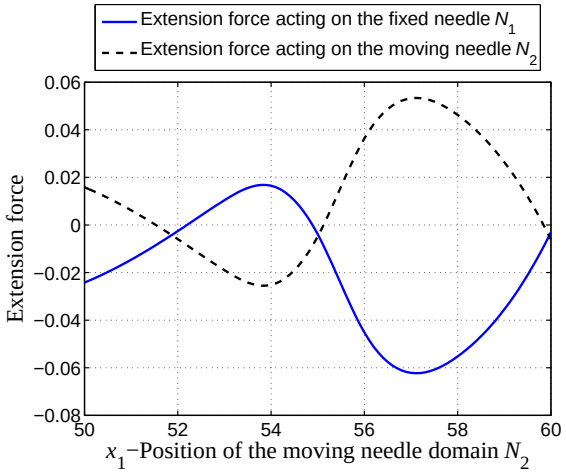
When the pair of needle domains is away from the central region, at the near-centre position, figures 5.8c and 5.8d give the extension force and the stored energy. The data in figure 5.8c shows that the extension forces become more negative than in the previous case. The negative extension force results from the effect of the boundary acting on both needle domains. Additionally, we find there is no equilibrium position for both needle domains even through there are several zero intersections shown in figure 5.8c. This pair of needle domains can not stay in equilibrium without lattice friction or some other resistance to hold the needle domains. In section 4.10, a friction stress value was computed based on the wedge-shaped tip configuration of a needle domain observed in experiment. This gave friction stress of $\tau_0 = 2.34$. The corresponding friction force is $F_{cr} = b\tau$, giving $F_{cr} = 0.05$, which is normalized by $\sigma_0 w$. Therefore, with lattice friction, this pair of needle domains can stay in any position where the extension



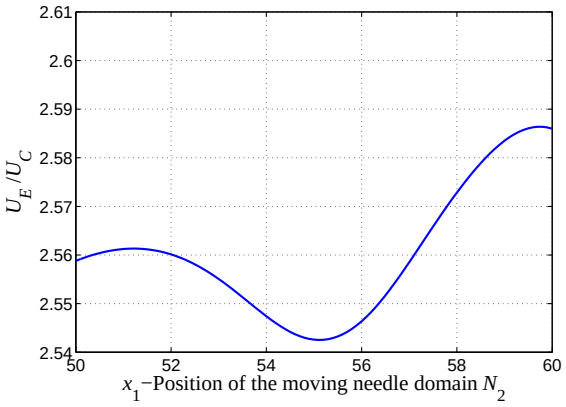
(a) Needle N_1 fixed at (0, 0)



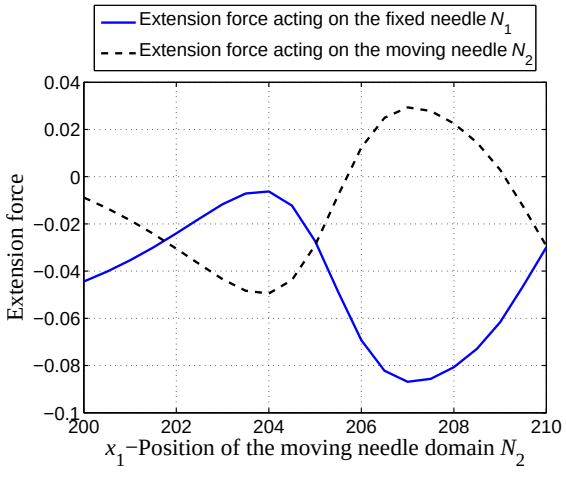
(b) Needle N_1 fixed at (0, 0)



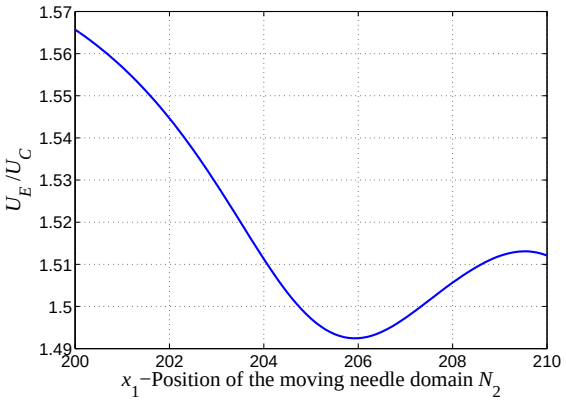
(c) Needle N_1 fixed at ($50w$, $50w$)



(d) Needle N_1 fixed at ($50w$, $50w$)

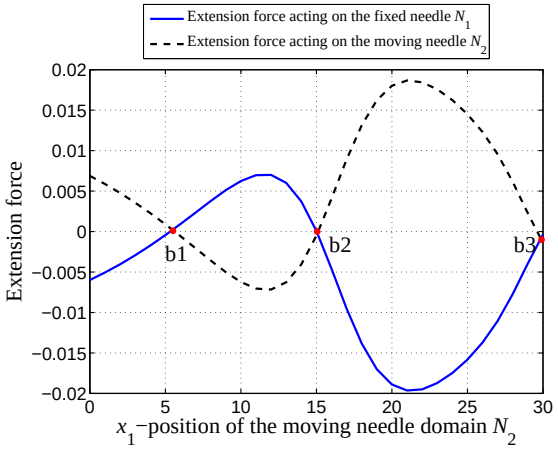


(e) Needle N_1 fixed at ($200w$, $200w$)

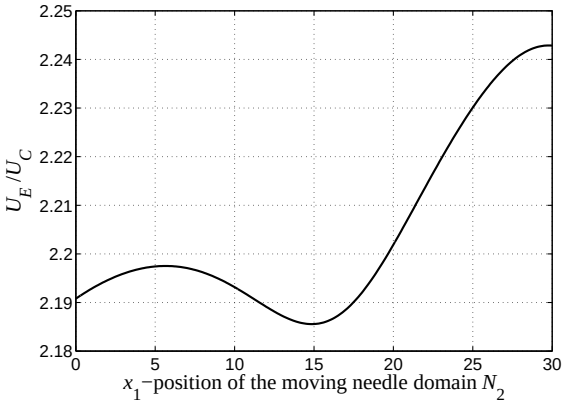


(f) Needle N_1 fixed at ($200w$, $200w$)

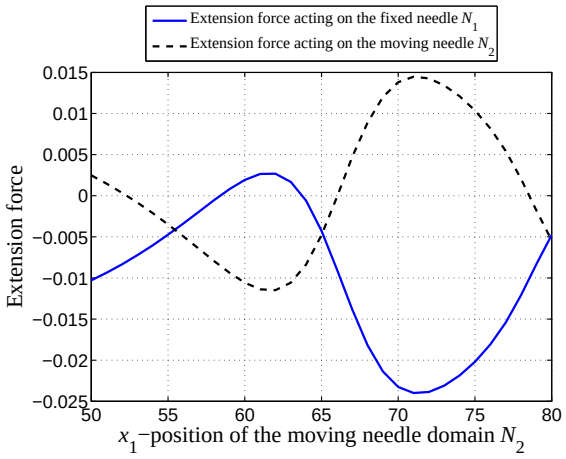
Figure 5.8: Extension forces acted on two needle domains with spacing $10w$ when needle N_1 is fixed at (0, 0) ($50w$, $50w$) and ($200w$, $200w$), respectively.



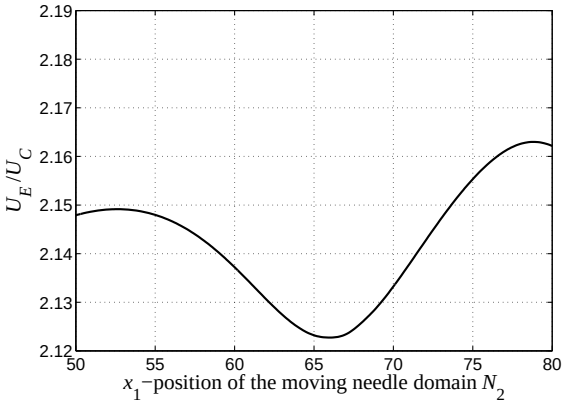
(a) Needle N_1 fixed at (0, 0)



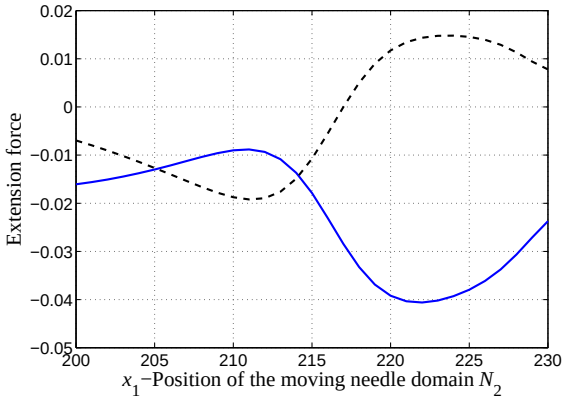
(b) Needle N_1 fixed at (0, 0)



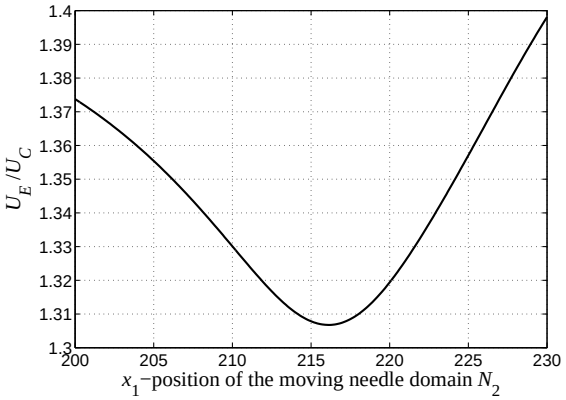
(c) Needle N_1 fixed at ($50w$, $50w$)



(d) Needle N_1 fixed at ($50w$, $50w$)



(e) Needle N_1 fixed at ($200w$, $200w$)



(f) Needle N_1 fixed at ($200w$, $200w$)

Figure 5.9: Extension forces acted on two needle domains with spacing $30w$ when needle N_1 is fixed at (0, 0) ($50w$, $50w$) and ($200w$, $200w$), respectively.

force on both needle domains is smaller than the critical resistance force F_{cr}. Referring to figure 5.8c, this gives a wide range of stable positions. However, from the figure 5.8d, we could expect to find N_2 close to the minimum energy position, which is not much different from the previous case, shown in figures 5.8a and 5.8b.

When needle N_1 is in the near-boundary position, at $(200w,\ 200w)$, figure 5.8e gives the extension forces acting on each needle domain. Both needle domains are close to an edge, and the extension forces are again shifted towards negative values, as shown in figure 5.8e. The boundary effect now provides a strong traction to drive the needle domains to further shorten towards the edge. There is no equilibrium position for N_1 in the range shown, unless lattice friction is present. From the variation of energy shown in figure 5.8f, the bottom of the energy well for needle N_2 is at position $(205.8w,\ 195.8w)$ with needle N_1 fixed at position $(200w,\ 200w)$. The energy well is deeper in figure 5.8f than in figures 5.8b and 5.8d, suggesting that proximity to the boundary stabilized the needle pattern.

Additionally, we also select a pair of needle domains with wider spacing $30w$ to compare with needle domains with the narrow spacing mentioned above. Similarly, the needle N_1 is fixed at three different position, (0, 0), $(50w,\ 50w)$ and $(200w,\ 200w)$, respectively. While the needle N_2 tip is moving around each fixed N_1 needle tip along the direction of the line $x_2 = x_1 - 30w$. Figures 5.9a-5.9f present the variation of extension force and energy for both needle domains located at different position.

Figure 5.9a shows the extension force of this pair of needle domains when N_1 needle is fixed at origin. We note that there are still three zero intersections (b1, b2, and b3) marked in figure 5.9a, and only one position b2 is corresponding to a stable equilibrium state for both needle domains. This result reveals that a central range with radius about $30w$ is not affected by the boundary. The energy potential shown in figure 5.9b reconfirms that b2 is a stable equilibrium position. Comparing the interaction between two needle domains with narrow spacing $(10w)$ with the case of wide spacing $(30w)$, the value of the extension forces are smaller when

the needles have wide spacing. Then the critical resistance force F_{cr} taken as 0.05 can hold the needles in place. Therefore, in practice, it is expected that coarsely spaced needle domains are most likely to be stable.

5.2.3 The effect of polarization charge on interaction of needle domains

In this section, we will discuss the effect of changing the polarization charge on the equilibrium position of two adjacent needle domains, considering the influence of boundaries. Based on the study of the effect of polarization charge mentioned in Chapter 4, we know that the equilibrium configuration of two adjacent needle domains is sensitive to the polarization charge at the needle tip. There is no stable equilibrium configuration until the polarization charge reduced to 73.4% of the full spontaneous polarization value, $q(\sqrt{2}p_0w)$. In addition, we also found that the minimum energy configuration of two interactive needle domains corresponds to the polarization charge $Q = 0.48q$. With the influence of boundaries, does the equilibrium configuration for adjacent needle domains still exist? How does the energy due to two interactive needle domains change with variation of polarization charge? Based on section 5.2.2, the extension force gradually becomes more negative as needles shorten to approach an edge. When a pair of moving needle domains is really close to an edge, their equilibrium configuration occurs at the intersection between the line of extension and the x_1 axis. Accordingly, the angle θ between tip line and the negative x_1 axis decreases as a needle domain pair approaches an edge. What happens if the polarization charge is varied?

As in section 5.2.2, a pair of needle domains with identical tips and $10w$ spacing are chosen to study the effect of changing the polarization charge. Six different positions approaching to an edge are selected for needle N_1, which are $(0, 0)$, $(50w, 50w)$, $(100w, 100w)$, $(150w, 150w)$, $(200w, 200w)$, and $(230w, 230w)$. During searching for an equilibrium configuration for each position, we fix the tip of needle domain N_1, and then move the needle domain

N_2 around N_1 along its longitude direction $x_2 = x_1 - 10w$. The influence of setting the polarization charge in the range of $0 - 0.734q$ is studied, as shown in figure 5.10. Figure 5.10 gives the change of angle θ (see figure 5.7 for a definition) with respect to the tip position x_1 of needle N_1 and the quantity of polarization charge at the needle tip Q/q. For each position, it is found that the angle θ in equilibrium state shows the same trend, as the polarization charge Q changes between 0 and 0.734%. Comparing with the infinite case, the variation of angle θ at position $x_1 = 0$ is similar, but with a slight boundary influence. For each fixed quantity of polarization charge in range of $0 - 0.734$, the angle θ decreases in varying degrees when the interactive needle pair approaches an edge.

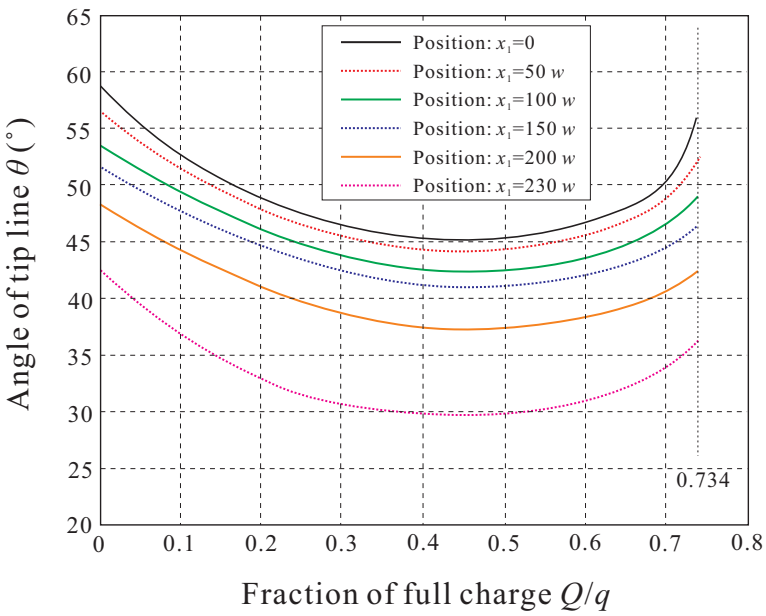


Figure 5.10: Change of angle θ with respect to the distance of tip position from edge and the quantity of polarization charge at the needle tip.

The key result is that the angle of the equilibrium needle tip line changes due to the presence of boundaries. Far from a boundary, the tip line is at $45°$ to the x_1 axis for minimum energy. But close to an edge, this angle reduces to less than $30°$.

The change of energy (U_E) due to two interactive needle domains was next computed. The energy (U_C) due to a single needle domain placed at the origin was used to nondimensionalize the results. Figure 5.11 gives the variation of the dimensionless U_E/U_C for different tip

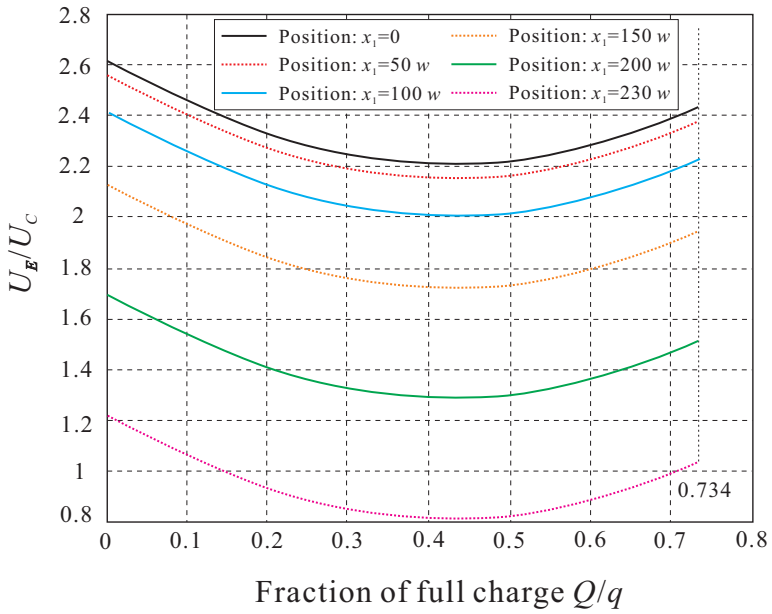


Figure 5.11: Change of energy with respect to the tip position x_1 of needle N_1 and the quantity of polarization charge at the needle tip.

positions of needle N_1 and varying quantity of polarization charge at the needle tip Q/q. The key result is that the minimum energy state is always found when $Q \sim 0.45q - 0.48q$. This is consistent with the infinite case (no boundaries) mentioned in section 4.6. This result justifies adopting the value of polarization charge at a needle tip equal to $0.48q$ for all subsequent calculations. Additionally, we note that the energy due to these interactive needle domains decreases for each fixed value of polarization charge, as the needle pair is approaching to an edge. This result is in agreement with section 5.2.1 which described a single needle having reduced energy near an edge.

5.3 Evolution of a pair of needle domains under applied compressive force

In the previous sections, we have studied the interaction and arrangement of needle domains without external loads. In this section, we discuss the evolution of a pair of needle domains under the applied external loads. During the analysis, lattice friction is used, along with the

viscous model proposed in section 4.8.1. Considering a thin specimen subject to in-plane compressive loads, the plane stress-plane electric displacement condition is used (see Chapter 2, section 2.6).

A pair of 90° a-a needle domains is selected to study the evolution of needles under the effect of external compressive loads. As shown in figure 5.12, the tips of two needle domains with spacing $10w$ along the x_1 axis are located at the tip line $y = -x$, namely inclined with angle $\theta = 45^\circ$. The position of needle N_1 tip is the origin, and the tip of needle N_2 is placed at ($5w$, -$5w$). The polarization directions of the parent domain $\mathbf{P}^1$ and needle domain $\mathbf{P}^2$ are along [0 1 0] and [-1 0 0], respectively. The compressive stress perpendicular to the direction of the parent domain is applied on a sample with dimensions $500w$ by $500w$. This compressive stress is incremented in steps of 0.01 MPa up to 0.1 MPa. At each loading step, each needle domain is allowed to reach an equilibrium state before the next load step in compressive stress. If the needles cannot reach equilibrium, loading is stopped. Alternatively, the calculation ends when any needle reaches an edge of sample. During the evolution of needle domains, we take the critical resistance force F_{cr} as 0.05 in normalized units. Only when the extension force exceeds F_{cr} in magnitude, the corresponding needle starts to move along its own longitude direction.

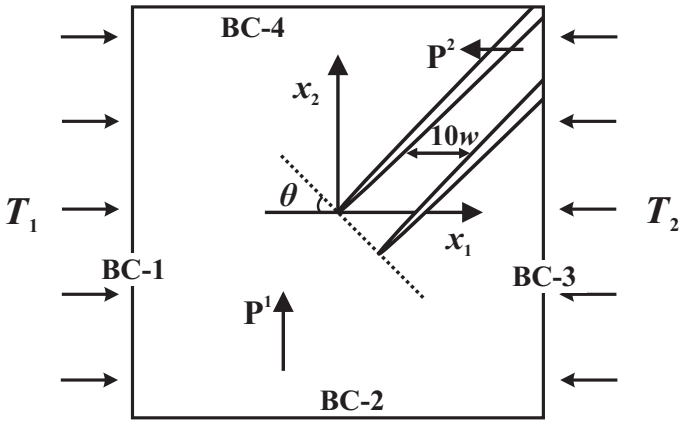


Figure 5.12: A pair of needle domains under the effect of compressive loads.

This boundary condition problem with the compressive stress is decomposed into an infinite body solution and a complementary solution, according to the superposition theory given

in section 5.1. The boundary conditions of the original problem are given as follows:

BC-1: T_1 is a positive stress increasing from 0 to 0.1 MPa with the step 0.01 MPa, and $\phi_0 = 0$ which is because the loading side is connected to ground through the loading device;
BC-3: $T_2 = -T_1$, $\phi_0 = 0$;
BC-2 and BC-4: these two edges are free of charge and free of traction, $T_0 = 0$ and $q_0 = 0$.

The extension force acting on each needle domain and the change of their tip positions are recorded during the application of the increasing compressive stress, as shown in figure 5.13. Due to the needles moving along their own longitude direction (N_1: $x_2 = x_1$ and N_2: $x_2 = x_1 - 10w$), we only give the x_1 coordinates of each needle tip. The extension force F_e is normalized by $\sigma_0 w$, and the tip position is normalized by w. Before loading the specimen, the magnitude of the extension forces acting on needles N_1 and N_2 are -0.0127 and 0.0125, respectively. When the 0.01 MPa step load starts to compresses the specimen, the corresponding extension forces decrease to -0.0272 and -0.0011. However, both needles still stay at the initial position because their extension forces are smaller than the critical friction stress F_{cr}. When the load increases to 0.03 MPa, step-3, the extension force of N_1 reaches -0.0561 and is greater than F_{cr} 0.05. The needle N_1 starts to move under the action of extension force, while N_2 needle stays at its original position. Due to the movement of needle N_1 , the relative location and the extension force of the two needles are influenced. The positions are updated according to the corresponding extension force until both extension forces are no greater than the critical friction F_{cr}. At the end of step-3, the extension forces are -0.05 and -0.0382, and the positions for both needles (N_1 and N_2) are (0.35w, 0.35w) and (5w, -5w). Comparing to the initial state, needle N_1 has shortened toward the boundary under the action of compressive loads. This could be interpreted as ferroelastic switching in which the shortened N_1 needle domains leave behind a region of parent domain (a^1 domain).

After step-3, both needle domains move under the action of the increasing compressive load. During each following step load, two needle domains re-reach a new equilibrium state

through changing the tip position of needle domains. Finally, their tips stabilized with friction, and stop at the positions (0.91w, 0.91w) and (5.84w, -4.16w). As the step load is continually increased, the two needle domains slowly shorten towards the boundary. A similar result has been observed by Potnis [52]. They found that the needle domains retreated under the application of compressive stress through the observation of optical microscope.

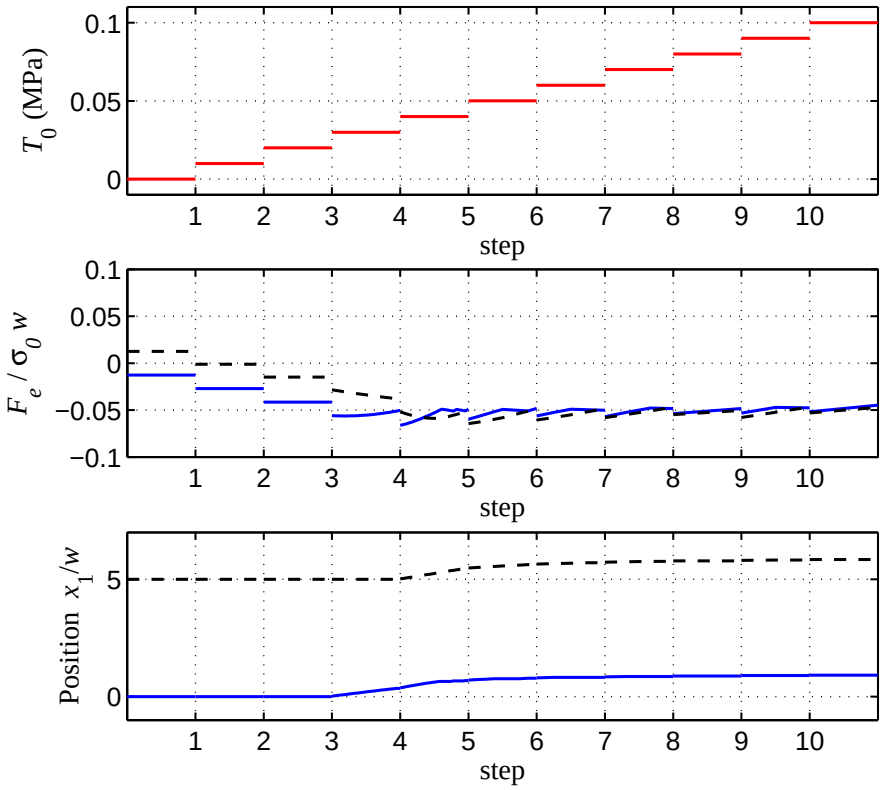


Figure 5.13: A pair of needle domains under the application of compressive step loads with increment 0.01 MPa (Solid line: needle N_1; Dash line: needle N_2).

If we enlarge the increment of the compressive step load, what happens to the evolution of these two adjacent needles? To compare with the above simulation of the loads with a small step, we will directly increase the compressive loads to 0.1 MPa through only one step. Figure 5.14 gives the compressive step load, the extension forces acting on both needles, and the tip position x_1 of both needles. We find that when the increment step of the compressive loads is enlarged, the early details of the movement of needles, which appears in the range of small

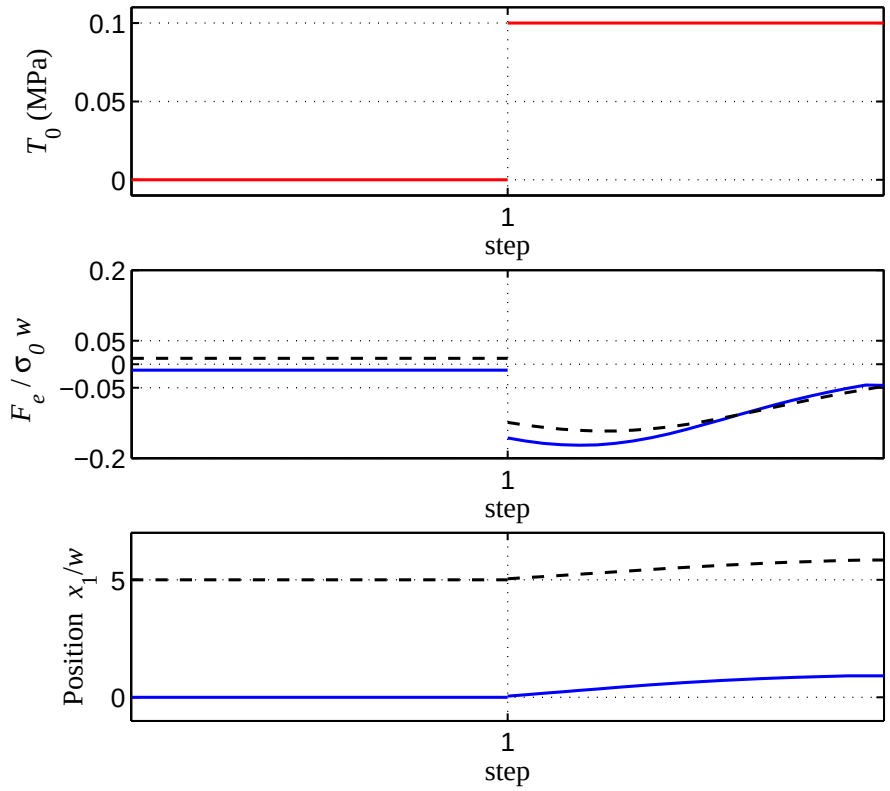


Figure 5.14: A pair of needle domains under the effect of compressive loads with large increment 0.1 MPa (Solid line: needle N_1; Dash line: needle N_2).

load, are lost. Instead, the extension forces of two needles suddenly decrease to -0.1569 and -0.1240, and both needles simultaneously start to move. Through continually updating their tip positions, they reach a final equilibrium state, balanced by friction. The N_1 and N_2 needles stop at the same positions as in the case of the loads with small step, namely (0.91w, 0.91w) and (5.84w, -4.16w), respectively. This result is the same as the case with small step loads. We need further make sure whether this coincide happen to other load case. Comparing the figures 5.13 and 5.14, the enlarged step causes an obvious increase in the magnitude of the extension force during the evolution of these two needles. For each step of loads with large increment, the extension force of both needles instantaneously changes. Therefore, for smaller step of loads, the moving process of two needles is more steady, and the evolution process is closer to quasi-static.

We next increase the compressive load to 3 MPa with small increments 0.01 MPa and

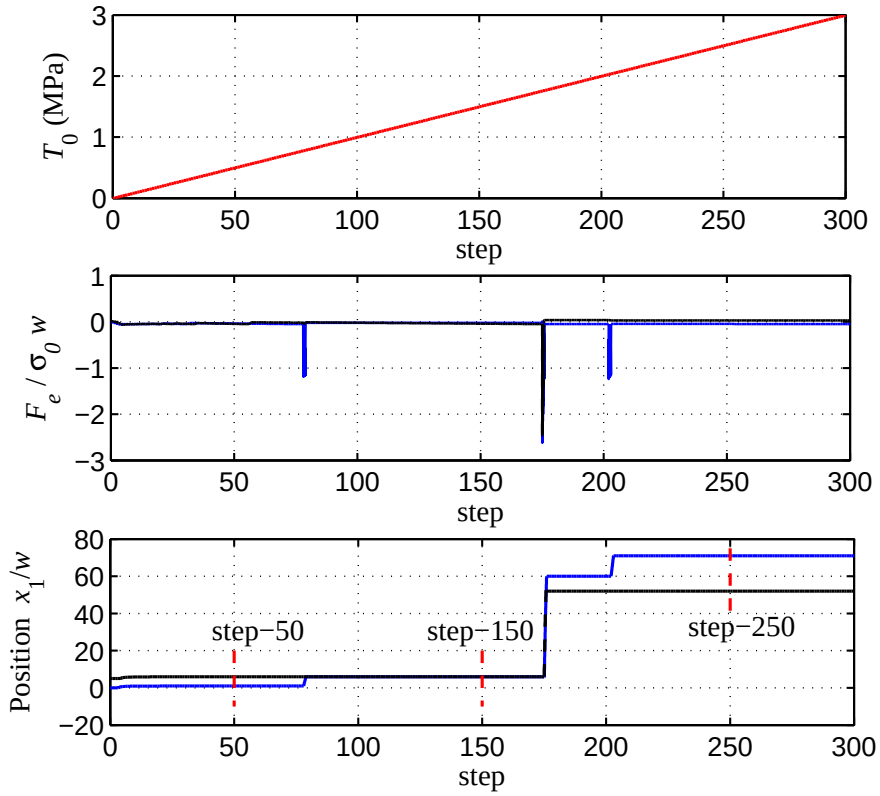
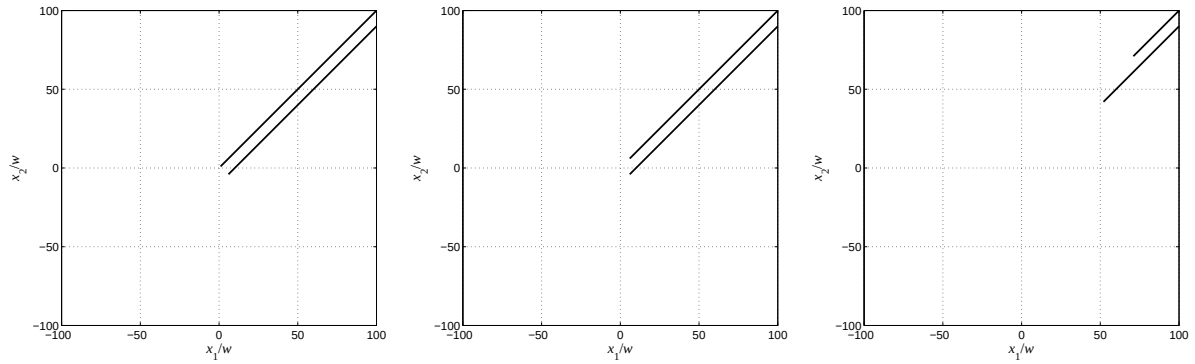


Figure 5.15: A pair of needle domains under the effect of compressive loads with increment 0.01 MPa (Blue line: needle N_1; black line: needle N_2).



(a) step-50 **(b)** step-150 **(c)** step-250

Figure 5.16: The arrangement of needle domains for the different loading steps with the increment 0.01 MPa.

alternatively with large increments 0.1 MPa, and further study the evolution of this pair of needles. Figures 5.15 gives the evolution of the two needles with the applied force increasing from 0 to 3 MPa in increments of 0.01 MPa. Figure 5.16 shows the pattern of the two needle domains at selected loading steps. At low force, both needle tips undergo small-amplitude displacements, as shown in figure 5.16a and 5.16b. When the applied force exceeds 1.77 MPa, both needles tips retreat rapidly to the side of sample in a burst of motion, as presented in figure 5.16c. The simulation shows several interesting features. First, friction stabilized the pair of needles over a range of loads, as may be expected. Then, when the needles move, they separate, and move in jumps, or rapid bursts of motion. This indicates that loading can produce an instability rather than incrementally changing the equilibrium state. Such instabilities are a known feature of dislocation dynamics simulations in isotropic media [96] and are also seen in measurements of plastic deformation [97].Furthermore, similar bursts of needle-domain motion were observed in the experiments of Potnis $et\ al.$ [52].

When the step load with increment of 0.1 MPa is instead applied and the load is gradually increased to 3 MPa, The two needle domains again retreat to the boundary of sample. Figure 5.17 shows the applied force, the extension force acting on needles, and the position x_1 of needle domains under the action of compressive loads. Comparing with the results presented in figures 5.15 and 5.17, the evolution process is different. For the compressive step load with small increment, the tips of the two needles follow each other (though separated), as shown in figure 5.15. For the larger increment step loads, the tips of two needles separate when $T_0 > 2.9$ MPa, as shown in figure 5.18. Figure 5.17 also indicates oscillations in F_e, bursts of motion and instability.

Besides the loading process, the initial positions of the needles also influences the evolution of two adjacent needles. The critical friction F_{cr} and the viscosity term η in viscous model are also important factors influencing the evolution of needles. From the above simulation, we can conclude that the results are dependent on the load steps, with no one-to-one

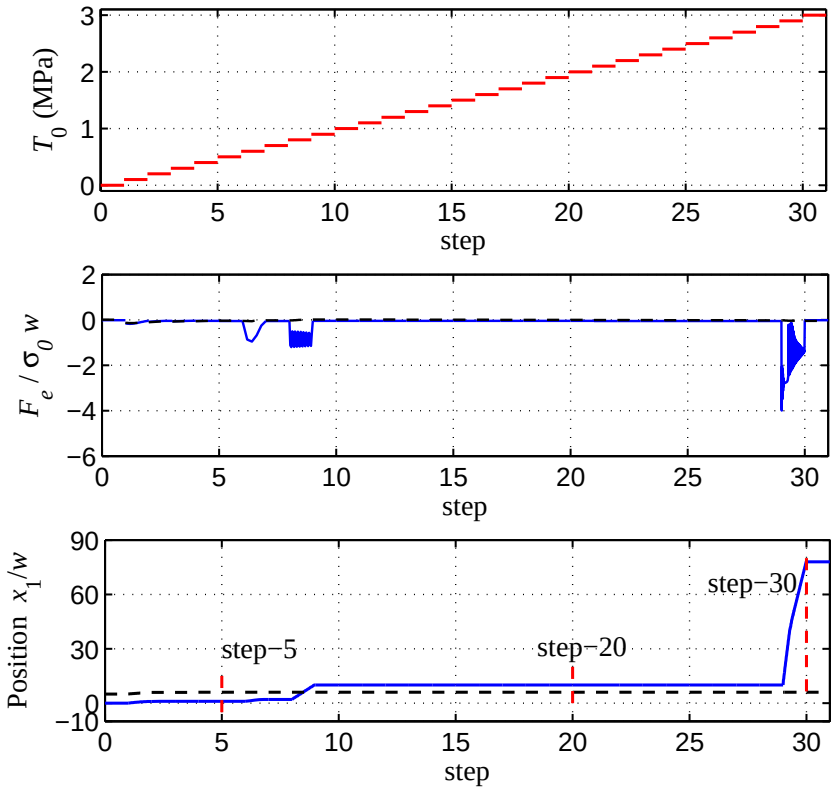
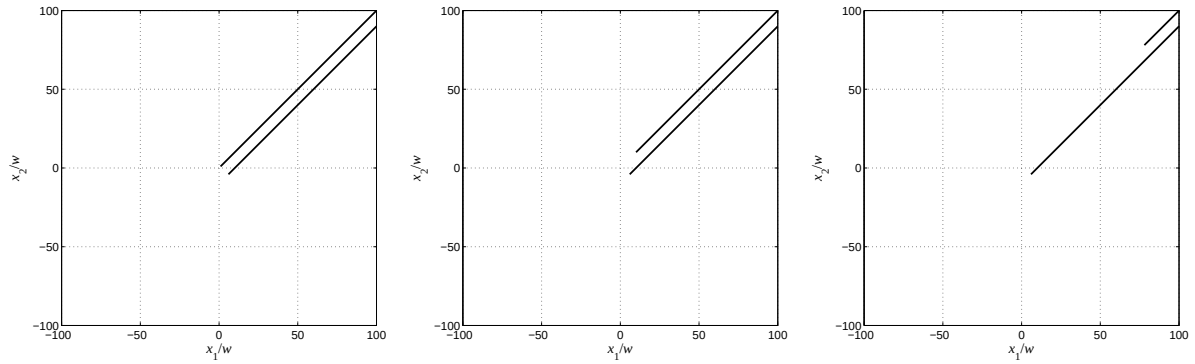


Figure 5.17: A pair of needle domains under the effect of compressive loads 0.1 MPa (Blue line: needle N_1; black line: needle N_2).



(a) step-5 **(b)** step-20 **(c)** step-30

Figure 5.18: The arrangement of needle domains for the different loading steps with the increment 0.1 MPa.

correspondence between the external loads and the arrangement of needles in the equilibrium state. The viscosity term η in the viscous model could be used as a fitting parameter to calibrate the simulations against experimental data.

5.4 Evolution of comb needles under mechanical loads

In this section, we will discuss the evolution of a comb of needles under compressive step loads. An array of comb-like needle domains composing 11 needle domains is selected. Their tips are located on the line orientated at 45° to the negative x_1 axis. The spacing of needle domains is kept as $10w$ along the x_1 direction. The equivalent dislocation and line charge of each needle domain is $\mathbf{b} = (3\sqrt{2}\varepsilon_0 w/2)\,[1\ 1\ 0\ 0]$ and $\mathbf{Q} = 0.48q[0\ 0\ 0\ 1]$, $q = \sqrt{2}p_0 w$, respectively. The compressive stress perpendicular to the direction of the parent domain is again applied on a sample with dimensions $500w \times 500w$. This compressive stress is incremented in steps of 0.02 MPa up to 3 MPa. At each loading step, when each needle domain reaches an equilibrium state, the next step of compressive stress is applied. The critical resistance force $F_{cr} = 0.05\sigma w$ was used.

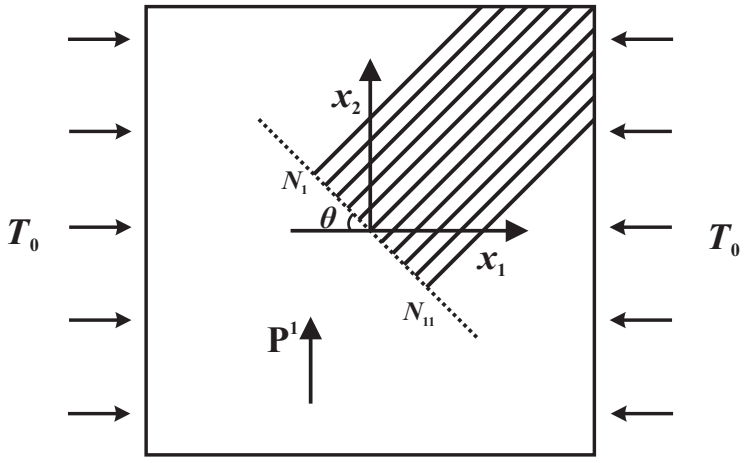
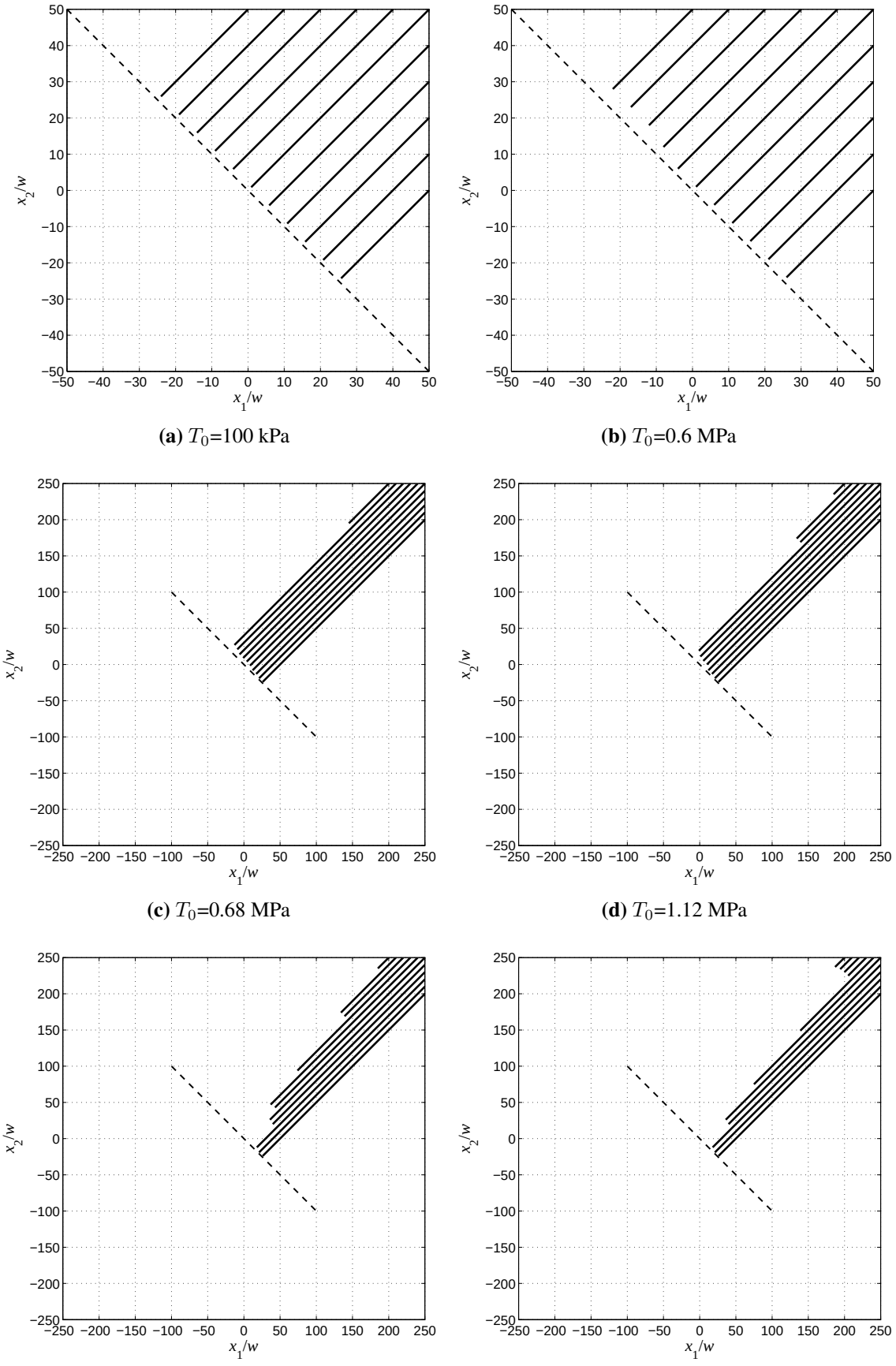


Figure 5.19: An array of comb-like needle domains under the action of the compressive stress.

Figure 5.20 present the evolution of comb-like needle domains under the action of the various stress loads. The dotted line is located at $x_2 = -x_1$ where the initial tip fronts of



(a) T_0=100 kPa

(b) T_0=0.6 MPa

(c) T_0=0.68 MPa

(d) T_0=1.12 MPa

(e) T_0=1.28 MPa

(f) T_0=2.6 MPa

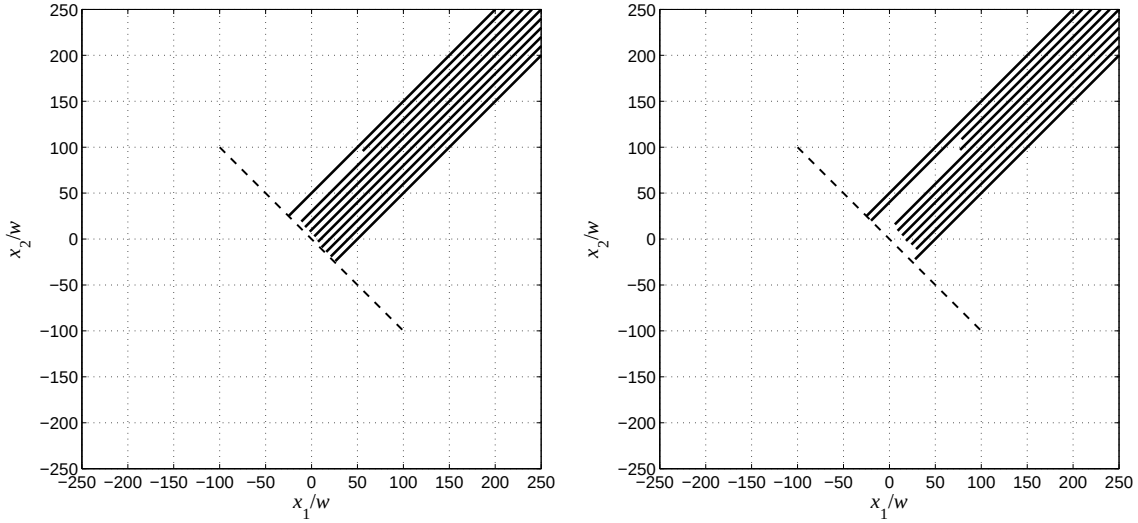
Figure 5.20: Evolution of comb-like needle domains applied by varying compressive loads.

the comb needles are. Each comb pattern in figure 5.20 is in the equilibrium state. Based on the change of the comb pattern in the figure 5.20, the comb needles are found to retreat in varying degrees under the application of the compressive loads. Figure 5.20a shows that when the external loads increase to 100 kPa, a slight retreat Δl ($< 1w$), which is the changing displacement along each needle longitude direction, happens to each of the needle domains. This is once again consistent with the observations of Potnis $et\ al.$ [52] who noted slight motion of a comb of needles under load. As the compressive step loads continually increase to 0.6 MPa, the moving displacement Δl for each needle domain is still slight in the range of about $1w$-$4w$. The angle θ between the tip front of the comb needles and the x_1 negative direction remains at 45°.

When the compressive load exceeds 0.68 MPa, the side needle domain N_1 shortens significantly toward the boundary of the sample. However, the rest of the needle domains remain in the 45° comb pattern. The long comb remains rather stable in the initial 45° comb pattern. Additionally, as the compressive load rises from 0.68 MPa to 0.98 MPa, the needle domains remain almost unchanged, as shown in figure 5.20c. As the compressive loads increase to 1.12 MPa, the needles N_2 and N_3 escape from the tip front line of comb needles and shorten toward the boundary, as shown in figure 5.20d. The needle domains successively break free from the comb as the external load is increased. Finally, a ladder pattern composed of needle domains forms, as presented in figures 5.20e and 5.20f. This ladder structure is reminiscent of the stepped patterns of domains observed in Chapter 3, though in that case the domain grew during thermal processing. In particular, groups of aligned needle tips are seen and these groups show different lengths of needle.

From the above results, we saw that the side needle N_1 was the first needle breaking free from the comb-tip fronts. After that, other needles also start to break away from the initial tip fronts when the external load is great enough. If the needle N_1 is pinned due to the existence of a defect in the crystals, what happens to this comb-like pattern of needles under the action of the

same compressive loads? To investigate this, the simulation was repeated, but with needle N_1 fixed. The comb-like needles then retreat only slightly when T_0 <0.76 MPa. With increasing load, needle N_2 breaks away from the tip fronts, as shown in figure 5.21a. We further test the case when both of the needles N_1 & N_2 are pinned. Then, only with T_0 >1.06 MPa, the needles N_3 and N_4 break away from the initial tip fronts. Comparing to the unpinned comb needle, the pinned comb needles are relatively more stable, needing greater loads to break from the configuration of the initial comb-like needles. However pinning a few needles does not prevent the comb from breaking up.



(a) Pin N_1, $T_0 = 0.76$ MPa **(b)** Pin N_1 & N_2, $T_0 = 1.06$ MPa

Figure 5.21: Evolution of comb-like needle domains with the pinned needle applied by varying compressive loads levels (a) The needle N_1 is pinned, (b) the needles N_1 and N_2 are pinned.

5.5 Conclusions

The superposition theory was adopted to analyse the effect of boundary condition in a finite material region. Through studying a single needle domain near a boundary, it was found to prefer either shortening towards an edge until disappearing or extending through the whole crystal.

Considering the effect of boundary condition and the lattice friction, the equilibrium arrangement of a pair of needle domains was different from the case of the infinite body without friction. However, through computing the energy, it was still found that the stable configuration of two interactive needle domains corresponded to polarization charge $0.48q$, which is the same as the infinite body case.

Evolution of pairs of needle domains and comb-like needle domains were simulated under the compressive loads. It was found the loading process influenced the evolution of the needle domains. Under the action of small incremental compressive loads, a slight and gradual motion of the comb happened, but the comb-like configuration was kept. When the compressive load was increased, bursts of needle domain motion occurred, along with the break-up of the comb into a ladder like pattern. The results are qualitatively similar to experimental observations which have not previously been explained using models.

6

Conclusions and further work

6.1 Conclusions and discussions

In this thesis needle domains in $BaTiO_3$ single crystals were modelled as edge dislocations with line charge. We studied the interaction and the common patterns of needle domains in $BaTiO_3$ single crystals for the case with no boundaries. The influence of boundaries was also investigated by modelling the effect of boundaries on the arrangement and evolution of needle domains.

In an experimental section, observation of needle domains in $BaTiO_3$ single crystals was made using optical microscopy and X-ray methods. First, temperature change was used to generate needle domains in a $BaTiO_3$ single crystal sample experiencing cooling through Curie temperature T_c. In practice, needle domains often appear during the cooling process of manufacturing single crystals. In the experiment, it was found that the pattern of needle domains changes with the variation of temperature.

It was also found that two common stable arrangements of needle domains exist, a comb-like needle pattern and a herringbone needle pattern. Later simulation results explained why these two arrangements are stable in barium titanate single crystals.

In experimental observations, the needle domain was a long slender domain with a sharp tip and narrow width. Additionally, the movement of needle domains under external loads (including heat, mechanical and electric loads) was along their own longitude direction, which could be analogous to the slip of the edge dislocations. Considering the mechanical and electric incompatibility, a single needle domain was modelled using discrete dislocations and line charges distributed over the tip. Considering the thin width of needle domains and the convenient study of interaction among needles, the concept of an effective edge dislocation with Burgers vector b and effective line charge q was proposed to model a single needle domain. The burgers vector b of this equivalent effective edge dislocation was a function of needle width w and a material constant, the spontaneous strain ε_0. The magnitude of the line charge was proportional to needle width w and spontaneous polarization p_0. According to the solution provided by Barnett and Lothe, the field and energy due to the needles was calculated to analyse the arrangement of needle domains. It was found that the total energy in a cylindrical region around the needle tip increases logarithmically with distance from the needle tip as may be expected from knowledge of classical dislocations. The energy due to formation of a needle domain was also proportional to the square of the width of the domain. During calculating, the full anisotropic and electrically coupled characteristics of $BaTiO_3$ single crystals were considered. Due to material anisotropy and electromechanical coupling, the interaction of needle domains differs significantly from classical results for interaction of dislocations in isotropic media.

The equilibrium distribution of collections of discrete needle domains in an infinite crystal was analysed with respect to variations in the needle domains position, including a pair of parallel needles with identical tips, a pair of parallel needles with opposite tips, and a pair of perpendicular needles. The equilibrium configurations of the needle domains were determined by finding a minimum potential energy configuration. For pairs of identical parallel needle domains, no stable equilibrium configuration was found. However, pairs of needles with opposite effective charge could form stable equilibrium configurations. The results suggested that the needle tip interactions tend to be dominated by electrostatic terms in $BaTiO_3$ single crystals. To

explore further, the stability of group of needles was also analysed. Herringbone-type arrays of needle domains were confirmed to be stable, though the needles towards the end of such a pattern are only weakly bound to the array. In the herringbone-type pattern, the presence of alternating effective charges reduces the overall energy resulting in a stable configuration. Since the electrostatic terms appear to dominate the interaction of nearby needles, the comb-like arrays of needle domains with identical tips are unstable within the model. However, the comb-like needle domains with identical tips, as a stable pattern, were often observed in practice. This paradoxical result lead us to pay more attention to the influence of screening by space charges on the stability of a needle pattern.

Through studying the interaction between two needle domains with identical tips, it was found that the existence and position of stable equilibrium states were sensitive to a change in the quantity of polarization charge. There was no stable equilibrium configuration until the effective polarization charge was reduced to 73.4% of the full theoretical value $q = \sqrt{2}p_0w$. As the polarization charge was decreased from $Q = 0.734q$ to 0, the position of stable equilibrium states for both needles and the energy in this equilibrium state also changed. Surprisingly, the energy due to two interactive needle domains without polarization charge was greater than twice the energy of an individual needle domain with full polarization charge. When the polarization charge was reduced to $Q = 0.48q$, the angle θ of the stable tip line of these two needles was $44.9°$. This is a remarkable result, and appears consistent with experimental observations of $45°$ combs of needle tips. The corresponding configuration had minimum energy with respect to Q, which suggests that this configuration was stable to changes in Q arising from the semiconducting nature of $BaTiO_3$. Additionally, the stability and the stable equilibrium position, when the polarization charge Q is equal to $0.48q$, still were consistent with the case of two interactive perpendicular needles with full polarization. Based on the model of an full effective dislocation and a reduced line charge $Q = 0.48q$, the analysis of comb-like needle pattern and herringbone needle pattern was consistent with experimental observation. The case of domain bundle boundaries in $BaTiO_3$ single crystals was also analysed to reconfirm the validity of the model.

The needle domain model was used to compute friction stress τ_0, based on the observation that needle tips form a shallow wedge shape, and using the theory of a dislocation pile-up group. The resistance force f acting on the needle domain is a function of the Burgers' vector b and friction stress τ_0. By considering the opening angle (about 1°) of a typical needle it was possible to estimate a friction stress τ_0 of about $2.3\sigma_0 \simeq 6$ MPa. This estimate is a little high compared to observed stress for needle growth in $BaTiO_3$ (approximately 1-4 MPa [52]), but of the same order.

Chapter 5 adopts the superposition theory to consider the effect of boundary conditions in a finite material region. Through studying a single needle domain near a boundary, it was found to prefer either shortening towards an edge until disappearing or extending through the whole crystal. Only if the needle domain is constrained by lattice friction or otherwise pinned by some defect can it terminate within the crystal. This is consistent with the observation that domains are often found in the form of complete laminations, rather than needles. A pair of needle domains was selected to further study the effect of a boundary on the equilibrium arrangement. Due to the effect of boundary conditions and the lattice friction, the equilibrium arrangement of this pair of needle domains was different from the case of the infinite body without friction. However, through computing the energy, it was still found that the stable configuration of two interactive needle domains corresponded to polarization charge $0.48q$ under the effect of boundary condition, which is the same as the infinite body case. Additionally, as the pair needles are approaching to an edge, the energy due to these interactive needle domains decreased for each fixed value of polarization charge.

Evolution of pairs of needle domains and comb-like needle domains were simulated under compressive loads. During the process of analysis, the lattice friction and viscous model were adopted, as well as the plane stress condition. It was found that the loading process influenced the evolution of the needle domains. Under the action of small incremental compressive loads, a slight and gradual motion of the comb happened, but the comb-like configuration was kept.

When the compressive load was increased, bursts of needle domain motion occurred, along with the break-up of the comb into a ladder like pattern. The results are qualitatively similar to experimental observations which have not previously been explained using models.

Overall, the thesis shows that there is potential to model needle domains and their evolution using a modified dislocation dynamics approach that accounts for anisotropy and eletromechanical coupling. The paradox that, with coupled anisotropic fields, needle domain combs become unstable, was identified for the first time (previous studies ignored this problem by using isotropic dislocation fields and neglecting charge). But the present study shows that allowing for some conduction of charge away from needle tips produces a minimum energy state that is consistent with combs of needles and other experimental observations.

6.2 Future work

6.2.1 Improvement of current model of needle domains

During discussion of the interaction and evolution of needle domains, the current model has shortcomings in two following aspects. To further improve the model, modelling of these conditions will be the subject of future work.

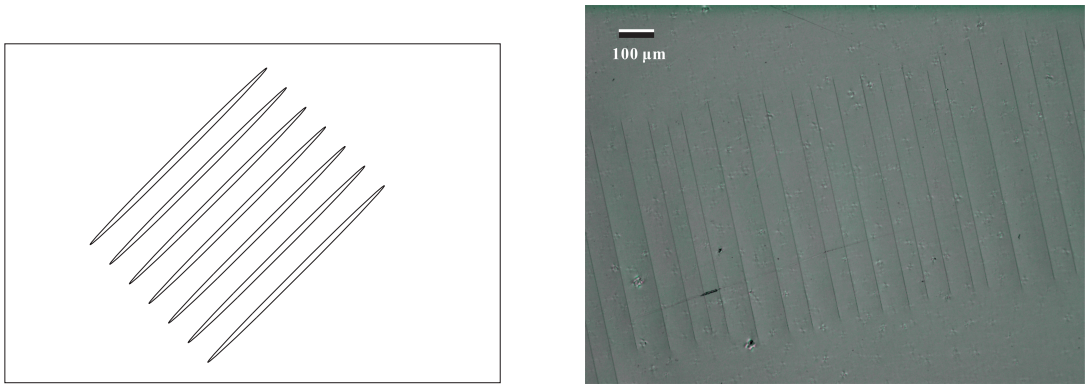
First, in the current model, we adopted an effective edge dislocation and an effective line charge to model a needle domain. Actually, this means that the model treats the tips of needle domains as blunt. However, the shape of the needle tip is not blunt and is typically round or wedge shaped. Therefore, we could improve the model, treating the tip as an assembly of dislocations and line charge distributed over the tip. The interaction of the equivalent dislocations and line charges in one needle domain will then influence the shape of the needle tip as well as its change in length. We could use experimental observation to map the shape of needle domains in various conditions, and so perfect the model. A better approximation to the near

field of one needle domain could also be obtained by superposition of a family of dislocations and line charges.

Second, due to the dislocation and line charge, a core singularity arises the calculation of energy produced by the needle domains. The energy outside the singular core region, which can be described by elastic continuum theory, is then main part of the line energy. In this thesis, we adopted the approximate method of cutting out a core region ($2w \times 2w$) in the process of calculating the energy. However, plastic deformation in crystals is heavily related to the dislocation core properties. But the elastic continuum theory can not be applied because of the strong distortion of the crystalline lattice existing around the field of the needle tip. Therefore, the atomistic, or first principles simulations need be utilized to analyse directly the interaction between atoms in the core region [81,98]. The energy of the core region is estimated to be about 10% of the total internal energy, so could be significant.

Besides the above aspects, there are several domain patterns worth further study. One interesting 90° a-a needle domain, which has two ends and a long slender shaft, commonly appears in the $BaTiO_3$ single crystal. Figure 6.1a and 6.1b gives the schematic configuration of a needle domain array with two ends and the observation obtained in an experiment. According to the model, the needle domain with two ends can be equivalent to two edge dislocations with opposite direction and two line charges with opposite sign. The arrangement and evolution of the needle domains with two ends will be studied in future work. Tension or compression of the whole sample under external loads could cause the formation of laminar texture from these needles.

In addition, for a large number of intensive needle domains (that is, when the needle domains are no longer dilutely dispersed in the parent domain), we need consider that the difference in polarization direction between the needle domains and parent domains leads to a difference in their material constants. In the current model, only the fields of the equivalent dislocation and line charge were used to model the effect of the needle tip. In future work,



(a) (b)

Figure 6.1: Needle domains with two ends: (a) Schematic graph of needle domains with two ends, (b) needle domains with two ends observed in the experiment.

the different polarization direction and material constants could be considered because these differences will influence the propagation of needle domains through the domain switching mechanism, if the needles are not dilute.

In this thesis, we have studied interaction and evolution of needle domains. It would be interesting to develop our model to analyse the needle nucleation. In Chapter 2, we have modelled a needle domain as an equivalent dislocation and line charge. However, there is no real dislocation and line charge existing at the needle tip. Therefore, we can not use any theory about dislocation nucleation criterion. Li and Landis [99, 100] has adopted phase-field model to study the nucleation of needle domain needles under small-scale-switching conditions and combined the factors of mechanical stress intensity and electric displacement intensity. Condition for needle domain nucleation is based on energetic considerations which postulate that 90° switching occurs when the work due to the applied stresses and electric fields on a switching process attain a critical level.

6.2.2 Free charge and free traction

In the current model, according to the condition of electrical compatibility, there is a jump in polarization and hence an effective charge wherever a needle domain meets a free surface. So

far, only zero voltage boundaries were considered. Then, free charge can accumulate at the surface as needed to balance the polarization jump. It is of interest to consider an equivalent line charge to model the field due to the needle end at a charge free surface. In the same way, the superposition theory is used to analyse this boundary value problem.

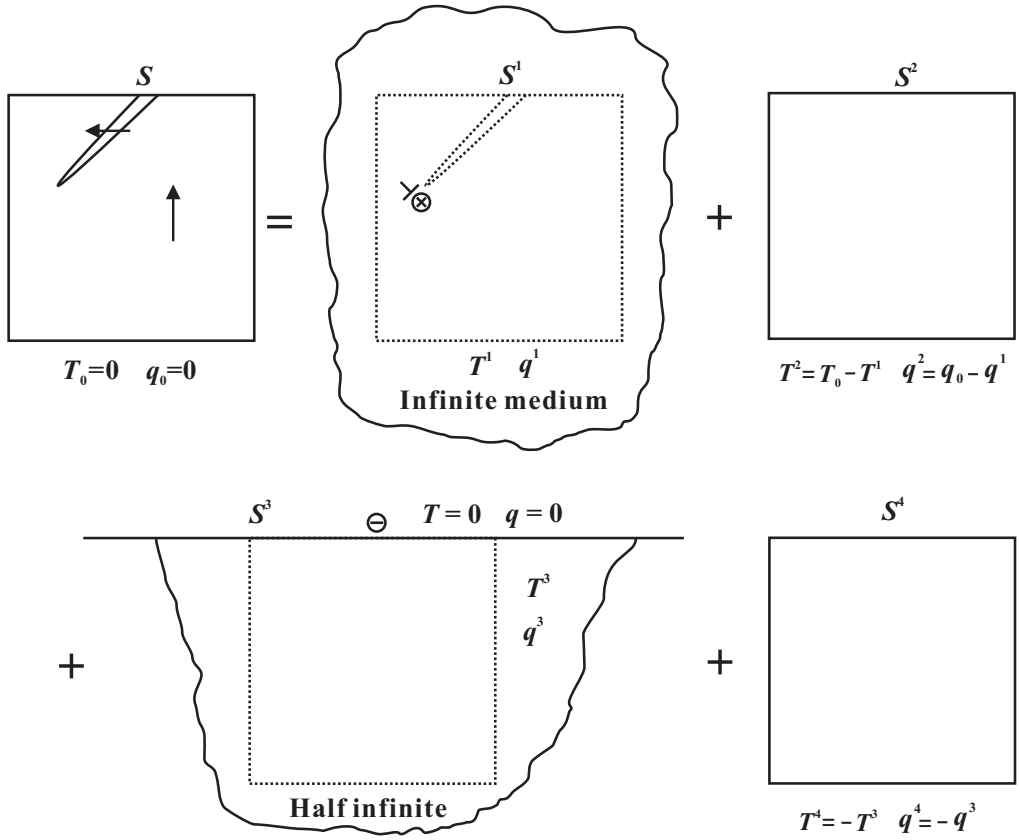


Figure 6.2: Decomposition of the boundary value problem

To avoid the near surface singularity resulting from the introduction of the equivalent line charge existing where the needle meets the surface, the original problem can be decomposed into four parts, as illustrated in figure 6.2.

- The S^1 fields are the superposition fields associated with the individual needle tips in an infinite medium, which can be calculated by the Barnett and Lothe's solution. The

boundary values at the boundary S^1:

$$T^1 = \sigma_{ij}^1 n_j \tag{6.1}$$

$$q^1 = D_i^1 n_i \tag{6.2}$$

- The image S^2 field, as a complementary field, is used to correct for the actual boundary conditions. The corresponding boundary loads:

$$T^2 = T_0 - \sigma_{ij}^1 n_j \tag{6.3}$$

$$q^2 = q_0 - D_i^1 n_i \tag{6.4}$$

- The S^3 fields are the superposition fields related to the near-surface needle end charges in a half-infinite problem. Free traction and free charge on edge where the needle end locates:

$$T = 0 \qquad q = 0 \tag{6.5}$$

The corresponding boundary loads for other edges:

$$T^3 = \sigma_{ij}^3 n_j \tag{6.6}$$

$$q^3 = D_i^3 n_i \tag{6.7}$$

- The S^4 fields are the complementary fields for the half-infinite S^3 fields. We can combine the boundary conditions of the S^2 and S^4 fields and adopt the finite element method to compute the superposition fields. The boundary loads can be calculated as follows:

$$T^4 = -\sigma_{ij}^3 n_j \tag{6.8}$$

$$q^4 = -D_i^3 n_i \tag{6.9}$$

where, T^i, D^i and q^i (i =1, 2, 3, 4) indicate the traction, electric displacement and charge on edges for the corresponding decomposed problem, respectively.

Green's functions of a half-infinite piezoelectric body can be adopted to compute the S^3 field. A generalized displacement vector **u** and a generalized stress $\boldsymbol{\phi}$ are:

$$\mathbf{u} = [u_1, u_2, u_3, \varphi]^T \qquad \boldsymbol{\phi} = [\phi_1, \phi_2, \phi_3, \phi_4]^T \tag{6.10}$$

where the superscript T represents a transpose, u_j are the displacement, φ is the electric potential, and ϕ_j are the generalized stress functions. The general solution for **u** and $\boldsymbol{\phi}$ can be expressed as [101–103]

$$\mathbf{u} = 2\mathbf{Re}\left[\mathbf{A}\mathbf{f}(z_*)\right] \tag{6.11}$$

$$\phi = 2\mathbf{Re}\left[\mathbf{B}\mathbf{f}(z_*)\right] \tag{6.12}$$

where, $\mathbf{f}(z_*) = [\mathrm{f}_1(z_1), \mathrm{f}_2(z_2), \mathrm{f}_3(z_3), \mathrm{f}_4(z_4)]^T$ is an arbitrary function vector of the generalized complex variables $z_\alpha = x_1 + \mu_\alpha x_2$ (α =1, 2, 3, 4), the choice of which depends on the boundary conditions provided by the given problems. **Re** and **Im** stand for the real and imaginary parts, respectively. The complex constants μ_α and the two 4×4 complex matrices **A** and **B** are functions of the materials constants. Additionally, the matrices **A** and **B** satisfy the following orthogonality relations [104, 105]

$$\begin{bmatrix} \mathbf{B}^T & \mathbf{A}^T \\ \bar{\mathbf{B}}^T & \bar{\mathbf{A}}^T \end{bmatrix} \begin{bmatrix} \mathbf{A} & \bar{\mathbf{A}} \\ \mathbf{B} & \bar{\mathbf{B}} \end{bmatrix} = \begin{bmatrix} \mathbf{I} & 0 \\ 0 & \mathbf{I} \end{bmatrix} \tag{6.13}$$

where **I** is a 4×4 unit matrix, and the closure relations:

$$\mathbf{A}\mathbf{B}^T + \overline{\mathbf{A}\mathbf{B}}^T = \mathbf{I} = \mathbf{B}\mathbf{A}^T + \overline{\mathbf{B}\mathbf{A}}^T \tag{6.14}$$

$$\mathbf{A}\mathbf{A}^T + \overline{\mathbf{A}\mathbf{A}}^T = 0 = \mathbf{B}\mathbf{B}^T + \overline{\mathbf{B}\mathbf{B}}^T \tag{6.15}$$

The solution of surface Green's functions for a surface line load derived by Gao *et al* [102] can be adopted. When a line load located at x_0 is applied to the surface of the piezoelectric material, we have,

$$\mathbf{u} = \frac{1}{\pi}\mathbf{Im}\sum_{\beta=1}^{4}\left[\mathbf{A}\left\langle\langle\mathbf{ln}(z_* - x_0)\rangle\right\rangle\mathbf{B}^{-1}\right]\mathbf{p} \tag{6.16}$$

$$\boldsymbol{\phi} = \frac{1}{\pi}\mathbf{Im}\sum_{\beta=1}^{4}\left[\mathbf{B}\left\langle\langle\mathbf{ln}(z_* - x_0)\rangle\right\rangle\mathbf{B}^{-1}\right]\mathbf{p} \tag{6.17}$$

where, $\mathbf{p} = [p_1, p_2, p_3, -q]^T$ indicates a generalized line load exerted at the surface x_0, where the p_j (j =1, 2, 3) and q are the components of the applied line force and the applied line charge, respectively. The angular brackets $\langle\langle\ \rangle\rangle$ indicate a diagonal matrix as:

$$\left\langle\langle\mathbf{ln}(z_* - x_0)\rangle\right\rangle = \text{diag}\left[\mathbf{ln}(z_1 - x_0), \mathbf{ln}(z_2 - x_0), \mathbf{ln}(z_3 - x_0), \mathbf{ln}(z_4 - x_0)\right] \tag{6.18}$$

The corresponding stress and electric displacement fields related to $\boldsymbol{\phi}$ are calculated as follows:

$$\left[\sigma_{11}, \sigma_{12}, \sigma_{13}, D_1\right]^T = -\frac{\partial\boldsymbol{\phi}}{\partial x_2} \tag{6.19}$$

$$\left[\sigma_{21}, \sigma_{22}, \sigma_{23}, D_2\right]^T = -\frac{\partial\boldsymbol{\phi}}{\partial x_1} \tag{6.20}$$

An initial attempt was made using this methodology to analyse needles in a finite body with charge-free surfaces. While the method looks promising, the calculations proved to be rather involved, and so are reserved as a future work topic.

Finally, it should be noted that while the methods developed in the thesis were applied to $BaTiO_3$ only, they are also applicable to a variety of materials. Of interest, some other ferroelectrics such as lead zirconate titanate (PZT) show broad, wedge shaped needles, sometimes

with curved profiles. These could be modelled using suitable distributions of charge and dislocations. Also, with some modifications, the methods could be used for studying needle twins in shape memory alloys and magnetic shape memory alloys.

A

List of publications and conference proceedings

Journal papers

- Sui D., Huber J. E. and Landis C. M., 2015, "Modelling and interaction of needle domains in Barium titanate single crystals," Journal of the Mechanics and Physics of Solids. (To be submitted)
- Sui D. and Huber J. E., 2015, "Evolution of needle domains in barium titanate single crystal under external excitation," Journal of Applied Physics. (To be submitted)

Conference Proceedings

- Sui D. and Huber J. E., 2012, "Modelling of needle domains in Barium titanate single crystals using dislocation theory," Proceeding of the ASME 2012 Conference on Smart Materials, Adaptive Structures and Intelligent Systems, SMASIS2012-8033.

References

[1] L. E. Cross and R. E. Newnham. History of ferroelectrics. *Ceramics and Civilization, High-Technology Ceramics-Past, Present, and Future, American Ceramic Society*, 111:289–305, 1987.

[2] J. F. Scott. Applications of modern ferroelectrics. *Science*, 315:954–959, 2007.

[3] R. E. Cohen. Origin of ferroelectricity in perovskite oxides. *Nature*, 358:136–138, 1992.

[4] G. H. Haertling. Ferroelectric ceramics: History and technology. *Journal of the American Ceramic Society*, 82:797–818, 1999.

[5] C. H. Sherman and J. L. Butler. *Transducers and Arrays for Underwater Sound*. Springer, 2007.

[6] J. J. Bernstein, S. L. Finberg, K. Houston, L. C. Niles, L. E. Cross, K. K. Li, and K. Udayakumar. Micromachined high frequency ferroelectric sonar transducers. *IEEE Transactions On Ultrasonics, Ferroelectrics, and Frequency Control*, 44:960–969, 1997.

[7] J. F. Scott and C. A. Paz de Araujo. Ferroelectric memories. *Science*, 246:1400–1405, 1989.

[8] J. F. Scott. *Ferroelectric Memories*. Springer, 2000.

[9] S. V. Kalinin, A. N. Morozovska, L. Q. Chen, and B. J. Rodriguez. Local polarization dynamics in ferroelectric materials. *Reports on Progress in Physics*, 73:1–67, 2010.

[10] F. Jona and G. Shirane. *Ferroelectric Crystals*. Pergamon Press. New York, 1962.

[11] W. J. Merz. The electric and optical behavior of $BaTiO_3$ single domain crystals. *Physical Review*, 76:1221–1225, 1949.

[12] P. W. Forsbergh. Domain structures and phase transitions in barium titanate. *Physical Review*, 76:1187–1201, 1949.

[13] J. H. Yen, Y. C Shu, J. Shieh, and J. H. Yeh. A study of electromechanical switching in ferroelectric single crystals. *Journal of the Mechanics and Physics of Solids*, 56:2117–2135, 2008.

[14] E. Burcsu, G. Ravichandran, and K. Bhattacharya. Large electrostrictive actuation of barium titanate single crystals. *Journal of the Mechanics and Physics of Solids*, 52:823–846, 2004.

[15] Z. Lu and M. Xiao. Observation of localized domain reversal of iron-doped potassium niobate single crystal. *Journal of Applied Physics*, 76:4451–4453, 1994.

[16] D. N. Fang, Y. J. Jiang, and C. T. Sun. Interactions between domain switching and crack propagatiion in poled $BaTiO_3$ single crystal under mechanical loading. *Acta Materialia*, 55:5758–5767, 2007.

[17] A. B. K. Njiwa, D. C. Lupascu, and J. Rodel. Crack tip switching zone in ferroelectric materials. *Acta Materialia*, 52:4919–4927, 2004.

[18] W. Yang and T. Zhu. Switching-toughening of ferroelectrics subjected to electric fields. *Journal of the Mechanics and Physics of Solids*, 46:291–311, 1998.

[19] C. S. lynch. The effect of uniaxial stress on the electromechanical response of 8/65/35 PLZT. *Acta Materialia*, 44:4137–4148, 1996.

[20] H. C. Cao and A. G. Evans. Nonlinear deformation of ferroelectric ceramics. *Journal of the American Ceramic Society*, 76:890–896, 1993.

[21] G. Arlt. Switching and dielectric nonlinearity of ferroelectric ceramics. *Ferroelectrics*, 189:91–101, 1996.

[22] S. E. Park and T. R. Shrout. Ultrahigh strain and piezoelectric behaviour in relaxor based ferroelectric single crystals. *Journal of Applied Physics*, 82:1804–1811, 1997.

[23] S. E. Park and T. R. Shrout. Characteristics of relaxor-based piezoelectric single crystals for ultrasonic transducers. *IEEE Transactions on Ultrasonics, Ferroelectrics and Frequency Control*, 44:1140–1147, 1997.

[24] T. Ritter, X. Geng, Lopath P. D. Kirk, S. K., S. E. Park, and T. R. Shrout. Single crystal PZN/PT-polymer composites for ultrasound transducer applications. *IEEE Transactions on Ultrasonics, Ferroelectrics and Frequency Control*, 47:792–800, 2000.

[25] T. R. Guruaja, R. K. Panda, J. Chen, and H. Beck. Single crystal transducers for medical imaging applications. *IEEE Ultrasonics Symposium Proceedings*, 2:969–972, 1999.

[26] S. Saitoh, T. Kobayashi, K. Harada, S. Shimanuki, and Y. Yamashita. A 20 MHz single-element ultrasonic probe using 0.91Pb(Zn$(1/3)$Nb$(2/3)$)O(3)-0.09PbTiO(3) single crystal. *IEEE Transactions on Ultrasonics, Ferroelectrics and Frequency Control*, 45:1071–1076, 1998.

[27] P. Wlodkowski. The development of high-sensitivity, low-noise accelerometers utilizing single crystal piezoelectric materials. *Sensors and Actuators A: Physical*, 90:125–131, 2001.

[28] Z.-G. Ye. *Handbook of advance dielectric, piezoelectric and ferroelectric materials*. Woolhead publishing limited, Cambridge, 2008.

[29] E. Aksel and J.L. Jones. Advances in lead-free piezoelectric materials for sensors and actuators. *Sensors*, 10:253–262, 2010.

[30] L. E. Cross. Lead free at last. *Nature*, 432:24–25, 2004.

[31] M. D. Maeder, D. Damjanovic, and N. Setter. Lead free piezoelectric materials. *Journal of Electroceramics*, 13:385–392, 2004.

[32] H. Fan, L. Zhao, B. Tang, C. Tian, and H. Kim. Growth and characterization of pmnt relaxor-based ferroelectric single crystal by flux method. *Materials Science and Engineering B*, 99:183–186, 2003.

[33] B. Fang, H. Xu, T. He, and H. Luo. Growth mechanism and electrical properties of PbO_3 single crystals by a modified Bridgman method. *Journal of Crystal Growth*, 244:318–326, 2002.

[34] W. Chen and Z. Ye. Top seeded solution growth and characterization of piezo-/ferroelectric $(1\text{-}x)$Pb$(Zn_{1/3}Nb_{2/3})O_3$-xPbTiO$_3$ single crystals. *Journal of Crystal Growth*, 233:503–511, 2001.

[35] K. Kitamura, J. Yamamoto, N. Iyi, S. Kirnura, and T. Hayashi. Stoichiometric $LiNbO_3$ single crystal growth by double crucible czochralski method using automatic powder supply system. *Journal of Crystal Growth*, 116:327–332, 1992.

[36] P. W. Rehrig, Trolier-McKinstry S., S. E. Park, and G. L. Messing. Dielectric and electromechanical properties of barium titanate single crystals grown by templated growth. *IEEE transactions on Ultrasonics, Ferroelectrics, and Frequency Control*, 47:895–902, 2000.

[37] A. Abdollahi and I. Arias. Phase-field modelling of the coupled microstructure and fracture evolution in ferroelectric single crystals. *Acta Materialia*, 59:4733–4746, 2011.

[38] Y. H. Zhang, J. Y. Li, and D. N. Fang. Fracture analysis of ferroelectric single crystals: Domain switching near crack tip and electric field induced crack propagation. *Journal of the Mechanics and Physics of Solids*, 61:114–130, 2013.

[39] K. Bhattacharya and G. Ravichandran. Ferroelectric perovskites for electromechanical actuation. *Acta Materialia*, 51:5941–5960, 2003.

[40] A. H. Sharon. *Understanding Solid State Physics*. Taylor & Francis, 2010.

[41] X. C. Tong. *Advanced materials for integrated optical waveguides*. Springer international publishing, 2014.

[42] Z Li, S. K. Chan, M. H. Grimsditch, and E. S. Zouboulis. The elastic and electromechanical properties of tetragonal $BaTiO_3$ single crystals. *Journal of Applied Physics*, 70:7327–7332, 1991.

[43] W. J. Merz. Domain formation and domain wall motion in ferroelectric $BaTiO_3$ single crystals. *Physical Review*, 95:690–698, 1954.

[44] E. A. Little. Dynamic behavior of domain walls in barium titanate. *Physical Review*, 98:978–984, 1955.

[45] G. Arlt and P. Sasko. Domain configuration and equilibrium size of domain in $BaTiO_3$ ceramics. *Journal of Applied Physics*, 51(9):4956, 1980.

[46] E. K. H. Salje and Y. Ishibashi. Mesoscopic structures in ferroelectric crystals: needle twins and right-angle domains. *Journal of Physics: Condensed Matter*, 8:8477–8495, 1996.

[47] J. F. Blackburn and E. K. H. Salje. Formation of needle shaped twin domains in cordierite: a computer simulation study. *Journal of Applied Physics*, 85:2414–2422, 1999.

[48] R. J. Harrison, S. A. T. Redfern, and E. K. H. Salje. Dynamical excitation and anelastic relaxation of ferroelastic domain walls in $LaAlO_3$. *Physical Review B*, 69:144101, 2004.

[49] A. K. Tagantsev, L. E. Cross, and J. Fousek. *Domains in ferroic crystals and thin films*. Springer-Verlag New York, Inc., 2010.

[50] Z. H. Zhang, X. Y. Qi, and X. F. Duan. Two-step evolution mechanism of multi-domains in $BaTiO_3$ single crystal investigated by in situ transmission electron microscopy. *Scripta Materialia*, 58:441–444, 2008.

[51] T. Matsumoto and M. Okamoto. Ferroelectric 180° a-a nanostripe and nanoneedle domains in thin $BaTiO_3$ films prepared with forcused-ion beam. *IEEE Transactions on Ultrasonics, Ferroelectrics, and Frequency Control*, 57:2127–2133, 2010.

[52] P. Potnis and J. Huber. In-situ observation of needle domain evolution in barium titanate single crystals. *Journal of the European Ceramic Society*, 33:327–333, 2013.

[53] J. Bornarel and J. Lajzerowicz. Experimental evidence for the long-range interaction of domains in ferroelectric KH_2PO_4. *Journal of Applied Physics*, 39:4339–4341, 1968.

[54] J. Bornarel. Existence of dislocations at domain tips in ferroelectric crystal KH_2PO_4. *Journal of Applied Physics*, 43:845–852, 1972.

[55] J. Bornarel and J. Lajzerowicz. Interdomain and domain defect interactions in kdp. *Ferroelectrics*, 4:177–187, 1972.

[56] R. J. Harrison, S. A. T. Redfern, A. Buckley, and E. K. H. Salje. Application of real-time, stroboscopic X-ray diffraction with dynamical mechanical analysis to characterize the motiion of ferroelectric domain walls. *Journal of Applied Physics*, 95:1706–1717, 2004.

[57] R. J. Harrison and E. K. H Salije. The noise of the needle: avalanches of a single progressing needle domain in $LaAlO_3$. *Applied Physics Letters*, 97:021907, 2010.

[58] J. Bornarel, J. lajzerowicz, and J. F. Legrand. Switching process in twinned ferroelectric crystals ferroelectrics. *Journal of Applied Physics*, 7:331–314, 1974.

[59] Z. H. Zhang, X. Y. Qi, and X. F. Duan. Direct determination of the polarization direction of domains in $BaTiO_3$ single crystal. *Applied Physics Letters*, 89:242905, 2006.

[60] X. Y. Qi, H. H. Liu, and X. F. Duan. In situ transmission electron microscopy study of electric-field-induced 90° domain switching in $BaTiO_3$ single crystals. *Applied Physics Letters*, 89:092908, 2006.

[61] W. Y. Li and C. M Landis. Nucleation and growth of domains near crack tips in single crystal ferroelectrics. *Engineering Fracture Mechanics*, 78:1505–1513, 2011.

[62] W. Y. Li and C. M Landis. Modeling of the nucleation and growth of domain needles. *ASME 2010 Conference on Smart Materials, Adaptive Structures and Intelligent Systems*, 1:373–374, 2010.

[63] D. Carka and C. M. Landis. Equilibrium conditions and evolution of needle domain arrays in ferroelectric single crystals. *ASME 2012 Conference on Smart Materials, Adaptive Structures and Intelligent Systems*, 2:255–257, 2012.

[64] E. Van der Giessen and A. Needleman. Discrete dislocation plasticity: a simple planar model. *Modelling and Simulation in Materials Science and Egineering*, 3:689–735, 1995.

[65] E. Orowan. Plasticity of crystals. IV. further foundation for the dynamic plasticity law. *Zeitschrift für Physik*, 89:605–634, 1934.

[66] M. F. Ashby and D. R. H. Jones. *Engineering materials 1*. Butterworth-Heinemann 2th Edition, 1996.

[67] D. Hull and D. J. Bacon. *Introduction to dislocations*. Butterworth-Heinemann, 2001.

[68] W. T. Read. *Dislocation in crystals*. McGraw-Hill, 1953.

[69] M. Peach and J. S. Koehler. The forces exerted on dislocations and the stress fields produced by them. *Physical Review*, 1:436–439, 1950.

[70] Y. N. Wang, S. J. Chen, and C. X. Tong. *Theory and application of dislocation*. Metallurgical Industry, 2007.

[71] J. P. Hirth and J. Lothe. *Theory of dislocations*. McGraw-Hill, New York, 1968.

[72] Y. C. Shu and K. Bhattacharya. Domain patterns and macroscopic behaviour of ferroelectric materials. *Philosophical Magazine B*, 81:2021–2054, 2001.

[73] J. Fousek and V. Janovec. The orientation of domain walls in twinned ferroelectric crystals. *Journal of Applied Physics*, 40:135–142, 1969.

[74] N. T. Tsou and J. E. Huber. Compatible domain structures and the poling of single crystal ferroelectrics. *Mechanics of Materials*, 42:740–753, 2010.

[75] A. R. Hutson and L. R. Walker. Piezoelectric potentials of dislocations in insulating crystals. *Journal of Applied Physics*, 50:6247–6250, 1979.

[76] G. Faivre and G. Saada. Dislocaitons in piezoelectric semiconductors. *Phys. Status Solidi (b)*, 52:127–140, 1972.

[77] L. Merten. Model of a screw dislocation in piezoelectric crystals. I general theory. *Phys. Kondens. Mater*, 2:53–70, 1964.

[78] J. D. Eshelby, W. T. Read, and W. Shockley. Anisotropic elasticity with application to dislocation theory. *Acta Metallurgica*, 1:251–259, 1953.

[79] A. N. Stroh. Dislocations and cracks in anisotropic elasticity. *Philosophical Magazine*, 3:625–646, 1958.

[80] D. M. Barnett and J. Lothe. Dislocations and line charges in anisotropic piezoelectric insulators. *Physica Status Solidi (b)*, 67:105–111, 1975.

[81] V. A. Lubarda, J. A. Blume, and A. Needleman. An analysis of equilibrium dislocation distribution. *Acta Metallurgica et Materialia*, 41:625–642, 1993.

[82] L. X. Zhang and X. Ren. Electro-shape-memory effect in Mn-doped $BaTiO_3$ single crystals and in situ observation of the reversible domain switching. *Materials Science and Engineering A*, 438-440:354–359, 2006.

[83] N. Niizeki and M. Hasegawa. Direct observation of antiparallel 180° domains in $BaTiO_3$ by X-ray anomalous dispersion method. *Journal of the Physcial Society of Japan*, 19:550–554, 1964.

[84] S. Kim, V. Gopalan, and B. Steiner. Direct X-ray synchrotron imaging of strains at 180° domain walls in congruent $LiNbO_3$ and $LiTaO_3$ crystals. *Applied Physics Letters*, 77:2051–2053, 2000.

[85] M. Birkhol. *Thin Film Analysis by X-ray Scattering*. WILEY-VCH, 2006.

[86] S. O. Hruszkewycz, M. J. Highland, M. V. Holt, D. J. Kim, C. M. Folkman, C. Thompson, A. Tripathi, G. B. Stephenson, S. Hong, and P. H. Fuoss. Imaging local polarization in ferroelectric thin films by coherent X-ray Bragg projection ptychogrphy. *Physical Review Letters*, 110:177601, 2013.

[87] B. M. Park and S. J. Chung. Synchrotron white-beam X-ray topography of ferroelectric domains in a $BaTiO_3$ single crystal. *Philosophical Magazine A*, 75:611–620, 1997.

[88] G. Fogarty, B. Steiner, M. Cronin-Golomb, U. Laor, M. H. Garrett, J. Martin, and R. Uhrin. Antiparallel ferroelectric domains in photorefractive barium titanate and strontium barium niobate observed by high-resolution X-ray diffraction imaging. *Journal of the Optical Society of America B-Optical Physics*, 13:2636–2648, 1996.

[89] K. Nittala, S. Mhin, J. L. Jones, D. S. Robinson, J. F. Ihlefeld, and G. L. Brennecka. In situ X-ray diffraction of solution-derived ferroelectric thin films for quantitative phase and texture evolution measurement. *Journal of Applied Physics*, 112:104109, 2012.

[90] M. E. Fitzpatrick, A. T. Fry, P. Holdway, F. A. Kandil, J. Shackleton, and L. Suominen. Determination of residual stresses by X-ray diffraction-issue 2. *Measurement Good Practice Guide*, 52:1–68, 2005.

[91] M. Ceretti, A. Piovano, A. Cousson, T. Berthier, M. Meven, G. Agostini, J. Schefer, O. Hernandex, C. Lamberti, and W. Paulus. Growth and characterization of large high quality brownmillerite $CaFeO_{2.5}$ single crystal. *Royal Society of Chemistry*, 14:5771–5776, 2012.

[92] P. R. Potnis. Single crystal ferroelectrics: Macroscopic and microscopic studies. *Thesis, University of Oxford*, 2011.

[93] J. Weertman. *Dislocation based fracture mechanics*. World Scientific, 1996.

[94] A. Widjaja and E. Van der Giessen. Contact area and size effects in discrete dislocation modelling of wedge indentation. *Journal of Material Research*, 22:655–663, 2007.

[95] L. J. McGilly, A. Schilling, and J. M. Gregg. Domain bundle boundaries in single crystal $BaTiO_3$ lamellae: searching for naturally forming dipole flux-closure/quadrupole chains. *Nano Letters*, 10:4200–4205, 2010.

[96] V. S. Deshpande, A. Needleman, and E. Van der Giessen. Dislocation dynamics is chaotic. *Scripta Materialia*, 45:1047–1053, 2001.

[97] J. F. Kung, H. Y. Bao, and J. M. Galligan. Yielding, mobile dislocations and chaos. *Scripta Materialia*, 34:479–482, 1996.

[98] E. Clouet, L. Ventelon, and F. Willaime. Dislocation core energies and core fields from first principles. *Physical Review Letters*, 102:055502, 2009.

[99] W. Y. Li and C. M. Landis. Nucleation and growth of domains near crack tips in single crystal ferroelectric. *Engineering Fracture Mechanics*, 78:1505–1513, 2011.

[100] W. Y. Li and C. M. Landis. Modelling of the nucleation and growth of domain needles. *Preceedings of the ASME 2010 conference on smart materials, adaptive structures and intelligent systems*, SMASIS2010-3917:1–2, 2010.

[101] J. Y. Liou and J. C. Sung. On the generalized Barnett-Lothe tensors for monoclinic piezoelctric materials. *International Journal of Solids and Structures*, 44:5208–5221, 2007.

[102] C. F. Gao and N. Noda. Green's functions of a half-infinite peizoelectric boday: Exact solutions. *Acta Mechanica*, 172:169–179, 2004.

[103] T. C. T. Ting. *Anisotropic Elasticity: Theory and Applications*. Oxford University Press, 1996.

[104] Z. C. Qu and Y. H. Chen. Explicit expressions of eigenvalues and eigenvectors for transversely isotropic piezoelectric materials. *Acta Mechanica*, 162:213–219, 2003.

[105] J. X. Liu, B. Wang, and S. Y. Du. Electro-elastic Green's functions for a piezoelectric hafl-space and their application. *Applied Mathematics and Mechanics*, 18:1037–1043, 1997.